

Dark Matter Phase Transitions in CP in the Dark

Master's Thesis
of

Lisa Biermann

at the Department of Physics
Institute for Theoretical Physics (ITP)

Reviewer: Prof. Dr. Milada Margarete Mühlleitner
Second Reviewer: PD Dr. Stefan Gieseke
Advisor: Dr. Jonas Müller

August 19, 2020 – July 20, 2021

I declare that I have developed and written the enclosed thesis completely by myself, and have not used sources or means without declaration in the text.

Karlsruhe, July 20, 2021, _____
Lisa Biermann

Accepted as Master thesis.

Karlsruhe, July 20, 2021, _____
Prof. Dr. Milada Margarete Mühlleitner

Contents

1. Introduction	1
2. Theoretical Background	3
2.1. Standard Model of Particle Physics	3
2.2. The Baryon Asymmetry of the Universe	5
2.2.1. Sakharov Conditions	7
2.2.2. Can the SM alone explain the BAU?	7
2.3. Electroweak Phase Transition	8
2.4. The Effective Potential Approach	10
2.5. Finite Temperature Field Theory	12
2.6. One-Loop Effective Potential at Finite Temperature	15
2.7. Resummation	16
3. CP in the Dark	19
4. Renormalization	23
4.1. Notation	23
4.2. $\overline{\text{MS}}$ Renormalization of the Effective Potential	24
4.3. Treatment of Finite Pieces	26
4.3.1. Conventional Mass Scheme	26
4.3.2. Modified Mass Scheme for CP in the Dark	29
4.3.3. Constraining the t Parameters	30
4.3.4. Changing the t Parameters	33
5. Results	45
5.1. Workflow	45
5.1.1. ScannerS	45
5.1.2. BSMPT	46
5.2. Parameter Point Sample	49
5.3. VEV Configuration Analysis	49
5.4. SFOEWPT in CP in the Dark	55
5.5. Doublet and Singlet Admixture	60
5.6. Trilinear Higgs Self-Couplings	62
5.7. DM observables	65
5.8. Branching Ratios of the SM-like Higgs Boson	68
6. Conclusions	73
Acknowledgements	75
Appendix	77
A. Fourth derivative of the Coleman-Weinberg potential	77
B. Benchmark points	78

1. Introduction

Almost nine years past the discovery of a Standard Model-like Higgs boson at the LHC [1, 2], particle physics faces an era of precision measurements. Although predictions from the Standard Model (SM) of particle physics are consistent with experimental results, the tension towards statistical significant discrepancies has been intensified with recent findings of the Muon $g - 2$ experiment [3]. Furthermore, there is clear evidence for physics beyond the SM, for example from cosmology. The matter that is described by the SM is only able to account for around 15.6% of the total matter density of the universe, the rest is the so-far unknown dark matter (DM) [4]. There is clear evidence for its gravitational interactions [4–6] and the presence of non-relativistic DM is also essential in order to successfully describe the formation of structures in the early universe [7].

In addition to DM, another open question is the non-zero baryon asymmetry of the universe (BAU). Although the Big Bang theory predicts an initial baryon-antibaryon symmetric state, the Planck Collaboration determines today's BAU at [4]

$$\eta \equiv \frac{n_b - \bar{n}_b}{n_\gamma} \simeq \frac{n_b}{n_\gamma} \simeq 6.1 \times 10^{-10}. \quad (1.1)$$

Sakharov proposed three conditions that enable a dynamical generation of a non-zero BAU starting from an initially baryon-antibaryon symmetric state [8]. They are: C and CP -violation, baryon number violation and departure from thermal equilibrium. Electroweak baryogenesis (EWBG) is a possible framework that can explain the dynamical generation of the BAU during the era of the electroweak phase transition (EWPT) in the early universe in combination with beyond the SM (BSM) physics. BSM models are required for an EWBG scenario to enable a *strong first-order electroweak phase transition* (SFOEWPT) that provides the departure from thermal equilibrium that is necessary to fulfill the third Sakharov condition. For the measured SM-like Higgs mass $m_h = (125.10 \pm 0.14)$ GeV [9] the EWPT can only be realized through a smooth cross-over phase transition in the SM [10, 11]. An SFOEWPT is characterized by ξ_c , the ratio between the vacuum expectation value v_c at the temperature of the EWPT and the *critical temperature* T_c [12, 13], that exceeds one, i.e.

$$\xi_c \equiv \frac{v_c}{T_c} \gtrsim 1. \quad (1.2)$$

Additionally, a BSM model has to include non-standard CP -violation, as the amount of CP -violation in the SM is not sufficient to enable EWBG.

This Master thesis studies the model CP in the Dark, that was introduced in [14]. The model features an extension of the SM scalar sector by an additional dark $SU(2)$ -doublet and an additional dark real singlet. CP in the Dark is a specific Next-to-Minimal Two-

Higgs-Doublet Model (N2HDM) [15–17], with only one additional \mathbb{Z}_2 -symmetry. This imposed symmetry stabilizes the dark sector at $T = 0$ GeV, providing a stable neutral particle dark matter candidate h_1 and in addition an SM-like first doublet that features the SM-like Higgs boson h . The model also introduces two heavier neutral dark scalars h_2 and h_3 , as well as the charged dark scalars H^\pm . CP in the Dark provides additional CP -violation in the dark sector that makes it a particularly interesting model candidate in an EWBG scenario. In this Master thesis, we study the potential of the model CP in the Dark to provide parameter points compatible with the relevant theoretical and experimental constraints that show an SFOEWPT, which is a necessary condition in an EWBG scenario for the generation of the BAU.

The structure of this thesis is as follows. In Chapter 2 we build the theoretical foundation of this thesis. A short introduction to the SM is given in Sec. 2.1. The open question of the baryon asymmetry of the universe is introduced in Sec. 2.2. Sections 2.3-2.7 present the description of particle physics in the hot early universe at times around the electroweak phase transition. The model CP in the Dark is described in detail in Chapter 3. Chapter 4 gives its renormalization prescription, with special focus on the role of the unconstrained finite pieces of the chosen renormalization scheme. Our results are presented in Chapter 5. The work is summarized and concluded in Chapter 6.

2. Theoretical Background

The following sections give an overview on the theoretical background of this Master thesis. Section 2.1 introduces the Standard Model (SM) of particle physics focussing on the SM Higgs mechanism. An introduction to the open question of explaining the baryon asymmetry of the universe (BAU) is given in Sec. 2.2. Section 2.3 provides more details on the electroweak phase transition. The formalism used to describe the Higgs sector at finite temperature in the hot early universe is introduced in Secs. 2.4 to 2.7.

2.1. Standard Model of Particle Physics

The SM provides us with the most complete understanding of particle physics based on a renormalizable quantum field theory with the symmetry group [18]

$$SU(3)_C \times SU(2)_L \times U(1)_Y. \quad (2.1)$$

Postulating local gauge invariance of the SM Lagrangian under the symmetry transformation of Eq. (2.1) introduces the covariant derivative $\partial_\mu \rightarrow D_\mu$ and the gauge fields. The gauge bosons mediate fundamental interactions between particles. Particles are understood as excitations of quantum fields. They carry quantum numbers and have certain transformation properties under the symmetry groups of the gauge interactions.

Three of the four fundamental interactions are described within the SM. The strong interaction is mediated by gluons G_μ^a that are the gauge bosons of the $SU(3)_C$. The electroweak interaction is mediated by the gauge bosons of the $SU(2)_L \times U(1)_Y$ gauge groups, the $W_{1,2,3}^\mu$ and B^μ bosons.

It has been verified experimentally that the electroweak gauge bosons and all fermions are massive.¹ However, naive mass terms break the symmetry of the SM and can therefore not be introduced in the usual bilinear way.

Moreover, unitarity in a quantum field theory like the SM with massive gauge bosons and fermions that interact weakly up to high scales, can be restored by introducing an additional scalar boson which couples to SM particles proportional to their masses. The SM Higgs boson is such a scalar boson. It was first postulated in the Brout-Englert-Higgs (BEH) mechanism [20–23]. The mechanism explains fermion and gauge boson masses in a gauge-invariant way.

¹Neutrinos are massless in the SM, although they have to carry a non-zero mass. The process called neutrino oscillation is only possible for non-zero neutrino masses m_ν and can explain the solar neutrino flux and all other experimental findings related to neutrinos. The current world-best limit is set by the KATRIN experiment in Karlsruhe [19].

The BEH mechanism introduces a complex $SU(2)_L$ doublet field Φ together with the Higgs potential $V(\Phi)$

$$V(\Phi) = \mu^2 \Phi^\dagger \Phi + \lambda (\Phi^\dagger \Phi)^2, \quad (2.2)$$

with

$$\mu^2 < 0. \quad (2.3)$$

Expanding the SM-Higgs field Φ around its minimum yields

$$\Phi = \begin{pmatrix} \phi^+ \\ \phi^0 \end{pmatrix} \equiv \begin{pmatrix} G^\pm \\ \frac{1}{\sqrt{2}}(v + h + iG^0) \end{pmatrix}, \quad (2.4)$$

with the vacuum expectation value (VEV)

$$v = \sqrt{\frac{-\mu^2}{2\lambda}} \approx 246.22 \text{ GeV}. \quad (2.5)$$

The ground state of the Higgs field

$$\langle \Phi \rangle = \frac{1}{\sqrt{2}} \begin{pmatrix} 0 \\ v \end{pmatrix} \quad (2.6)$$

spontaneously breaks $SU(2)_L \times U(1)_Y$ down to $U(1)_{em}$. The photon γ as gauge boson of the unbroken $U(1)_{em}$ remains massless.

Each of the three broken degrees of freedom introduces a massless Pseudo Goldstone boson into the theory. Additionally, we get one massive scalar Higgs boson h . In *unitary gauge* the degrees of freedom which are associated with Goldstone bosons are absorbed into the mass eigenstates for the electroweak gauge bosons W^\pm and Z . The Higgs field in unitary gauge reads

$$\Phi = \begin{pmatrix} 0 \\ \frac{1}{\sqrt{2}}(v + h) \end{pmatrix}. \quad (2.7)$$

The Higgs mechanism describes the minimalistic extension necessary in order to explain massive gauge bosons and fermions. The fermions obtain their masses through the Yukawa couplings, introducing an interaction between the SM Higgs bosons and the fermions, respectively.

With the discovery of an SM-like Higgs boson with $m_h = (125.10 \pm 0.14) \text{ GeV}$ [9] at CERN by ATLAS [1] and CMS [2] in 2012 the last missing piece of the SM and also the first elementary scalar particle was found experimentally.

2.2. The Baryon Asymmetry of the Universe

The standard model of Big Bang cosmology is the *Lambda Cold Dark Matter* model Λ CDM. It is based on today's most important observations on our universe:

- *Expansion*: The universe is expanding. The expansion is described by a growing scale factor $a(t)$. The *Hubble parameter* [9]

$$H(t) = \frac{\dot{a}(t)}{a(t)} \quad (2.8)$$

describes the rate of the expansion. A measurable consequence is the redshift of photons emitted by cosmological sources [24]. Fig. 2.1 sketches the evolution of the universe with time and decreasing temperature.

- *Isotropy and homogeneity*: Largest structures in the universe are superclusters of galaxies that reach sizes of up to a couple of 10 Mpc. Matter and energy is evenly distributed considering scales larger than 10^2 Mpc [9, 25].
- *Cosmic Microwave Background*: Nearly ideal gas of photons with temperature

$$T = (2.7255 \pm 0.0006) \text{ K} \quad (2.9)$$

that fills the universe and shows angular fluctuations of $\delta T/T \sim 10^{-5}$ [9].

- *Dark Matter*: Ordinary baryonic matter with a relic density of [4]

$$\Omega_b h^2 = 0.02237 \pm 0.00015 \quad (2.10)$$

only accounts for around 15.6% of the matter density of the universe [4]

$$\Omega_m h^2 = 0.1430 \pm 0.0011. \quad (2.11)$$

Almost 84% of the matter relic density consists of *cold* dark matter [4]

$$\Omega_c h^2 = 0.1200 \pm 0.0012. \quad (2.12)$$

While the cosmological large-scale evidence clearly indicates the presence of additional matter in the universe [4, 5], so far dark matter has hidden from searches for baryonic matter. It therefore has to be sufficiently electrically neutral. Dark matter also plays an important role in the formation of structures in the early universe. It is required to be non-relativistic or *cold* to be able to stabilize the process of matter accumulation [7].

During the ongoing expansion that was accelerated during an era called inflation an equal amount of baryons and antibaryons is created originating from the initial symmetric state associated with the Big Bang. However, observations today show a BAU. Primordial antimatter has so far not been observed and all cosmological antimatter can be consistently explained by mechanisms of secondary production in cosmic rays. The BAU is quantified by the baryon asymmetry to photon density ratio η . The baryon asymmetry density $n_B - n_{\bar{B}}$ is nearly equal to the density of baryons $n_B - n_{\bar{B}} \simeq n_B$. The Planck Collaboration determines the BAU to be [4]

$$\eta \equiv \frac{n_b - \bar{n}_b}{n_\gamma} \simeq \frac{n_b}{n_\gamma} \simeq 6.1 \times 10^{-10}. \quad (2.13)$$

The evolution of a baryon-asymmetric universe from an initially baryon-symmetric state could in principle be explained by a mechanism that prevents the baryon-antibaryon

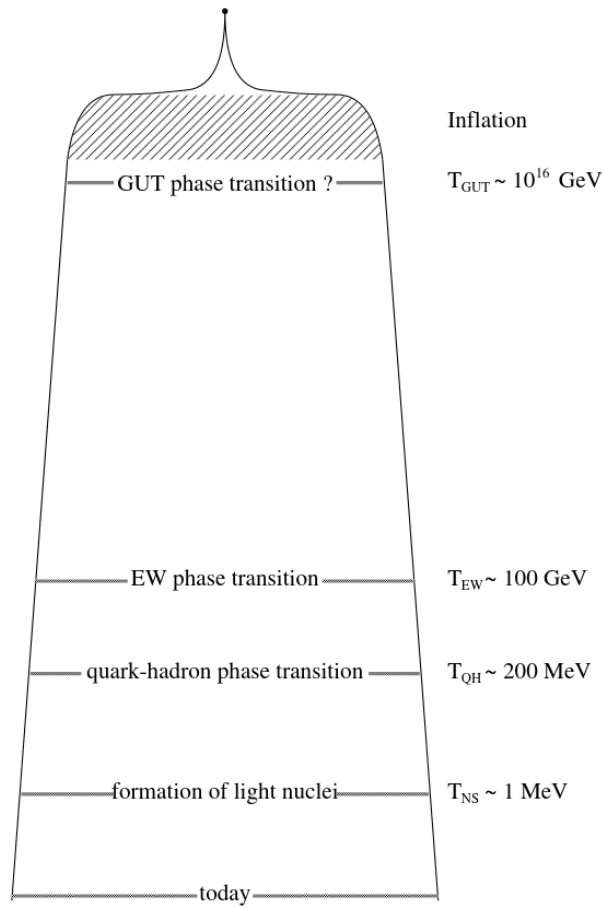


Figure 2.1.: Sketch of the temporal evolution of the universe. The Big Bang is followed by a period of accelerated expansion, called *inflation*. With continuing, but much slower expansion and decreasing temperature, the universe undergoes several phase transitions. The era of the electroweak phase transition around $T_{\text{EW}} = 100 \text{ GeV}$ is of special interest in the context of this thesis as it gives rise to scenarios of electroweak baryogenesis enabling the explanation of a dynamical generation of the observed baryon asymmetry of the universe, see Secs. 2.2 and 2.3. The figure is taken from [26].

annihilation. However, after inflation the causally connected region is too small for such a process to successfully appear. Assuming that the universe does not start from an initially baryon-antibaryon symmetric one, but from a state with an initial baryon excess can also not solve the problem. A small initial baryon excess is not able to survive inflation and would be washed out in this process [26].

The dynamical generation of the BAU originating from a symmetric vacuum is possible for a model that fulfills the conditions by Sakharov [8].

2.2.1. Sakharov Conditions

The observed excess of matter over antimatter has to evolve from an initial state with baryon asymmetry equal to zero. A dynamical creation of a BAU is possible given that the three Sakharov conditions are fulfilled [8]:

- Existence of baryon number B violating processes,
- C and CP violation and
- departure from thermal equilibrium.

The Sakharov conditions are necessary, but in general not sufficient in order to generate the BAU in an electroweak baryogenesis (EWBG) scenario.

2.2.2. Can the SM alone explain the BAU?

The SM already provides C , CP and B violation. C and CP violation occur in the charged weak currents. The Kobayashi-Maskawa (KM) mechanism [27] explains the observed CP violation in K meson systems and B meson decays via a non-zero complex and therefore a CP -violating phase in the Cabibbo–Kobayashi–Maskawa (CKM) matrix.

In present-day experiments the baryon B and lepton number L appear to be good quantum numbers. More specifically, the global $U(1)_B$ and $U(1)_L$ gauge symmetries of the Lagrangian suffer from the *Adler-Bell-Jackiw* chiral anomaly which results in conservation of $B - L$ because the difference of the associated symmetry currents vanish [26]

$$\partial^\mu (J_\mu^B - J_\mu^L) = 0. \quad (2.14)$$

Baryon and lepton number violation in the SM is a non-perturbative effect. B and L are conserved as long as the perturbative approach is still justified. However, non-abelian gauge theories have many equivalent topological minima whose ground states have different topological charge classified by a non-zero *Chern-Simons number* N_{CS} . Ground states with different N_{CS} are separated by a potential barrier and correspond to large gauge field variations beyond the size of perturbative fluctuations. They can violate B and L by units of flavor n_F [28],

$$\Delta B = \Delta L = n_F \Delta N_{CS}. \quad (2.15)$$

A classical calculation by 't Hooft [28, 29] showed that at zero temperature the needed tunneling process between two topologically different vacuum field configurations is highly suppressed

$$\sigma_{B+L} \sim 10^{-164}. \quad (2.16)$$

The situation changes at finite temperature. *Sphalerons*, classical mixtures of gauge and Higgs fields who topologically lie on the path with minimum energy, mediate transitions

between different minima [30, 31]. The electroweak symmetry is restored for temperatures roughly above the electroweak scale $T_{\text{EW}} = 100 \text{ GeV}$ [32]. Then B and L violating transitions are no longer suppressed. As long as [26]

$$T_{\text{EW}} < T \lesssim 10^{12} \text{ GeV} \quad (2.17)$$

we are in the symmetric Higgs phase and sphaleron-mediated $B + L$ violating processes are in thermal equilibrium because

$$\Gamma_{\cancel{B+L}}^{\text{sph}}(T > T_{\text{EW}}) \gg H, \quad (2.18)$$

with the Hubble parameter H defined in Eq. (2.8). Whether the departure from thermal equilibrium is sufficiently strong in order to fulfill the third Sakharov condition is discussed in Sec. 2.3.

2.3. Electroweak Phase Transition

It has been shown that spontaneously broken gauge symmetries are restored at high temperature [33–37]. At finite temperature, the Higgs potential passes from the symmetry-breaking VEV to a symmetric ground state. This electroweak phase transition (EWPT) takes place around [32]

$$T_{\text{EW}} = 100 \text{ GeV}. \quad (2.19)$$

In the early universe at $T > T_{\text{EW}}$ consequently all SM-like gauge bosons and fermions are massless.

A phase transition is characterized by an order parameter. For systems with a spontaneously broken electroweak symmetry, the electroweak VEV ω is a suitable order parameter. The *critical temperature* T_c is defined as the temperature, where the symmetric and broken minima of the potential V are degenerate,

$$V(\omega = 0, T_c) = V(\omega \neq 0, T_c). \quad (2.20)$$

First-order phase transitions are characterized by a discontinuity in the order parameter at T_c . For second-order phase transitions the vicinity of T_c is also characterized by a significant, but continuous change in the order parameter. The departure from thermal equilibrium needed for a dynamically generated BAU in context of the criteria by Sakharov (see Sec. 2.2) can only be guaranteed through a *sufficiently* strong first-order EWPT.²

EWBG is a suitable candidate for an explanation of the BAU production, however only possible with beyond the Standard Model (BSM) physics. It takes place in the period after inflation and before or around the electroweak phase transition at $T_{\text{EW}} = 100 \text{ GeV}$.

As long as $T > T_{\text{EW}}$ sphaleron-mediated B and L violating processes are in thermal equilibrium. All fermions and bosons are still massless as the $SU(2)_L \times U(1)_Y$ symmetry is a global unbroken symmetry of the theory. As the universe cools down, the temperature T eventually comes in the vicinity of T_{EW} triggering EWPTs. Bubbles with the symmetry-breaking vacuum state now start to nucleate. In order to conserve the BAU, the bubbles

²Since lattice gauge theory disfavors a first-order QCD phase transition with the known non-zero quark masses [38], first-order phase transitions during the EWPT are a favored scenario to determine the baryon density.

must get filled with more baryons than antibaryons and further B violating processes inside the bubbles must be prohibited. The sphaleron rate needs to be sufficiently suppressed in the broken phase inside the bubbles. In the broken phase it is given by [39]

$$\Gamma_{\beta+\mathcal{L}}^{\text{sph}} \propto \exp - \frac{E_{\text{sph}}(T)}{T}. \quad (2.21)$$

The sphaleron energy $E_{\text{sph}}(T)$ can be expressed in terms of $\phi_c(T_c)$, the classical field configuration that minimizes the effective potential (see Sec. 2.4) at T_c [39]. $\Gamma_{\beta+\mathcal{L}}^{\text{sph}}$ is sufficiently suppressed in order to explain the BAU if the *baryon wash-out* condition is fulfilled [12, 13]

$$\xi_c \equiv \frac{v_c}{T_c} \gtrsim 1. \quad (2.22)$$

If Eq. (2.22) is satisfied, the EWPT is a strong first-order electroweak phase transition (SFOEWPT).

The size of the discontinuity in the order parameter for the EWPT in the SM is dependent on the SM Higgs boson mass m_h , it gets smaller for larger m_h . An SFOEWPT is only possible for $m_h \lesssim 70 - 80 \text{ GeV}$ [10, 11]. For the measured $m_h = (125.10 \pm 0.14) \text{ GeV}$ [9] the EWPT can only take place through a *smooth cross-over* phase transition that does not provide the necessary departure from thermal equilibrium to explain the BAU [26].

Consequently, the initial question of Sec. 2.2.2 is answered with a *no*. The SM with its explanation of electroweak symmetry breaking through the BEH mechanism alone is not sufficient to explain the dynamical generation of today's observed BAU in the early universe. Note, that in addition to not sufficiently suppressing the sphaleron transitions, also the \mathcal{CP} -violation (CPV) is not large enough in the SM to explain baryogenesis [40]. It is therefore crucial to formulate BSM models that not only enable an SFOEWPT, but also include sources of additional non-standard CPV. The model CP in the Dark which is discussed in this thesis, can be such a suitable model candidate.

2.4. The Effective Potential Approach

It was shown in [41] that radiative corrections can significantly change the symmetry-breaking behavior of a theory. At tree level, the postulated SM Higgs potential of Eq. (2.2) is stable. But higher-order corrections play an important role. The requirement of vacuum stability up to the Planck mass scale imposes an upper bound on the top quark pole mass [42, 43]. Vacuum stability for BSM models with additional scalar degrees of freedom is studied for example in [44–47] for the Two-Higgs-Doublet Model (2HDM) and in [16, 17] for the Next-to-Minimal Two-Higgs-Doublet Model (N2HDM).

The effective potential approach (EPA) enables an all-order description of the complete vacuum state of a theory, considering tree-level interactions and also all possible quantum corrections. The minimum of the *effective potential* is the true vacuum state of the quantum field theory, including interactions of all orders of perturbation theory.

The probability amplitude for the general transition between two vacuum states $|0_{\text{in}}\rangle$ and $|0_{\text{out}}\rangle$ in the presence of external sources can be calculated knowing the *generating functional* for the *connected* Greens function $W(J)$ [41, 48]

$$\begin{aligned}
 W(J) = & \sum_{n_1, n_2, n_3, \dots, n_N} \frac{1}{n_1! n_2! n_3! \dots n_N!} \int d^4 x_1 d^4 x_2 \dots d^4 x_{n_1} d^4 y_1 \dots d^4 y_{n_2} \dots d^4 w_1 \dots d^4 w_{n_N} \\
 & \times G^{(n_1, n_2, n_3, \dots, n_N)}(x_1, x_2, \dots, x_{n_1}, y_1, \dots, y_{n_2}, \dots, w_1, \dots, w_{n_N}) \\
 & \times J_1(x_1) J_1(x_2) \dots J_1(x_{n_1}) J_2(y_1) \dots J_2(y_{n_2}) \dots J_i(w_1) \dots J_i(w_{n_N}),
 \end{aligned} \tag{2.23}$$

where J_i with $i \in \{1, \dots, N\}$ are sources introduced for each of the N fields Φ_i of the theory. $G^{(n_1, \dots, n_N)}(x_1, \dots, w_{n_N})$ are the *connected* Greens function that are constructed by the sum of all *connected* Feynman diagrams with n_i external lines of the particle i .³ The integration is performed in $\sum_{i=1}^N n_i$ directions that are labeled in Eq. (2.23) by x_i with $i \in \{1, \dots, n_1\}$, y_j with $j \in \{1, \dots, n_2\}$, \dots , and w_k with $k \in \{1, \dots, n_N\}$, respectively. Then the probability amplitude for the transition between two vacuum states reads

$$\langle 0_{\text{out}} | 0_{\text{in}} \rangle = e^{iW(J)}. \tag{2.24}$$

A classical field $\Phi_{c,i}$ can be understood as the variation of $W(J)$ with respect to the external source J_i

$$\Phi_{c,i} = \frac{\delta W(J)}{\delta J_i(x)} = \frac{\langle 0_{\text{out}} | \Phi_i(x) | 0_{\text{in}} \rangle_J}{\langle 0_{\text{out}} | 0_{\text{in}} \rangle_J}. \tag{2.25}$$

The *effective action* $\Gamma(\Phi_c)$ is defined via a Legendre transformation [18]

$$\Gamma(\Phi_c) = W(J) - \sum_i \int d^4 x J_i(x) \Phi_{c,i}(x). \tag{2.26}$$

It is therefore also a generating functional

$$\begin{aligned}
 \Gamma(\Phi_c) = & \sum_{n_1, \dots, n_N} \frac{1}{n_1! \dots n_N!} \int d^4 x_1 \dots d^4 x_{n_1} \dots d^4 w_{n_N} \times \Gamma^{(n_1, \dots, n_N)}(x_1, \dots, w_{n_N}) \\
 & \times \Phi_1(x_1) \dots \Phi_1(x_{n_1}) \dots \Phi_i(w_{n_N}).
 \end{aligned} \tag{2.27}$$

³Connected Feynman diagrams are diagrams without any disconnected vacuum loops [18].

$\Gamma^{(n_1, \dots, n_N)}(x_1, \dots, w_{n_N})$ label the one-particle irreducible (1PI) Greens functions that are constructed by the sum of all 1PI Feynman diagrams.⁴ Expanding the effective action of Eq. (2.26) in powers of external momenta around the point of vanishing external momenta at a constant field value $\varphi_{c,i}$ of the classical field $\Phi_{c,i}$ we get

$$\Gamma[\Phi_c] = \int d^4x \left\{ -V(\varphi_c) + \frac{1}{2} \partial_\mu \Phi_c(x) \partial^\mu \Phi_c(x) Z(\varphi_c) + \dots \right\}. \quad (2.28)$$

The first term in the external momenta expansion, $V(\varphi_c)$, is the so-called *effective potential* [41]. It can be diagrammatically calculated by summing all diagrams with zero external momenta and only external scalar fields.

The theory shows spontaneous symmetry breaking (SSB) if [41]

$$\frac{\delta \Gamma[\Phi_c(x)]}{\delta \Phi_c(x)} = 0, \quad \text{when } \Phi_c(x) \neq 0. \quad (2.29)$$

Assuming Poincaré-invariance, the fields are not space-time dependent and φ_c is constant. The Poincaré-invariant theory shows SSB if

$$\frac{dV(\varphi_c)}{d\varphi_c} = 0, \quad \text{when } \varphi_c \neq 0. \quad (2.30)$$

For space-time independent fields Φ_c , Eq. (2.28) simplifies and the effective action and the full effective potential are connected via the spacetime volume Ω

$$\Gamma[\varphi_c] = -\Omega V(\varphi_c). \quad (2.31)$$

In addition to the true ground state, also 1PI Greens functions can be calculated from the effective potential. Evaluating the n th derivative of $V(\varphi_c)$ at $\varphi_c = 0$ gives the n -point 1PI Greens function in the limit of vanishing external momenta.

A complete calculation of V would involve the sum over an infinite amount of Feynman diagrams. It is possible to do an expansion in terms of numbers of loops that can be directly related to an expansion in \hbar [41],

$$V = V^{(0)} + \hbar V^{(1)} + \mathcal{O}(\hbar^2) \quad \text{and} \quad (2.32)$$

$$\Gamma[\varphi_c] = -\Omega V^{(0)}(\varphi_c) + \frac{i\hbar}{2} \log \det \mathcal{D}^{-1} + \mathcal{O}(\hbar^2). \quad (2.33)$$

The logarithm of the determinant of the inverse propagator \mathcal{D}^{-1} can be rewritten as a trace. The trace can then be expressed as a sum over its eigenvalues [18]. In case of a pure

⁴1PI Feynman diagrams are connected diagrams that cannot be separated into two diagrams by cutting one internal line [18].

scalar theory with $\mathcal{D}^{-1} = (\partial^2 + m^2)$ defined in position space, this reads

$$\begin{aligned}
\log \det \mathcal{D}^{-1} &= \text{Tr} \log \mathcal{D}^{-1} \\
&= \int d^4x \langle x | \log \mathcal{D}^{-1} | x \rangle \\
&= \int d^4x \int \frac{d^4k}{(2\pi)^4} \int \frac{d^4k'}{(2\pi)^4} \langle x | k \rangle \langle k | \log \mathcal{D}^{-1} | k' \rangle \langle k' | x \rangle \\
&= \int d^4x \int \frac{d^4k}{(2\pi)^4} \log(-k^2 + m^2) \int d^4k' \langle x | k \rangle \delta^{(4)}(k - k') \langle k' | x \rangle \\
&= \int d^4x \int \frac{d^4k}{(2\pi)^4} \log(-k^2 + m^2) \\
&= \Omega \int \frac{d^4k}{(2\pi)^4} \log(-k^2 + m^2),
\end{aligned} \tag{2.34}$$

where we used that $1 = \int \frac{d^4k}{(2\pi)^4} |k\rangle \langle k|$ and inserted the eigenvalues of the inverse propagator in momentum space $\langle k | \log \mathcal{D}^{-1} | k' \rangle = (2\pi)^4 \delta^{(4)}(k - k') \log(-k^2 + m^2)$. After performing a Wick rotation with $k_0 \rightarrow ik_4$ and comparing Eq. (2.31) with (2.33), the one-loop potential in a purely bosonic field theory reads

$$V^{(1)} = \frac{1}{2} \int \frac{d^4k_E}{(2\pi)^4} \log(k_E^2 + m_{\text{eff}}^2). \tag{2.35}$$

The effective mass matrix m_{eff}^2 in a theory with spontaneous symmetry breaking is calculated considering the inverse propagator in the true ground state where the field Φ_c obtains the VEV $\langle \varphi \rangle$

$$m_{\text{eff},ij}^2 = \left. \frac{\partial^2 V^{(0)}}{\partial \Phi_{c,i} \partial \Phi_{c,j}} \right|_{\Phi_c = \langle \varphi \rangle}. \tag{2.36}$$

2.5. Finite Temperature Field Theory

Quantum field theory at finite temperature can be formulated in the *Matsubara* formalism that was originally introduced in [49]. The thermal system of the hot early universe can be described by a *grand canonical ensemble*, therefore allowing particle and energy exchange with a heat bath of temperature T [50]. The *partition function* Z of a system at finite temperature $T = \beta^{-1}$ is ⁵

$$Z(\beta) = \text{Tr} e^{-\beta \hat{\mathcal{H}}}, \tag{2.37}$$

with $\mathcal{H} = H - \mu N$, the Hamiltonian of the grand canonical ensemble, the Hamiltonian operator H and the particle number operator N , as well as the chemical potential μ .

Observables at finite temperature are ensemble averages of operators \mathcal{O} , the so-called *Gibbs averages* [51]

$$\langle \mathcal{O} \rangle_\beta = Z(\beta)^{-1} \text{Tr} e^{-\beta \hat{\mathcal{H}}} \mathcal{O}. \tag{2.38}$$

Writing the operator as $\mathcal{O} = \mathcal{O}(x_1, x_2, \dots, x_n) \equiv \mathcal{O}_1(t_1, \mathbf{x}_1) \mathcal{O}_2(t_2, \mathbf{x}_2) \dots \mathcal{O}_n(t_n, \mathbf{x}_n)$ and inserting the explicit Heisenberg operator form of $\mathcal{O}_H(t, \mathbf{x}) = e^{i\hat{\mathcal{H}}t} \mathcal{O}_S e^{-i\hat{\mathcal{H}}t}$ we can rewrite

⁵We use natural units and set $k_B \equiv 1$.

Eq. (2.38)

$$\langle \mathcal{O}(x_1, x_2, \dots, x_n) \rangle_\beta = Z(\beta)^{-1} \text{Tr} e^{-\beta \hat{\mathcal{H}}} \mathcal{O}_1(t_1, \mathbf{x}_1) \mathcal{O}_2(t_2, \mathbf{x}_2) \dots \mathcal{O}_n(t_n, \mathbf{x}_n) \quad (2.39a)$$

$$= Z(\beta)^{-1} \text{Tr} e^{-\beta \hat{\mathcal{H}}} e^{i\mathcal{H}t_1} \mathcal{O}_1(0, \mathbf{x}_1) e^{-i\mathcal{H}t_1} \dots e^{i\mathcal{H}t_n} \mathcal{O}_n(0, \mathbf{x}_n) e^{-i\mathcal{H}t_n} \quad (2.39b)$$

$$= Z(\beta)^{-1} \text{Tr} e^{-\beta \hat{\mathcal{H}}} \cdot e^{-\beta \hat{\mathcal{H}}} e^{\beta \hat{\mathcal{H}}} \cdot e^{i\mathcal{H}t_1} \mathcal{O}_1(0, \mathbf{x}_1) \dots \mathcal{O}_n(0, \mathbf{x}_n) e^{-i\mathcal{H}t_n} \quad (2.39c)$$

$$= Z(\beta)^{-1} \text{Tr} e^{-\beta \hat{\mathcal{H}}} e^{\mathcal{H}(it_1 + \beta)} \mathcal{O}_1(0, \mathbf{x}_1) \dots \mathcal{O}_n(0, \mathbf{x}_n) e^{-\mathcal{H}(it_n + \beta)}. \quad (2.39d)$$

In step (2.39c) $1 = e^{-\beta \hat{\mathcal{H}}} e^{\beta \hat{\mathcal{H}}}$ is inserted and in step (2.39d) we use the cyclicity of the trace. By comparing Eq. (2.39b) and (2.39d) we find that the equality only holds if

$$it_m \rightarrow it_m + \beta \quad (2.40)$$

for arbitrary $m \in \{1, \dots, n\}$. Consequently, in contrast to the zero temperature Greens functions with boundary conditions for $t_m = \pm\infty$, the finite temperature Greens functions are periodic in imaginary time it_m with period β [51]. This is the reason why the Matsubara formalism is often called *imaginary time formalism* [50].

The finite-temperature two-point Greens function can be written as [50]

$$G_\beta(\tau - \tau') = \left\langle \mathcal{T}_\tau \left(\phi_H(\tau) \phi_H^\dagger(\tau') \right) \right\rangle_\beta \quad (2.41a)$$

$$= Z(\beta)^{-1} \text{Tr} e^{-\beta \hat{\mathcal{H}}} \mathcal{T}_\tau \left(\phi_H(\tau) \phi_H^\dagger(\tau') \right) \quad (2.41b)$$

$$= Z(\beta)^{-1} \text{Tr} e^{-\beta \hat{\mathcal{H}}} \left[\Theta(\tau - \tau') \phi_H(\tau) \phi_H^\dagger(\tau') \pm \Theta(\tau' - \tau) \phi_H^\dagger(\tau') \phi_H(\tau) \right]. \quad (2.41c)$$

In Eq. (2.41c) the time ordering at finite temperature \mathcal{T}_τ is written out explicitly, (+) corresponds to bosonic, (−) to fermionic Heisenberg fields ϕ_H . From Eq. (2.40) we know that G_β is periodic with period β , therefore $|\tau - \tau'| \leq \beta$. Using the cyclicity of the trace one can conclude that

$$G_\beta(\tau < 0) = \pm G_\beta(\tau + \beta). \quad (2.42)$$

Because the Greens functions are defined on a finite time interval, the Fourier transform can only involve discrete frequencies, the so-called *Matsubara* frequencies ω_n with $n \in \mathbb{N}_0$. Using Eq. (2.42), we can write the Fourier-transformed Greens function as [50]

$$G_\beta(\omega_n) = \frac{1}{2} \int_{-\beta}^{\beta} d\tau e^{i\omega_n \tau} G_\beta(\tau) \quad (2.43a)$$

$$= \pm \frac{1}{2} \int_{-\beta}^0 d\tau e^{i\omega_n \tau} G_\beta(\tau + \beta) + \frac{1}{2} \int_0^{\beta} d\tau e^{i\omega_n \tau} G_\beta(\tau) \quad (2.43b)$$

$$= \pm \frac{1}{2} \int_0^{\beta} d\tau e^{i\omega_n(\tau + \beta)} G_\beta(\tau) + \frac{1}{2} \int_0^{\beta} d\tau e^{i\omega_n \tau} G_\beta(\tau) \quad (2.43c)$$

$$= \frac{1}{2} \left(1 \pm e^{i\omega_n \beta} \right) \int_0^{\beta} d\tau e^{i\omega_n \tau} G_\beta(\tau) \quad (2.43d)$$

$$= \frac{1}{2} \left(1 \pm (-1)^n \right) \int_0^{\beta} d\tau e^{i\omega_n \tau} G_\beta(\tau). \quad (2.43e)$$

From Eq. (2.43e) we conclude that for bosons only *even* n and for fermions only *odd* n

lead to non-zero Greens functions. The Matsubara frequencies for bosons and fermions therefore are

$$\omega_n = \begin{cases} \frac{2n\pi}{\beta} & \text{for bosons with } n \in \mathbb{N}_0 \\ \frac{(2n+1)\pi}{\beta} & \text{for fermions.} \end{cases} \quad (2.44)$$

The finite temperature partition function can also be expressed in terms of the *path integral*. The zero temperature transition amplitude in the path integral formalism reads

$$\langle \phi(\mathbf{x}_1, t_1) | \phi(\mathbf{x}_2, t_2) \rangle = \langle \phi_1 | e^{-iH(t_1-t_2)} | \phi_2 \rangle = N' \int \mathcal{D}\phi e^{iS}. \quad (2.45)$$

For finite temperature we identify $-i\beta = t_1 - t_2$ and write

$$Z(\beta) = \text{Tr} e^{-\beta\hat{H}} = \int d\phi \langle \phi | e^{-\beta\hat{H}} | \phi \rangle = N' \int \mathcal{D}\phi e^{-\hat{S}_E}. \quad (2.46)$$

The imaginary time action S_E and \hat{S}_E are connected via

$$\hat{S}_E = S_E + \beta\mu N = \int_0^\beta d\tau \int d^3x \mathcal{L}_E + \beta\mu N. \quad (2.47)$$

The fields are periodic

$$\phi(\mathbf{x}, \beta) = \pm \phi(\mathbf{x}, 0). \quad (2.48)$$

The procedure of obtaining Feynman rules from the path integral is the same as for zero temperature field theory [18]. While the vertices remain unchanged when going from zero to finite temperature field theory, the propagators receive temperature-dependent contributions. The bosonic and fermionic momentum space causal two-point Greens functions in finite temperature field theory read

$$G_{\beta, s_0}(\mathbf{k}, \omega_n) = \frac{1}{\omega_n^2 + \mathbf{k}^2 + m^2}, \quad (2.49)$$

$$G_{\beta, s_{1/2}}(\mathbf{k}, \omega_n) = \frac{\gamma^0 \omega_n + \boldsymbol{\gamma} \mathbf{k} - m}{\omega_n^2 + \mathbf{k}^2 + m^2}. \quad (2.50)$$

γ^μ are the Dirac matrices and $s_{0, 1/2}$ label the spin quantum numbers of bosons and fermions.

We summarize, at finite temperature the space-time topology changes as

$$\mathbb{R}^4 \rightarrow \mathbb{R}^3 \times S^1. \quad (2.51)$$

S^1 is identified with the one-dimensional sphere. Periodicity in imaginary time leads to discretization of energy defining the Matsubara frequencies. Equations (2.44) and (2.51) indicate the following replacements when going from zero to finite temperature field theory

$$\int \frac{d^4k}{(2\pi)^4} = \int \frac{dk_0}{2\pi} \int \frac{d\mathbf{k}}{(2\pi)^3} \rightarrow T \sum_{n \in \mathbb{Z}} \int \frac{d^3k}{(2\pi)^3}. \quad (2.52)$$

The imaginary time formalism trades the time variable for the equilibrium temperature. It is therefore applicable for static systems that are in thermal equilibrium. However, this is not true for the hot early universe in the vicinity of the electroweak phase transition that we want to describe. It is possible to introduce a slow time dependence into the imaginary

time formalism through analytic continuation [50]. Systems far from thermal equilibrium can be described via the so-called *real time path formalism* and its special case, the *closed time path formalism* [50]. As the terminology indicates, it involves a time integration along a path on the real axis in positive direction that is closed in the complex time plane.

In the context of this work, we apply perturbation theory in the hot early universe. We study EWPTs assuming that we are approximately close enough to the equilibrium that the imaginary time formalism is still applicable.

2.6. One-Loop Effective Potential at Finite Temperature

By applying Eq. (2.52) to Eq. (2.35), we can write the one-loop effective potential at finite temperature for bosonic fields as

$$V^{(1)} = \frac{T}{2} \sum_{n \in \mathbb{Z}} \int \frac{d^3 k}{(2\pi)^3} \log(\omega_n^2 + \omega_k^2), \quad \text{with } \omega_k^2 \equiv \mathbf{k}^2 + m^2. \quad (2.53)$$

Using the method of [36] the finite temperature one-loop bosonic effective potential can be further split into two parts, a temperature-independent *Coleman-Weinberg* potential V_{CW} and a temperature-dependent part V_T [52, 53],

$$V^{(1)} = \int \frac{d^3 k}{(2\pi)^3} \frac{\omega_k}{2} + \int \frac{d^3 k}{(2\pi)^3} \frac{1}{\beta} \log(1 - e^{-\beta\omega_k}) \equiv V_{\text{CW}} + V_T. \quad (2.54)$$

The temperature-independent Coleman-Weinberg contribution is UV divergent. As no further UV divergences can be generated at finite temperature, performing $\overline{\text{MS}}$ renormalization at zero temperature is sufficient in order to cure the UV divergences [50]. This procedure of renormalization is further discussed in Chapter 4. One obtains the UV-finite bosonic Coleman-Weinberg potential in the $\overline{\text{MS}}$ scheme at the renormalization scale μ as [41]

$$V_{\text{CW}}^{\overline{\text{MS}}} = \frac{m^4}{64\pi^2} \left[\log\left(\frac{m^2}{\mu^2}\right) - k_X \right], \quad (2.55)$$

with the renormalization constant k_X

$$k_X = \begin{cases} \frac{5}{6}, & \text{for gauge bosons} \\ \frac{3}{2}, & \text{otherwise} \end{cases}. \quad (2.56)$$

The complete effective potential at finite temperature up to one-loop level reads

$$V = V^{(0)} + V^{(1)} \equiv V^{(0)} + V_{\text{CW}} + V_T. \quad (2.57)$$

The temperature-dependent part V_T of the one-loop bosonic effective potential can be written defining the *thermal* bosonic function J_- [36, 52, 53]

$$V_T = \int \frac{d^3 k}{(2\pi)^3} \frac{1}{\beta} \log(1 - e^{-\beta\omega_k}) \equiv \frac{1}{2\pi^2\beta^4} J_-(m^2\beta^2) \quad (2.58)$$

with

$$J_{\pm}(x^2) = \int_0^{\infty} dk k^2 \log\left(1 \pm e^{-\sqrt{k^2+x^2}}\right). \quad (2.59)$$

So far, we only considered a purely bosonic theory. The contributions from vector bosons and fermions to the effective potential can be calculated analogously. In Sec. 4.2 we give the one-loop effective potential at finite temperature for a general quantum field theory involving scalars, fermions and gauge bosons using the universal notation of [54]. Also in this most general case, the effective potential splits into a temperature-independent Coleman-Weinberg potential and a temperature-dependent part.

2.7. Resummation

The effective potential suffers from so-called *infrared* (IR) divergences when $\mathbf{k} \rightarrow 0$ for the bosonic Matsubara zero modes with $n = 0$,

$$V \propto \log \mathcal{D}^{-1} \xrightarrow{\mathbf{k} \rightarrow 0} \infty \quad \text{for } n = 0. \quad (2.60)$$

These infrared divergences lead to a breakdown of the perturbative expansion close to the phase transition [52].

It was shown in [55] that the NLO contribution to the temperature-dependent part of the effective potential in the expansion in terms of the self-coupling λ is of order $\mathcal{O}(\lambda^{3/2})$, not of order $\mathcal{O}(\lambda^2)$. The order $\mathcal{O}(\lambda^{3/2})$ is given by the so-called *ring* or *daisy* corrections [56]. If all ring diagrams are included, the problematic IR divergences cancel and we are able to perform a complete perturbative IR finite NLO calculation of the effective potential.

Ring diagrams account for non-perturbative significant long-distance effects. They are the dominant parts of the two-loop graph and can be calculated as self-energy corrections in the infrared limit $\mathbf{k} \rightarrow 0$ and in the *hard thermal loop approximation*⁶ [57]

$$\frac{m}{T} \ll 1. \quad (2.61)$$

Including the infinite sum of all possible ring diagrams in a diagrammatic calculation is equivalent to performing *resummation* by including the *thermal* masses into the calculation. Thermal masses arise from one-loop diagrams shown in Fig. 2.2 that yield quadratic divergences of order $\propto T^2$ [58]. In a scalar field theory with quartic coupling λ , the one-loop polarization tensor of Fig. 2.2 at finite temperature in the infrared and hard thermal loop limit is given by [58]

$$\Pi^{(1)}(\omega_n, \mathbf{k}) \xrightarrow{\mathbf{k} \rightarrow 0, m/T \ll 1} \Pi^{(1)}(0) = 3\lambda T \sum_{n \in \mathbb{Z}} \int \frac{d^3k}{(2\pi)^3} \frac{1}{\omega_n^2 + \omega_k^2} \quad (2.62)$$

$$= \lambda \frac{T^2}{4} \left(1 + \mathcal{O}\left(\frac{m}{T}\right) \right). \quad (2.63)$$

As suggested by *Parwani* in [59], resummation in finite temperature effective field theory can be performed by replacing all masses in the effective potential with the thermal masses

$$m^2 \rightarrow m^2 + \Pi^{(1)}(0). \quad (2.64)$$

The method proposed in [58], that we will refer to as the *Arnold-Espinosa* method, treats the Matsubara modes differently. As shown in [58], only contributions for heavy $n \neq 0$ but not for light $n = 0$ modes can be treated perturbatively. After the heavy modes

⁶This approximation is sufficient, because the ring diagram contribution is negligible in the opposite case when $m \sim T$ as shown in [55].

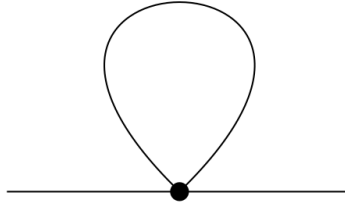


Figure 2.2.: Thermal mass correction in a purely bosonic field theory

are integrated out, only the zero modes are resummed in the Arnold-Espinosa method. Therefore, in contrast to the Parwani method, one does not suffer from the mixture of different orders in perturbation theory. The thermal mass corrections for a general quantum field theory in the notation of [54] are presented in Sec. 4.2.

3. CP in the Dark

A minimal approach to describe physics beyond the Standard Model in a *bottom up* way is the extension of the scalar sector. Being experimentally the least resolved sector of the SM, the scalar sector therefore has the potential to turn out to be more complex than postulated in the SM. A precisely measured quantity that restricts multiplet extensions of the SM scalar sector is the ρ parameter [60]. For an electroweak $SU(2)_L \times U(1)_Y$ gauge theory with n scalar doublets with weak isospins I_i , weak hypercharges Y_i and VEVs v_i the ρ parameter reads

$$\rho = \frac{\sum_{i=1}^n v_i [4I_i(I_i + 1) - Y_i^2]}{\sum_{i=1}^n 2Y_i^2 v_i}. \quad (3.1)$$

For the SM Higgs sector with one $SU(2)_L$ doublet with $I = \frac{1}{2}$, $Y = 1$, ρ is exactly $\rho_{\text{SM}} = 1$. Experimentally, ρ is found to be close to the SM value [61],

$$\rho_{\text{obs}} = 1.00039 \pm 0.00019. \quad (3.2)$$

A special model describing physics beyond the SM is called CP in the Dark [14]. It features an N2HDM-like extended scalar sector with two scalar doublets Φ_1 and Φ_2 and a real scalar singlet Φ_S . Additionally, we require the Lagrangian to be invariant under the discrete \mathbb{Z}_2 symmetry

$$\Phi_1 \rightarrow \Phi_1, \quad \Phi_2 \rightarrow -\Phi_2, \quad \Phi_S \rightarrow -\Phi_S. \quad (3.3)$$

This \mathbb{Z}_2 symmetry rules out any tree-level flavor-changing neutral currents (FCNCs) which would conflict the experimental results that require that any such process is strongly suppressed.

Imposing this \mathbb{Z}_2 symmetry on the field content of an N2HDM, the most general scalar tree-level potential invariant under $SU(2)_L \times U(1)_Y$ is given by

$$\begin{aligned} V^{(0)} = & m_{11}^2 |\Phi_1|^2 + m_{22}^2 |\Phi_2|^2 + \frac{m_S^2}{2} \Phi_S^2 \\ & + [\text{Re}(A) + i \text{Im}(A)] \Phi_1^\dagger \Phi_2 \Phi_S + [\text{Re}(A) - i \text{Im}(A)] \Phi_2^\dagger \Phi_1 \Phi_S \\ & + \frac{\lambda_1}{2} |\Phi_1|^4 + \frac{\lambda_2}{2} |\Phi_2|^4 + \lambda_3 |\Phi_1|^2 |\Phi_2|^2 + \lambda_4 |\Phi_1^\dagger \Phi_2|^2 + \frac{\lambda_5}{2} [(\Phi_1^\dagger \Phi_2)^2 + (\Phi_2^\dagger \Phi_1)^2] \\ & + \frac{\lambda_6}{4} \Phi_S^4 + \frac{\lambda_7}{2} |\Phi_1|^2 \Phi_S^2 + \frac{\lambda_8}{2} |\Phi_2|^2 \Phi_S^2. \end{aligned} \quad (3.4)$$

The mass parameters m_{11}^2 , m_{22}^2 and m_S^2 and the quartic coupling parameters λ_{1-4} , λ_{6-8} are forced to be real by the imposed \mathbb{Z}_2 symmetry. The trilinear coupling A and the quartic

coupling λ_5 are in general complex. However, in the tree-level potential of Eq. (3.4) we absorb the complex phase of λ_5 into a basis change of the doublets. Then only A can acquire a non-zero imaginary part, $\text{Im}(A)$.

At the present vacuum with $T = 0 \text{ GeV}$ only the first doublet acquires a non-zero VEV v_1 . Thus, the imposed \mathbb{Z}_2 -symmetry of Eq. (3.3) is *unbroken*

$$\langle \Phi_1 \rangle|_{T=0 \text{ GeV}} = \frac{1}{\sqrt{2}} \begin{pmatrix} 0 \\ v_1 \end{pmatrix}, \quad \langle \Phi_2 \rangle|_{T=0 \text{ GeV}} = \begin{pmatrix} 0 \\ 0 \end{pmatrix} \quad \text{and} \quad \langle \Phi_S \rangle|_{T=0 \text{ GeV}} = 0. \quad (3.5)$$

Due to the \mathbb{Z}_2 -symmetry, the first scalar doublet Φ_1 is the only one that couples to the fermion sector. Consequently, v_1 describes the SM VEV $v_1 \equiv v = 246.22 \text{ GeV}$. The Yukawa sector is identical to the SM one. FCNCs are therefore automatically prohibited at tree level.

At arbitrary temperature T , we allow for a more general vacuum structure that is described by five VEVs. While in the first doublet, only the neutral CP -even scalar ζ_1 develops a VEV ω_1 , the real part of the charged scalar ρ_2 , the neutral CP -even ζ_2 and neutral CP -odd Ψ_2 field components of the second doublet and the singlet ζ_S acquire VEVs as

$$\Phi_1 = \frac{1}{\sqrt{2}} \begin{pmatrix} \rho_1 + i\eta_1 \\ \zeta_1 + \omega_1 + i\Psi_1 \end{pmatrix}, \quad \Phi_2 = \frac{1}{\sqrt{2}} \begin{pmatrix} \rho_2 + \omega_{\text{CB}} + i\eta_2 \\ \zeta_2 + \omega_2 + i(\Psi_2 + \omega_{\text{CP}}) \end{pmatrix}, \quad \Phi_S = \zeta_S + \omega_S. \quad (3.6)$$

Note, that we include a charge-breaking VEV ω_{CB} in the finite temperature vacuum structure, to be as general as possible. However, in the later analysis of Chapter 5 all points with $|\omega_{\text{CB}}| > 0$ are excluded due to non-physical behavior.

The tree-level potential $V^{(0)}$ is required to be minimal at the electroweak vacuum. The resulting *minimum conditions*

$$\left. \frac{\partial V^{(0)}}{\partial \Phi_a} \right|_{\Phi_i = \langle \Phi_i \rangle|_{T=0 \text{ GeV}}} = 0, \quad a, i \in \{1, 2, S\} \quad (3.7)$$

can be used to trade the potential parameter m_{11}^2 for the input parameters v_1 and λ_1 ,

$$m_{11}^2 = -\frac{1}{2}\lambda_1 v_1^2. \quad (3.8)$$

This equation is referred to as the *tadpole equation*.

Using the minimum condition of Eq. (3.8), the mass matrix in the gauge basis

$$\phi_i = \{\rho_1, \eta_1, \rho_2, \eta_2, \zeta_1, \Psi_1, \zeta_2, \Psi_2, \zeta_S\} \quad (3.9)$$

is diagonal for the Goldstone bosons $G^\pm \equiv \frac{1}{\sqrt{2}}(\rho_1 \pm i\eta_1)$ and $G^0 \equiv \frac{1}{\sqrt{2}}\Psi_1$, the SM-like Higgs boson $h \equiv \zeta_1$ and the charged scalars $H^\pm \equiv \frac{1}{\sqrt{2}}(\rho_2 \pm i\eta_2)$. They are mass eigenstates with

$$m_{G^\pm}^2 = m_{G^0}^2 = 0, \quad (3.10a)$$

$$m_h^2 = \lambda_1 v_1^2 \quad \text{and} \quad (3.10b)$$

$$m_{H^\pm}^2 = m_{22}^2 + \frac{1}{2}\lambda_3 v_1^2. \quad (3.10c)$$

The first doublet field and the charged component of the second doublet field written in terms of these mass eigenstates read

$$\Phi_1 = \begin{pmatrix} G^\pm \\ \frac{1}{\sqrt{2}}(h + v_1 + iG^0) \end{pmatrix}, \quad \Phi_2^\pm = H^\pm. \quad (3.11)$$

The neutral fields ζ_2 , Ψ_2 and ζ_s mix and generate three mass eigenstates h_1 , h_2 , h_3 which are obtained by the rotation

$$\begin{pmatrix} h_1 \\ h_2 \\ h_3 \end{pmatrix} = R \begin{pmatrix} \zeta_2 \\ \Psi_2 \\ \zeta_S \end{pmatrix}. \quad (3.12)$$

The orthogonal matrix R is parametrized by three angles α_1 , α_2 and α_3 as [14]

$$R = \begin{pmatrix} c_{\alpha_1}c_{\alpha_2} & s_{\alpha_1}c_{\alpha_2} & s_{\alpha_2} \\ -(c_{\alpha_1}s_{\alpha_2}s_{\alpha_3} + s_{\alpha_1}c_{\alpha_3}) & c_{\alpha_1}c_{\alpha_3} - s_{\alpha_1}s_{\alpha_2}s_{\alpha_3} & c_{\alpha_2}s_{\alpha_3} \\ -c_{\alpha_1}s_{\alpha_2}c_{\alpha_3} + s_{\alpha_1}s_{\alpha_3} & -(c_{\alpha_1}s_{\alpha_3} + s_{\alpha_1}s_{\alpha_2}c_{\alpha_3}) & c_{\alpha_2}c_{\alpha_3} \end{pmatrix}, \quad (3.13)$$

where we use $\sin(\alpha_i) \equiv s_{\alpha_i}$, $\cos(\alpha_i) \equiv c_{\alpha_i}$. The sub mass matrix of the neutral scalars reads

$$M_N^2 = \begin{pmatrix} m_{22}^2 + \frac{v_1^2}{2}\lambda_{345} & 0 & \text{Re}(A)v_1 \\ 0 & m_{22}^2 + \frac{v_1^2}{2}\bar{\lambda}_{345} & -\text{Im}(A)v_1 \\ \text{Re}(A)v_1 & -\text{Im}(A)v_1 & m_S^2 + \frac{v_1^2}{2}\lambda_7 \end{pmatrix}. \quad (3.14)$$

It can be diagonalized yielding the mass eigenvalues

$$RM_N^2R^T = \text{diag}(m_{h_1}^2, m_{h_2}^2, m_{h_3}^2). \quad (3.15)$$

The masses are chosen to have the hierarchy

$$m_{h_1} < m_{h_2} < m_{h_3}. \quad (3.16)$$

The doublet and real singlet fields transform under CP as

$$\Phi_{1,2}(t, \vec{x}) \xrightarrow{CP} \Phi_{1,2}^*(t, -\vec{x}), \quad \Phi_S(t, \vec{x}) \xrightarrow{CP} \Phi_S(t, -\vec{x}), \quad (3.17)$$

respectively. The vacuum of Eq. (3.5) is symmetric under these CP -transformations, hence CPV cannot result from SSB at $T = 0$ GeV.

A non-zero complex phase of A , $\text{Im}(A) \neq 0$, will break the invariance under transformations of Eq. (3.17). Moreover, as the neutral scalars h_1 , h_2 and h_3 are generated through a mixture of CP -even and odd states, they are states of mixed CP quantum number and enable CP -violating processes. Therefore, the CPV in the model CP in the Dark is *explicit* and introduced through $\text{Im}(A) \neq 0$.

The conservation of the \mathbb{Z}_2 symmetry of Eq. (3.3) introduces an additional quantum number, called *dark charge*. While all SM-like particles have dark charge +1, the charged scalar H^\pm and the neutral scalars h_{1-3} originating from the second doublet Φ_2 and the real singlet Φ_S have dark charge -1. All particles with dark charge -1 are called *dark particles*. The dark charge is exactly conserved up to all orders in perturbation theory. Dark particles can consequently only be produced and annihilated in pairs. Therefore, the lightest neutral

dark particle h_1 is stable and acts as a *particle dark matter* candidate.

Note, that this model features explicit CPV in the dark sector.¹ It is therefore not constrained by electric dipole moment (EDM) constraints.

¹So far only [62, 63] presented a three-doublet model that also includes a dark matter candidate and additional CPV.

4. Renormalization

A perturbative quantum field theory calculation suffers from UV divergences¹ that are relics of the fixed-order approximation and its lack of describing short-range effects. If a quantum field theory is renormalizable, these infinities cancel in a full-order calculation [18]. CP in the Dark, as a special N2HDM, is a renormalizable quantum field theory [64].

In order to be able to obtain finite physical results in a fixed-order calculation of a renormalizable quantum field theory, the procedure of regularization and renormalization is applied. First, the divergences are isolated through regularization. Second, renormalization is the formal procedure, where all infinities are systematically canceled. It is achieved through replacing every potentially infinite *bare* parameter or wave function (WF) of the Lagrangian by finite *renormalized* parameters or WFs and counterterms (CTs) or wave function renormalization constants (WFRCs). The CTs and WFRCs contain singularities that cancel the infinities of the fixed-order quantum field theory calculation order by order in perturbation theory.

A *renormalization scheme* with its renormalization conditions defines how the finite pieces are handled. By specifying the scheme one therefore gets a unique relation between bare and renormalized parameters. The $\overline{\text{MS}}$ scheme is defined by only absorbing the UV singularities into the CTs and WFRCs. The $\overline{\text{MS}}$ scheme also absorbs typical associated constants into the CTs and WFRCs, in addition to the singularity. In an on-shell (OS) scheme, the physical masses are *defined* as the real parts of the poles of the renormalized propagators [18].

4.1. Notation

In this thesis we follow the notation of [54] which is applied in the C++ code BSMP [65, 66]. Thus, we use a most general way of writing a quantum field theory Lagrangian for a gauge theory with fields of spin $s_X = 0, \frac{1}{2}, 1$. The scalar multiplets of the theory are built up by real scalar component fields Φ_i with $i = 1, \dots, N_0$ and $s_\Phi = 0$. The Weyl 2-spinors Ψ_I with $I = 1, \dots, N_{1/2}$ and $s_\Psi = \frac{1}{2}$ build up the fermion multiplets. The gauge bosons with $s_A = 1$ are associated with the 4-vectors $A_{a\mu}$. The gauge group index $a = 1, \dots, N_1$ labels them in the adjoint representation.

In this notation, the purely scalar, scalar-fermionic and scalar-gauge Lagrangian reads

$$-\mathcal{L}_S = L^i \Phi_i + \frac{1}{2!} L^{ij} \Phi_i \Phi_j + \frac{1}{3!} L^{ijk} \Phi_i \Phi_j \Phi_k + \frac{1}{4!} L^{ijkl} \Phi_i \Phi_j \Phi_k \Phi_l, \quad (4.1a)$$

$$-\mathcal{L}_F = \frac{1}{2} Y^{IJ} \Psi_I \Psi_J + \frac{1}{2} Y^{IJK} \Psi_I \Psi_J \Phi_k + \text{c.c.}, \quad (4.1b)$$

$$-\mathcal{L}_{SG} = \frac{1}{4} G^{abij} A_{a\mu} A_b^\mu \Phi_i \Phi_j + G^{aij} A_{a\mu} \Phi_i \partial^\mu \Phi_j. \quad (4.1c)$$

¹If divergences in loop calculations appear for loop momenta $l \rightarrow \infty$, or high frequency, they are called UV divergences. Divergences for $l \rightarrow 0$ or low frequencies are called IR divergences. In the context of an EPA the IR divergences are treated through resummation as described in Sec. 2.7.

The tensors $\{L^i, L^{ij}, L^{ijk}, L^{ijkl}\}$ contain all couplings between scalar fields in the gauge basis. Y^{IJ} is the quadratic fermion coupling matrix. Y^{IJK} are Yukawa couplings between two fermions and one scalar field. Gauge-basis couplings between two scalar fields and one or two gauge fields are denoted by G^{aij} and G^{abij} .

After SSB the scalar fields are written as $\Phi_i(x) = \omega_i + \phi_i(x)$ with the VEVs ω_i and the fluctuations ϕ_i . The Lagrangian in the Λ -basis or *mass* basis reads

$$-\mathcal{L}_S = \Lambda + \Lambda_{(S)}^i \phi_i + \frac{1}{2!} \Lambda_{(S)}^{ij} \phi_i \phi_j + \frac{1}{3!} \Lambda_{(S)}^{ijk} \phi_i \phi_j \phi_k + \frac{1}{4!} \Lambda_{(S)}^{ijkl} \phi_i \phi_j \phi_k \phi_l, \quad (4.2a)$$

$$-\mathcal{L}_F = \frac{1}{2} M^{IJ} \Psi_I \Psi_J + \frac{1}{2} Y^{IJK} \Psi_I \Psi_J \phi_k + \text{c.c.}, \quad (4.2b)$$

$$-\mathcal{L}_{SG} = \frac{1}{2} \Lambda_{(G)}^{ab} A_{a\mu} A_b^\mu + \frac{1}{2} \Lambda_{(G)}^{abi} A_{a\mu} A_b^\mu \phi_i + \frac{1}{4} \Lambda_{(G)}^{abij} A_{a\mu} A_b^\mu \phi_i \phi_j + G^{aij} A_{a\mu} \phi_i \partial^\mu \phi_j. \quad (4.2c)$$

The Λ -tensors read [54]

$$\Lambda \equiv V^{(0)}(\omega_i) = L^i \omega_i + \frac{1}{2!} L^{ij} \omega_i \omega_j + \frac{1}{3!} L^{ijk} \omega_i \omega_j \omega_k + \frac{1}{4!} L^{ijkl} \omega_i \omega_j \omega_k \omega_l, \quad (4.3a)$$

$$\Lambda_{(S)}^i \equiv L^i + L^{ij} \omega_j + \frac{1}{2!} L^{ijk} \omega_j \omega_k + \frac{1}{3!} L^{ijkl} \omega_j \omega_k \omega_l, \quad (4.3b)$$

$$\Lambda_{(S)}^{ij} \equiv L^{ij} + L^{ijk} \omega_k + \frac{1}{2!} L^{ijkl} \omega_k \omega_l, \quad (4.3c)$$

$$\Lambda_{(S)}^{ijk} \equiv L^{ijk} + L^{ijkl} \omega_l, \quad (4.3d)$$

$$\Lambda_{(S)}^{ijkl} \equiv L^{ijkl}, \quad (4.3e)$$

$$\Lambda_{(G)}^{ab} \equiv \frac{1}{2!} G^{abij} \omega_i \omega_j, \quad (4.3f)$$

$$\Lambda_{(G)}^{abi} \equiv G^{abij} \omega_j, \quad (4.3g)$$

$$\Lambda_{(G)}^{abij} \equiv G^{abij}, \quad (4.3h)$$

$$\Lambda_{(F)}^{IJ} \equiv M^{*IL} M_L^J, \quad M^{IJ} \equiv Y^{IJ} + Y^{IJK} \omega_k. \quad (4.3i)$$

$\Lambda_{(S)}^{ij}$, $\Lambda_{(G)}^{ab}$ and M^{IJ} are the mass-squared matrices of the scalars (S), gauge bosons (G) and fermions (F), respectively.

4.2. $\overline{\text{MS}}$ Renormalization of the Effective Potential

The occurring infinities in a fixed-order calculation of a renormalizable quantum field theory can be treated and consistently absorbed into CTs during the process of renormalization. Using the EPA up to one-loop order at finite temperature we write [65]

$$V(\vec{\omega}, T) \equiv V(\vec{\omega}) + V_T(\vec{\omega}, T) \equiv V^{(0)}(\vec{\omega}) + V_{\text{CW}}(\vec{\omega}) + V_T(\vec{\omega}, T). \quad (4.4)$$

The temperature-independent contributions $V(\vec{\omega})$ are split up into the tree-level potential $V^{(0)}$ and the one-loop Coleman-Weinberg potential V_{CW} . As already discussed in Sec. 2.6, the renormalization of the UV-divergent Coleman-Weinberg potential is sufficient to cure the UV divergences of the one-loop finite temperature effective potential. The temperature-dependent potential V_T is UV finite [50].

The Coleman-Weinberg potential V_{CW} in the $\overline{\text{MS}}$ scheme is given in terms of the general

mass-squared matrices $\Lambda_{(X)}^{xy}$ as [41]

$$V_{\text{CW}} = \frac{\epsilon}{4} \sum_{X=S,G,F} (-1)^{2s_X} (1 + 2s_X) \text{Tr} \left[\left(\Lambda_{(X)}^{xy} \right)^2 \left(\log \left(\frac{1}{\mu^2} \Lambda_{(X)}^{xy} \right) - k_X \right) \right] \quad (4.5)$$

with $\epsilon = \frac{1}{(4\pi)^2}$ and $xy \in \{ij, ab, IJ\}$, $X \in \{(S), (G), (F)\}$. The Landau gauge is used.² The values of the renormalization constant k_X are

$$k_X = \begin{cases} \frac{5}{6}, & \text{for gauge bosons} \\ \frac{3}{2}, & \text{otherwise} \end{cases}. \quad (4.6)$$

In BSMPT [65, 66] the renormalization scale μ is set to $\mu = v(T = 0 \text{ GeV}) = 246.22 \text{ GeV}$.

The temperature-dependent contribution $V_T(\vec{\omega}, T)$ can also be expressed with the general mass-squared matrices $\Lambda_{(X)}^{xy}$ [36, 52, 53],

$$V_T(\vec{\omega}, T) = \sum_{X=S,G,F} (-1)^{2s_X} (1 + 2s_X) \frac{T^4}{2\pi^2} J_{\pm} \left(\frac{\Lambda_{(X)}^{xy}}{T^2} \right). \quad (4.7)$$

The thermal integrals for fermions and bosons J_{\pm} are defined as [36, 52, 53]

$$J_{\pm}(x^2) = \text{Tr} \left[\int_0^{\infty} dk k^2 \log \left(1 \pm \exp \left(-\sqrt{k^2 + x^2} \right) \right) \right], \quad (4.8)$$

where the $+$ ($-$) refers to fermions (bosons). The trace is calculated by summation over the eigenvalues of the corresponding matrix. The daisy corrections to the scalar $\Pi_{(S)}^{ij}$ and gauge boson $\Pi_{(G)}^{ab}$ masses that are needed for resummation [55] (see Sec. 2.7) can also be expressed in terms of tensors [65],

$$\begin{aligned} \Pi_{(S)}^{ij} \equiv & \frac{T^2}{12} \left[(-1)^{2s_S} (1 + 2s_S) \sum_{k=1}^{N_0} L^{ijkk} + (-1)^{2s_G} (1 + 2s_G) \sum_{a=1}^{N_1} G^{aa ij} + \right. \\ & \left. (-1)^{2s_F} (1 + 2s_F) \frac{1}{2} \sum_{I,J=1}^{N_{1/2}} \left(Y^{*IJj} Y_{IJ}^i + Y^{*IJi} Y_{IJ}^j \right) \right], \end{aligned} \quad (4.9)$$

$$\Pi_{(G)}^{ab} \equiv T^2 \frac{2}{3} \left(\frac{\tilde{n}_H}{8} + 5 \right) \frac{1}{\tilde{n}_H} \sum_{m=1}^{N_0} \Lambda_{(G)}^{aamm} \delta_{ab}, \quad (4.10)$$

where $\tilde{n}_H \leq N_0$ is the number of Higgs fields that couple to the gauge bosons. The *Parwani* method [59] corresponds to the replacement of all masses by the thermal masses as

$$\Lambda_{(X)}^{xy} \rightarrow \Lambda_{(X)}^{xy} + \Pi_{(X)}^{xy} \quad \text{with} \quad xy \in \{ij, ab\}, X \in \{(S), (G)\}. \quad (4.11)$$

In the *Arnold-Espinosa* method [58] only the Matsubara zero modes are resummed. The zero-mode resummation corresponds to the following replacement in the temperature-

²Landau gauge corresponds to the choice $\xi = 0$ in general R_{ξ} gauge. Then the gauge boson propagators are purely transverse and there are no ghost contributions. Gauge dependence in the EPA is further discussed in e.g. [36, 39, 67, 68].

dependent potential V_T ,

$$V_T(\vec{\omega}, T) \rightarrow V_T(\vec{\omega}, T) + V_{\text{ring}}(\vec{\omega}, T) \quad \text{with} \quad (4.12)$$

$$V_{\text{ring}}(\vec{\omega}, T) = -\frac{T}{2\pi} \sum_{x=1}^{N_X} \left((\bar{m}_x^2)^{3/2} - (m_x^2)^{3/2} \right) \quad \text{with} \quad x \in \{i, a\}, X \in \{(S), (G)\}, \quad (4.13)$$

with m_x^2 being the eigenvalue of $\Lambda_{(X)}^{xy}$. The temperature or Debye-corrected masses \bar{m}_x^2 can be calculated directly by diagonalizing the Debye corrected mass matrix $\Lambda_{(X)}^{xy} + \Pi_{(X)}^{xy}$ and determining its eigenvalues.

4.3. Treatment of Finite Pieces

After resummation in Sec. 2.7 and renormalization in Sec. 4.2, the one-loop corrected effective potential of Eq. (4.4) is IR and UV finite.

Scalar mixing angles and masses that are obtained from the one-loop corrected potential now correspond to the one-loop corrected angles and masses in the approximation of vanishing external momenta. With the prospect of performing efficient parameter scans and comparing experimental and theoretical results, it is convenient to redefine the finite pieces of the CT potential such that the scalar mixing angles and masses exactly equal their LO values. The LO-fixed masses can then be used as input for the parameter scans. The conventional treatment of finite pieces for angles and masses was first introduced in [69] and is applied to CP in the Dark in Sec. 4.3.1.

In the context of this work, we found that in case of explicitly CPV models the *conventional* mass scheme as proposed in [65, 66, 69–71] is not sufficient in order to constrain all scalar masses to their LO values as it lacks loop-induced CPV contributions. In Sec. 4.3.2 we introduce a *modified* mass scheme for CP in the Dark that is capable of exactly constraining the scalar masses and angles that are obtained from the one-loop corrected effective potential to their LO values.

4.3.1. Conventional Mass Scheme

In the conventional mass scheme [65, 66, 69–71] a CT potential V_{CT} is constructed by replacing the N_p bare parameters $p_i^{(0)}$ of the tree-level potential with $i \in \{1, \dots, N_p\}$ by the renormalized parameters p_i and *finite*³ CTs δp_i as

$$p_i^{(0)} \rightarrow p_i + \delta p_i. \quad (4.14)$$

Additionally, tadpole CTs δT for the $N_v \leq N_{\text{Higgs}}$ field directions that are allowed to develop a non-zero VEV at finite temperature are included. In a strict one-loop calculation only terms up to $\mathcal{O}(\delta p)$ are taken into account. A general expression of V_{CT} reads [65, 66, 69–71]

$$V_{\text{CT}} = \sum_{i=1}^{N_p} \frac{\partial V^{(0)}}{\partial p_i} \delta p_i + \sum_{k=1}^{N_v} \delta T_k(\phi_k + \omega_k). \quad (4.15)$$

³The $\overline{\text{MS}}$ renormalized one-loop corrected effective potential is UV finite. Any additionally introduced CT is therefore UV finite.

The CT potential is added to the one-loop corrected effective potential in Eq. (4.4). The full one-loop corrected effective potential then reads

$$V = V^{(0)} + V_{\text{CW}} + V_T + V_{\text{CT}}. \quad (4.16)$$

Applying Eq. (4.15) to the tree-level potential in Eq. (3.4) results in the *conventional* CT potential for CP in the Dark

$$\begin{aligned} V_{\text{CT}} = & \delta m_{11}^2 |\Phi_1|^2 + \delta m_{22}^2 |\Phi_2|^2 + \frac{\delta m_S^2}{2} \Phi_S^2 \\ & + [\delta \text{Re}(A) + i\delta \text{Im}(A)] \Phi_1^\dagger \Phi_2 \Phi_S + [\delta \text{Re}(A) - i\delta \text{Im}(A)] \Phi_2^\dagger \Phi_1 \Phi_S \\ & + \frac{\delta \lambda_1}{2} |\Phi_1|^4 + \frac{\delta \lambda_2}{2} |\Phi_2|^4 + \delta \lambda_3 |\Phi_1|^2 |\Phi_2|^2 + \delta \lambda_4 |\Phi_1^\dagger \Phi_2|^2 + \frac{\delta \lambda_5}{2} [(\Phi_1^\dagger \Phi_2)^2 + (\Phi_2^\dagger \Phi_1)^2] \\ & + \frac{\delta \lambda_6}{4} \Phi_S^4 + \frac{\delta \lambda_7}{2} |\Phi_1|^2 \Phi_S^2 + \frac{\delta \lambda_8}{2} |\Phi_2|^2 \Phi_S^2 \\ & + \delta T_{\text{CB}}(\rho_2 + \omega_{\text{CB}}) + \delta T_1(\zeta_1 + \omega_1) \\ & + \delta T_2(\zeta_2 + \omega_2) + \delta T_{\text{CP}}(\Psi_2 + \omega_{\text{CP}}) + \delta T_S(\zeta_S + \omega_S). \end{aligned} \quad (4.17)$$

In order to constrain the NLO scalar mixing angles and masses to their LO values, the following renormalization conditions are applied [65, 66, 69–71]

$$\partial_{\phi_i} V^{(0)} \Big|_{\phi=\langle\phi^c\rangle|_{T=0 \text{ GeV}}} \equiv \partial_{\phi_i} V(T=0 \text{ GeV}) \Big|_{\phi=\langle\phi^c\rangle|_{T=0 \text{ GeV}}}, \quad (4.18a)$$

$$\partial_{\phi_i} \partial_{\phi_j} V^{(0)} \Big|_{\phi=\langle\phi^c\rangle|_{T=0 \text{ GeV}}} \equiv \partial_{\phi_i} \partial_{\phi_j} V(T=0 \text{ GeV}) \Big|_{\phi=\langle\phi^c\rangle|_{T=0 \text{ GeV}}}. \quad (4.18b)$$

The scalar fields ϕ_i of the gauge basis are labeled as follows

$$\phi_i = \{\rho_1, \eta_1, \rho_2, \eta_2, \zeta_1, \Psi_1, \zeta_2, \Psi_2, \zeta_S\}. \quad (4.19)$$

The field configuration at $T = 0 \text{ GeV}$ is denoted by $\langle\phi^c\rangle|_{T=0 \text{ GeV}}$,

$$\langle\phi^c\rangle|_{T=0 \text{ GeV}} = \{0, 0, 0, 0, v_1, 0, 0, 0, 0\} \quad \text{and} \quad v_1 \equiv v = 246.22 \text{ GeV}. \quad (4.20)$$

The conditions in Eq. (4.18) ensure that the electroweak minimum is still a *local* minimum at NLO. Only parameter points where the electroweak minimum is still the *global* minimum at $T = 0 \text{ GeV}$ are NLO stable and are further considered in the scan of **BSMPT** (see Sec. 5.1.2). Inserting the one-loop potential (4.16) into Eq. (4.18) implies the following renormalization conditions on V_{CT}

$$\partial_{\phi_i} (V_{\text{CT}} + V_{\text{CW}}) \Big|_{\phi=\langle\phi^c\rangle|_{T=0 \text{ GeV}}} = 0, \quad (4.21a)$$

$$\partial_{\phi_i} \partial_{\phi_j} (V_{\text{CT}} + V_{\text{CW}}) \Big|_{\phi=\langle\phi^c\rangle|_{T=0 \text{ GeV}}} = 0. \quad (4.21b)$$

We use the notation

$$N_\phi^{\text{CW}} \equiv \partial_\phi V_{\text{CW}}, \quad (4.22a)$$

$$H_{\phi_i \phi_j}^{\text{CW}} \equiv \partial_{\phi_i} \partial_{\phi_j} V_{\text{CW}}. \quad (4.22b)$$

Equations (4.21a) and (4.21b) yield a system of in total 16 equations for 18 CTs. 13 of the 16 equations are linearly independent. Three identities between derivatives of the V_{CW} are

required for a consistent solution, namely

$$H_{\rho_1\rho_1}^{\text{CW}} = H_{\Psi_1\Psi_1}^{\text{CW}}, \quad (4.23a)$$

$$H_{\eta_1\eta_1}^{\text{CW}} = H_{\Psi_1\Psi_1}^{\text{CW}}, \quad (4.23b)$$

$$H_{\rho_2\rho_2}^{\text{CW}} = H_{\eta_2\eta_2}^{\text{CW}}. \quad (4.23c)$$

Equations (4.23) are checked for every scanned parameter point and are found to be fulfilled up to numerical fluctuations.

The remaining five dimensional solution space is parametrized by $\delta\lambda_i \equiv t_i \in \mathbb{R}$ with $i \in \{2, 3, 6, 7, 8\}$. Three CTs $\delta\lambda_2$, $\delta\lambda_6$ and $\delta\lambda_8$, which only appear in terms with no Φ_1 , are fully decoupled from the remaining CTs. The other free CT parameters $\delta\lambda_3$ and $\delta\lambda_7$ contribute to the other CTs δm_{22}^2 and δm_S^2 . The solution space for all CTs is given by

$$\delta m_{11}^2 = \frac{1}{2}H_{\zeta_1\zeta_1}^{\text{CW}} - \frac{3}{2}H_{\rho_1\rho_1}^{\text{CW}}, \quad (4.24a)$$

$$\delta m_{22}^2 = -H_{\rho_2\rho_2}^{\text{CW}} - \frac{1}{2}t_3v_1^2, \quad (4.24b)$$

$$\delta m_S^2 = -H_{\zeta_S\zeta_S}^{\text{CW}} - \frac{1}{2}t_7v_1^2, \quad (4.24c)$$

$$\delta \text{Re}(A) = -\frac{1}{v_1}H_{\zeta_2\zeta_S}^{\text{CW}}, \quad (4.24d)$$

$$\delta \text{Im}(A) = \frac{1}{v_1}H_{\Psi_2\zeta_S}^{\text{CW}}, \quad (4.24e)$$

$$\delta\lambda_1 = \frac{1}{v_1^2} \left(-H_{\zeta_1\zeta_1}^{\text{CW}} + H_{\rho_1\rho_1}^{\text{CW}} \right), \quad (4.24f)$$

$$\delta\lambda_2 = t_2, \quad (4.24g)$$

$$\delta\lambda_3 = t_3, \quad (4.24h)$$

$$\delta\lambda_4 = \frac{1}{v_1^2} \left(2H_{\rho_2\rho_2}^{\text{CW}} - H_{\zeta_2\zeta_2}^{\text{CW}} - H_{\Psi_2\Psi_2}^{\text{CW}} \right), \quad (4.24i)$$

$$\delta\lambda_5 = \frac{1}{v_1^2} \left(-H_{\zeta_2\zeta_2}^{\text{CW}} + H_{\Psi_2\Psi_2}^{\text{CW}} \right), \quad (4.24j)$$

$$\delta\lambda_6 = t_6, \quad (4.24k)$$

$$\delta\lambda_7 = t_7, \quad (4.24l)$$

$$\delta\lambda_8 = t_8, \quad (4.24m)$$

$$\delta T_{\text{CB}} = -N_{\rho_2}^{\text{CW}}, \quad (4.24n)$$

$$\delta T_1 = v_1 H_{\rho_1\rho_1}^{\text{CW}} - N_{\zeta_1}^{\text{CW}}, \quad (4.24o)$$

$$\delta T_2 = -N_{\zeta_2}^{\text{CW}}, \quad (4.24p)$$

$$\delta T_{\text{CP}} = -N_{\Psi_2}^{\text{CW}}, \quad (4.24q)$$

$$\delta T_S = -N_{\zeta_S}^{\text{CW}}. \quad (4.24r)$$

The first and second derivatives of V_{CW} in terms of scalar fields in their gauge basis are derived in [54] using the general tensor notation that is introduced in Sec. 4.1. The derivatives are implemented in BSMPT [65, 66]. Choosing the renormalization scheme with $t_i = 0$, $i \in \{2, 3, 6, 7, 8\}$, simplifies Eq. (4.24) to

$$\delta m_{11}^2 = \frac{1}{2}H_{\zeta_1\zeta_1}^{\text{CW}} - \frac{3}{2}H_{\rho_1\rho_1}^{\text{CW}}, \quad (4.25a)$$

$$\delta m_{22}^2 = -H_{\rho_2\rho_2}^{\text{CW}}, \quad (4.25b)$$

$$\delta m_S^2 = -H_{\zeta_S \zeta_S}^{\text{CW}}, \quad (4.25\text{c})$$

$$\delta \text{Re}(A) = -\frac{1}{v_1} H_{\zeta_2 \zeta_S}^{\text{CW}}, \quad (4.25\text{d})$$

$$\delta \text{Im}(A) = \frac{1}{v_1} H_{\Psi_2 \zeta_S}^{\text{CW}}, \quad (4.25\text{e})$$

$$\delta \lambda_1 = \frac{1}{v_1^2} \left(-H_{\zeta_1 \zeta_1}^{\text{CW}} + H_{\rho_1 \rho_1}^{\text{CW}} \right), \quad (4.25\text{f})$$

$$\delta \lambda_2 = 0, \quad (4.25\text{g})$$

$$\delta \lambda_3 = 0, \quad (4.25\text{h})$$

$$\delta \lambda_4 = \frac{1}{v_1^2} \left(2H_{\rho_2 \rho_2}^{\text{CW}} - H_{\zeta_2 \zeta_2}^{\text{CW}} - H_{\Psi_2 \Psi_2}^{\text{CW}} \right), \quad (4.25\text{i})$$

$$\delta \lambda_5 = \frac{1}{v_1^2} \left(-H_{\zeta_2 \zeta_2}^{\text{CW}} + H_{\Psi_2 \Psi_2}^{\text{CW}} \right), \quad (4.25\text{j})$$

$$\delta \lambda_6 = 0, \quad (4.25\text{k})$$

$$\delta \lambda_7 = 0, \quad (4.25\text{l})$$

$$\delta \lambda_8 = 0, \quad (4.25\text{m})$$

$$\delta T_{\text{CB}} = -N_{\rho_2}^{\text{CW}}, \quad (4.25\text{n})$$

$$\delta T_1 = v_1 H_{\rho_1 \rho_1}^{\text{CW}} - N_{\zeta_1}^{\text{CW}}, \quad (4.25\text{o})$$

$$\delta T_2 = -N_{\zeta_2}^{\text{CW}}, \quad (4.25\text{p})$$

$$\delta T_{\text{CP}} = -N_{\Psi_2}^{\text{CW}}, \quad (4.25\text{q})$$

$$\delta T_S = -N_{\zeta_S}^{\text{CW}}. \quad (4.25\text{r})$$

4.3.2. Modified Mass Scheme for CP in the Dark

Imposing the renormalization conditions of Eq. (4.21) on the CT potential of Eq. (4.17) is not sufficient in order to constrain the NLO masses exactly at their LO values. We still observe

$$\partial_{\zeta_2} \partial_{\Psi_2} (V_{\text{CW}} + V_{\text{CT}}) \sim \mathcal{O}(10^1) \quad (4.26)$$

after V_{CT} is determined through Eq. (4.24). The reason is non-zero $\partial_{ij}^2 V_{\text{CW}}$ for field directions in which $\partial_{ij}^2 V_{\text{CT}} = 0$.⁴ The NLO scalar masses are observed to show relative deviations from their tree-level values of the order of 0.005%.

CP in the Dark features CPV interactions that are not present at tree level but can be induced through 1-loop effects, see for example Fig. 4.1. Therefore, the introduction of CTs for all tree-level parameters as in Eq. (4.15) is not sufficient to capture all loop-induced CPV effects. The *conventional* mass scheme will fail for models like CP in the Dark that include CPV. In practice, this means that in order to actually fix all masses at their LO values, we need to introduce additional independent CTs that can absorb all non-vanishing second derivatives of the Coleman-Weinberg potential.

For CP in the Dark, we propose a *modified* mass scheme that fulfills Eq. (4.21) and is therefore able to capture all effects up to the order of the second derivative. In this scheme the additional CPV structure is parametrized by a new CT $\delta \text{Im}(\lambda_5)$, which is introduced

⁴The CTs of Eq. (4.24) are only a unique solution of Eq. (4.21) if Eq. (4.23) is fulfilled *and* additionally $\partial_i V_{\text{CT}} = 0 \Leftrightarrow \partial_i V_{\text{CW}} = 0$ and $\partial_{ij} V_{\text{CT}} = 0 \Leftrightarrow \partial_{ij} V_{\text{CW}} = 0$ for all $i, j \in \{1, \dots, N_0\}$. If, however, we find $\partial_i V_{\text{CW}} \neq 0$ for $\partial_i V_{\text{CT}} = 0$ or $\partial_{ij} V_{\text{CW}} \neq 0$ for $\partial_{ij} V_{\text{CT}} = 0$, then the solution is insufficient in the first place.

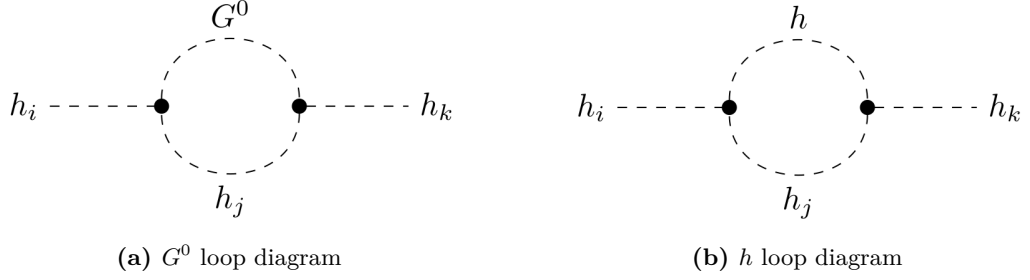


Figure 4.1.: One-loop diagrams contributing to the CP -violating $\zeta_2\Psi_2$ coupling, $i, j, k \in \{1, 2, 3\}$.

in the CT potential as

$$V'_{\text{CT}} \equiv V_{\text{CT}} + \frac{i}{2} \delta\text{Im}(\lambda_5) \left((\Phi_1^\dagger \Phi_2)^2 - (\Phi_1 \Phi_2^\dagger)^2 \right). \quad (4.27)$$

Although λ_5 is chosen to be real in the tree-level potential as discussed in Chapter 3, CPV vertices stemming from the $\delta\text{Im}(\lambda_5)$ CT in Eq. (4.27) are induced at one-loop level.

The CT $\delta\text{Im}(\lambda_5)$ therefore has to be included due to the same reason why tadpole CTs need to be included. The tadpoles vanish exactly at tree level, $T = 0$, but at one-loop level they may obtain non-zero contributions. Tadpole CTs δT are able to absorb the NLO tadpole contributions that would otherwise shift the tree-level VEV.

Again requiring the renormalization conditions of Eq. (4.21) determines $\delta\text{Im}(\lambda_5)$,

$$\delta\text{Im}(\lambda_5) = \frac{2}{v_1^2} H_{\zeta_2\Psi_2}^{\text{CW}}. \quad (4.28)$$

Together with Eq. (4.24) and the identities in Eq. (4.23), Eq. (4.28) represents a unique and complete solution for the renormalization scheme conditions in Eq. (4.15). All NLO scalar mixing angles and masses are exactly shifted to their LO values and can now be efficiently used as input for the parameter scan.

4.3.3. Constraining the t Parameters

The OS-shell like renormalization scheme that is defined in Sec. 4.3.2 fixes the NLO mixing angles and NLO masses exactly at their tree-level values. However, due to the vacuum of the model with a VEV only being assigned to the SM-like first doublet, there are five quartic CTs that are not constrained through the conditions of Eq. (4.21).

The CTs $\delta\lambda_3 = t_3$ (4.24h) and $\delta\lambda_7 = t_7$ (4.24l) are accessible through trilinear couplings, while $\delta\lambda_2 = t_2$ (4.24g), $\delta\lambda_6 = t_6$ (4.24k) and $\delta\lambda_8 = t_8$ (4.24m) are only accessible through quartic couplings, as they multiply quartic couplings of solely dark fields.

In order to fix all t_i parameters in the usual scheme we could in principle additionally constrain the third derivatives of the one-loop potential to be equal to those of the tree-level potential,

$$\partial_{\phi_i} \partial_{\phi_j} \partial_{\phi_k} V^{(0)} \Big|_{\phi=\langle\phi^c\rangle|_{T=0 \text{ GeV}}} \equiv \partial_{\phi_i} \partial_{\phi_j} \partial_{\phi_k} V(T=0 \text{ GeV}) \Big|_{\phi=\langle\phi^c\rangle|_{T=0 \text{ GeV}}} \quad (4.29a)$$

$$\Rightarrow \partial_{\phi_i} \partial_{\phi_j} \partial_{\phi_k} (V_{\text{CT}} + V_{\text{CW}}) \Big|_{\phi=\langle\phi^c\rangle|_{T=0 \text{ GeV}}} = 0, \quad (4.29b)$$

and equally the fourth derivatives of the one-loop potential to be equal to those of the tree-level potential,

$$\partial_{\phi_i} \partial_{\phi_j} \partial_{\phi_k} \partial_{\phi_l} V^{(0)} \Big|_{\phi=\langle\phi^c\rangle|_{T=0 \text{ GeV}}} \equiv \partial_{\phi_i} \partial_{\phi_j} \partial_{\phi_k} \partial_{\phi_l} V(T=0 \text{ GeV}) \Big|_{\phi=\langle\phi^c\rangle|_{T=0 \text{ GeV}}} \quad (4.30a)$$

$$\Rightarrow \partial_{\phi_i} \partial_{\phi_j} \partial_{\phi_k} \partial_{\phi_l} (V_{\text{CT}} + V_{\text{CW}}) \Big|_{\phi=\langle\phi^c\rangle|_{T=0 \text{ GeV}}} = 0. \quad (4.30b)$$

This would yield the CT potential in terms of derivatives of the Coleman-Weinberg potential. In the context of this thesis, also the fourth derivative of the Coleman-Weinberg potential was implemented in BSMPT, basic considerations can be found in App. A.

Demanding the additional renormalization scheme conditions of Eqs. (4.29) and (4.30) would exactly determine the t_i parameters in terms of the third derivatives $\partial_{\phi_i \phi_j \phi_k} V_{\text{CW}} \equiv T_{\phi_i \phi_j \phi_k}^{\text{CW}}$ and fourth derivatives $\partial_{\phi_i} \partial_{\phi_j} \partial_{\phi_k} \partial_{\phi_l} V_{\text{CW}} \equiv F_{\phi_i \phi_j \phi_k \phi_l}^{\text{CW}}$ of the Coleman-Weinberg potential, e.g.

$$t_3 = -\frac{1}{v_1} T_{\rho_2 \rho_2 \zeta_1}^{\text{CW}}, \quad t_7 = -\frac{1}{v_1} T_{\zeta_1 \zeta_S \zeta_S}^{\text{CW}}, \quad (4.31a)$$

$$t_2 = \frac{1}{3} F_{\rho_2 \rho_2 \rho_2 \rho_2}^{\text{CW}}, \quad t_6 = -\frac{1}{6} F_{\zeta_S \zeta_S \zeta_S \zeta_S}^{\text{CW}}, \quad t_8 = -F_{\rho_2 \rho_2 \zeta_S \zeta_S}^{\text{CW}}. \quad (4.31b)$$

However, as we will show in the following, this method leads to potential inconsistencies for trilinear and quartic CTs that were already constrained through mass renormalization.

The mass renormalization of Eq. (4.21b)

$$\partial_{\phi_i} \partial_{\phi_j} V^{(0)} \Big|_{\phi=\langle\phi^c\rangle|_{T=0 \text{ GeV}}} \equiv \partial_{\phi_i} \partial_{\phi_j} V(T=0 \text{ GeV}) \Big|_{\phi=\langle\phi^c\rangle|_{T=0 \text{ GeV}}} \quad (4.32a)$$

$$= \partial_{\phi_i} \partial_{\phi_j} (V^{(0)} + V_{\text{CW}} + V_{\text{CT}}) \Big|_{\phi=\langle\phi^c\rangle|_{T=0 \text{ GeV}}} \quad (4.32b)$$

already constrains the trilinear and quartic CTs $\delta \text{Re}(A)$, $\delta \text{Im}(A)$, $\delta \lambda_1$, $\delta \lambda_4$ and $\delta \lambda_5$ in terms of second derivatives of the Coleman-Weinberg potential as

$$\delta \text{Re}(A) = -\frac{1}{v_1} H_{\zeta_2 \zeta_S}^{\text{CW}}, \quad (4.33a)$$

$$\delta \text{Im}(A) = \frac{1}{v_1} H_{\Psi_2 \zeta_S}^{\text{CW}}, \quad (4.33b)$$

$$\delta \lambda_1 = \frac{1}{v_1^2} \left(-H_{\zeta_1 \zeta_1}^{\text{CW}} + H_{\rho_1 \rho_1}^{\text{CW}} \right), \quad (4.33c)$$

$$\delta \lambda_4 = \frac{1}{v_1^2} \left(2H_{\rho_2 \rho_2}^{\text{CW}} - H_{\zeta_2 \zeta_2}^{\text{CW}} - H_{\Psi_2 \Psi_2}^{\text{CW}} \right), \quad (4.33d)$$

$$\delta \lambda_5 = \frac{1}{v_1^2} \left(-H_{\zeta_2 \zeta_2}^{\text{CW}} + H_{\Psi_2 \Psi_2}^{\text{CW}} \right). \quad (4.33e)$$

If we would now additionally require the conditions of Eq. (4.29), or even (4.30), we would introduce additional in general non-zero contributions that potentially also violate the tree-level relations between masses and trilinear or quartic couplings, as elaborated in the following. This would then require an iterative procedure in order to determine the trilinear and quartic parameters.

In case of $\delta \text{Re}(A)$ constraining the trilinear couplings with Eq. (4.29) results in the following

condition

$$\partial_{\zeta_1 \zeta_2 \zeta_S}^3 V(T = 0 \text{ GeV})|_{\phi=\langle\phi^c\rangle|_{T=0 \text{ GeV}}} = \text{Re}(A) + \partial_{\zeta_1 \zeta_2 \zeta_S}^3 V_{\text{CW}}|_{\phi=\langle\phi^c\rangle|_{T=0 \text{ GeV}}} + \delta\text{Re}(A) \quad (4.34a)$$

$$\equiv \partial_{\zeta_1 \zeta_2 \zeta_S}^3 V^{(0)}|_{\phi=\langle\phi^c\rangle|_{T=0 \text{ GeV}}} = \text{Re}(A), \quad (4.34b)$$

while $\delta\text{Re}(A)$ is already defined to absorb exactly the contribution arising from $\partial^2 V_{\text{CW}}$ in mass renormalization, cf. Eq. (4.33a), so that

$$\partial_{\zeta_1 \zeta_2 \zeta_S}^3 V(T = 0 \text{ GeV})|_{\phi=\langle\phi^c\rangle|_{T=0 \text{ GeV}}} = \text{Re}(A) + \underbrace{\partial_{\zeta_1 \zeta_2 \zeta_S}^3 V_{\text{CW}}|_{\phi=\langle\phi^c\rangle|_{T=0 \text{ GeV}}}}_{\neq 0, \text{ in general}} - \frac{1}{v_1} H_{\zeta_2 \zeta_S}^{\text{CW}}. \quad (4.35)$$

If by chance the contribution from the additional third derivative of V_{CW} turns out to be equal to the H^{CW} term and is therefore exactly canceled by $\delta\text{Re}(A)$, our renormalization condition in Eq. (4.34) would be fulfilled. In general, this is *not* the case. The corresponding trilinear coupling gets modified by a non-zero one-loop contribution

$$\lambda_{\zeta_1 \zeta_2 \zeta_S} = \lambda_{\zeta_1 \zeta_2 \zeta_S}^{(0)} + \underbrace{\Delta\lambda_{\zeta_1 \zeta_2 \zeta_S}^{(1)}}_{\neq 0, \text{ in general}}. \quad (4.36)$$

In order to renormalize the additional one-loop contribution to zero we need to modify the CT potential of Eq. (4.27) to

$$V_{\text{CT}}'' \equiv V_{\text{CT}}' + \delta\widehat{\text{Re}}(A) \left[\Phi_1^\dagger \Phi_2 \Phi_S + \Phi_S \Phi_2^\dagger \Phi_1 \right] \quad (4.37)$$

by introducing a new CT of the form

$$\delta\widehat{\text{Re}}(A) \equiv -\delta\text{Re}(A) - \partial_{\zeta_1 \zeta_2 \zeta_S}^3 V_{\text{CW}}|_{\phi=\langle\phi^c\rangle|_{T=0 \text{ GeV}}} \quad (4.38a)$$

$$= \frac{1}{v_1} H_{\zeta_2 \zeta_S}^{\text{CW}} - \partial_{\zeta_1 \zeta_2 \zeta_S}^3 V_{\text{CW}}|_{\phi=\langle\phi^c\rangle|_{T=0 \text{ GeV}}}. \quad (4.38b)$$

Then the NLO trilinear couplings are fixed at their LO values by construction

$$\partial_{\zeta_1 \zeta_2 \zeta_S}^3 V(T = 0 \text{ GeV})|_{\phi=\langle\phi^c\rangle|_{T=0 \text{ GeV}}} = \text{Re}(A) + \underbrace{\partial_{\zeta_1 \zeta_2 \zeta_S}^3 V_{\text{CW}}|_{\phi=\langle\phi^c\rangle|_{T=0 \text{ GeV}}}}_{=0} + \delta\text{Re}(A) + \delta\widehat{\text{Re}}(A) \quad (4.39a)$$

$$= \partial_{\zeta_1 \zeta_2 \zeta_S}^3 V^{(0)}|_{\phi=\langle\phi^c\rangle|_{T=0 \text{ GeV}}}. \quad (4.39b)$$

But the non-zero one-loop contributions of Eq. (4.36) modify the relation between exact trilinear couplings and their values in the mass renormalization scheme. In order to again ensure mass renormalization one has to introduce new additional CTs that absorb the induced shift from $\delta\widehat{\text{Re}}(A)$. Following this approach, one can consequently define quadratic, trilinear and quartic CTs in an *iterative* approach by introducing a set of new CTs that can order by order in iteration absorb the mismatch until the required level of precision is acquired.

Another possible and consistent way is to determine the t_i parameters through future experiments. Thus, t_3 and t_7 can be extracted from Higgs-to-Higgs decays. The quartic couplings influenced by t_2 , t_6 and t_8 could be derived from Higgs-to-Higgs scattering.

The following Sec. 4.3.4 discusses the effects of changing the t_i parameters. In the end we will argue to set $t_i = 0$ for the analysis in Chapter 5.

4.3.4. Changing the t Parameters

A change of the t_i parameters, $i \in \{2, 3, 6, 7, 8\}$, corresponds to a change in the renormalization scheme. The choice of t_i is unphysical and should therefore not change the result. However, as discussed in [72–74] a proper parameter conversion is essential in order to compare results obtained for different renormalization schemes.

Take two different renormalization schemes RS_1 with $t_i \equiv t_1$ and RS_2 with $t_i \equiv t_2$. The bare parameter $p^{(0)}$ is the same in both schemes

$$p^{(0)} = p_1 + \delta p_1 = p_2 + \delta p_2. \quad (4.40)$$

Now the renormalized parameters p_1 and p_2 of the two schemes are related through

$$p_2 = p_1 + \delta p_1 - \delta p_2. \quad (4.41)$$

Parameter-dependent quantities, e.g. amplitudes, can be converted as follows. Assume the quantity f is given in scheme RS_1 . The renormalized f at NLO can be written as

$$f^{(1)}(p_1 + \delta p_1) = f^{(1)}(p_1) + f^{(0)}(p_1 + \delta p_1) \quad (4.42a)$$

$$= f^{(1)}(p_1) + f^{(0)}(p_1) + \left. \frac{\partial f^{(0)}}{\partial p} \right|_{p=p_1} (p_1 + \delta p_1 - p_1) + \mathcal{O}(\delta p^2) \quad (4.42b)$$

$$= f^{(1)}(p_1) + f^{(0)}(p_1) + f'^{(0)}(p_1) \cdot \delta p_1 + \mathcal{O}(\delta p^2). \quad (4.42c)$$

Using Eq. (4.41), the same quantity f in scheme RS_2 reads

$$f^{(1)}(p_2 + \delta p_2) = f^{(1)}(p_2) + f^{(0)}(p_2) + f'^{(0)}(p_2) \cdot \delta p_2 \quad (4.43a)$$

$$= f^{(1)}(p_1 + \delta p_1 - \delta p_2) + f^{(0)}(p_1 + \delta p_1 - \delta p_2) + f'^{(0)}(p_1 + \delta p_1 - \delta p_2) \cdot \delta p_2 \quad (4.43b)$$

$$= f^{(1)}(p_1) + \left. \frac{\partial f^{(1)}}{\partial p} \right|_{p=p_1} (\delta p_1 - \delta p_2) + f^{(0)}(p_1) + \left. \frac{\partial f^{(0)}}{\partial p} \right|_{p=p_1} (\delta p_1 - \delta p_2) \quad (4.43c)$$

$$+ f'^{(0)}(p_1) \delta p_2 + \left. \frac{\partial^2 f^{(0)}}{\partial p^2} \right|_{p=p_1} (\delta p_1 - \delta p_2) \delta p_2 + \mathcal{O}(\delta p^2)$$

$$= f^{(1)}(p_1) + f^{(0)}(p_1) + f'^{(0)}(p_1) (\delta p_1 - \delta p_2 + \delta p_2) + \mathcal{O}(\delta p^2) \quad (4.43d)$$

$$= f^{(1)}(p_1) + f^{(0)}(p_1) + f'^{(0)}(p_1) \cdot \delta p_1 + \mathcal{O}(\delta p^2). \quad (4.43e)$$

Comparing the quantity f expressed in scheme RS_1 , Eq. (4.42), and RS_2 , Eq. (4.43), we find that if the parameters are consistently converted between the renormalization schemes, then the quantities f will be equal up to one-loop order modulo higher order corrections.

$$f^{(1)}(p_2 + \delta p_2) = f^{(1)}(p_1 + \delta p_1) + \mathcal{O}(\delta p^2). \quad (4.44)$$

The one-loop corrected effective potential at finite temperature is, however, not an analytical function in terms of its renormalized parameters in the proposed incomplete OS scheme of Sec. 4.3.2. It is therefore not possible to do the conversion of renormalized parameters between different t_i -schemes consistently, which would ensure the conservation

of all parameter-dependent quantities.

We find that changing t_i without the necessary parameter conversion leads to unphysical effects that impose a limit on the range of allowed t_i . This is because a change in t_i without a proper parameter conversion influences the shape of the potential. From now on we define

$$t_{37} \equiv t_3 = t_7, \quad (4.45a)$$

$$t_{268} \equiv t_2 = t_6 = t_8. \quad (4.45b)$$

We observe that the CT potential is highly sensitive for large t_{37} . In order to illustrate the effect of a change in t_{37} on the potential, we consider ΔV_{eff} defined as the relative difference between the one-loop corrected effective potential at the electroweak tree-level minimum ϕ , written in the gauge basis of Eq. (3.9) as

$$\phi \equiv \{0, 0, 0, 0, v_1, 0, 0, 0, 0\} \quad \text{with} \quad v_1 \equiv v = 246.22 \text{ GeV}, \quad (4.46)$$

and at the found global minimum $\phi + \delta\phi$ at zero temperature

$$|\Delta V_{\text{eff}}| = \left| \frac{V_{\text{eff}}^{(1)}(\phi, T = 0 \text{ GeV}) - V_{\text{eff}}^{(1)}(\phi + \delta\phi, T = 0 \text{ GeV})}{V_{\text{eff}}^{(1)}(\phi, T = 0 \text{ GeV})} \right|. \quad (4.47)$$

If $|\Delta V_{\text{eff}}| = 0$, the found global minimum of the one-loop corrected effective potential is identical with the tree-level electroweak minimum as long as $\delta\phi = 0$. In case $\delta\phi \neq 0$, both minima are degenerate.

The dependence of $|\Delta V_{\text{eff}}|$ and $\delta\phi$ on $t_{37} \in \{-20, \dots, 20\}$ due to no proper parameter conversion is shown in Fig. 4.2 for six parameter points that are found to have an SFOEWPT for $t_i = 0$. These benchmark points are listed in App. B. Points where $\delta\phi = 0$ and therefore the electroweak minimum is found as the global minimum at $T = 0 \text{ GeV}$, are highlighted in yellow. We find that large $|t_{37}|$ lead to $\delta\phi \gg 0$ and $|\Delta V_{\text{eff}}| \gg 0$. Then the found global minimum for $T = 0 \text{ GeV}$ no longer coincides with the electroweak minimum. $|t_{37}| \gg 0$ results in the development of new *unphysical* global minima if no proper scheme conversion is performed.⁵

Figure 4.3 illustrates the temperature dependence of the one-loop global minimum $v(T)$ (red), see Eq. (5.4), and all five individual finite-temperature VEV directions ω_1 , ω_2 , ω_{CP} , ω_{CB} and ω_S due to no proper renormalization scheme conversion for different choices of $t_{37} \in \{0, 13, 20\}$ for the parameter point F13R406, see App. B. In case $t_{37} = 0$ an SFOEWPT with $\xi_c = 1.05316$, $v_c = 158.765 \text{ GeV}$ and $T_c = 150.751 \text{ GeV}$ is observed. Only ω_1 shows a phase transition. The broken EW VEV is found as the global VEV at $T = 0 \text{ GeV}$. If we set $t_{37} = 13$ and $t_{37} = 20$ without performing a proper renormalization scheme conversion the parameter point will fail the consistency checks performed by BSMPT, see Sec. 5.1.2. While for $t_{37} = 13$ at $T = 0 \text{ GeV}$ the symmetric phase is the global minimum, a non-symmetric phase is found to evolve around $T = 230 \text{ GeV}$. For $t_{37} = 20$ this unphysical broken phase is found to be the new global minimum over the whole temperature range. Consequently,

⁵The effect of changing t_{37} is much larger than the effect of changing t_{268} . Quantitatively, if only t_{268} is varied the same V_{CT} potential value is observed if approximately $t_{268} \sim -2 \times 10^4 \cdot t_{37}$. Only negative t_{268} were observed to show a similar behavior to what was observed for negative t_{37} in Fig. 4.2. t_{37} influence δm_{22}^2 and δm_{ξ}^2 which are of the order $\mathcal{O}(10^3 - 10^4) \text{ GeV}^2$ and therefore up to three orders of magnitude larger than the other CTs.

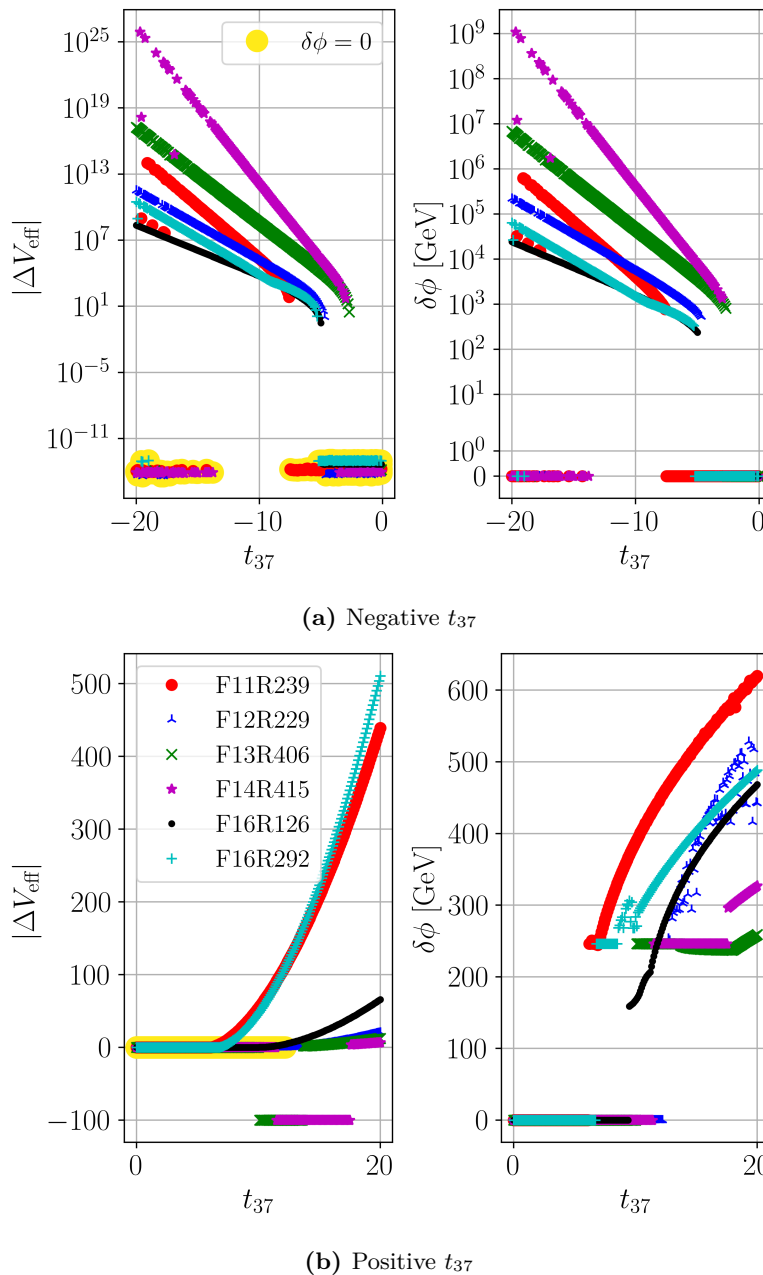


Figure 4.2.: The absolute relative difference $|\Delta V_{\text{eff}}|$, defined in Eq. (4.47), between the one-loop corrected effective potential for $T = 0 \text{ GeV}$ at the electroweak tree-level minimum ϕ and at the found global minimum $\phi + \delta\phi$ as well as the deviation from the electroweak tree-level minimum $\delta\phi$ as a function of t_{37} for negative t_{37} (Fig. 4.2a) and positive t_{37} (Fig. 4.2b) and for six benchmark points that have an SFOEWPT at $t_i = 0$. The six benchmark points are defined in App. B. Figures 4.2a and 4.2b share the same color code. In case $V_{\text{eff}}^{(1)}(\phi) + 100 \text{ GeV} < V_{\text{eff}}^{(1)}(\phi + \delta\phi)$ we set $|\Delta V_{\text{eff}}| = -100$. As long as $\delta\phi = 0$, the electroweak minimum is found as the global minimum at $T = 0 \text{ GeV}$. These points are highlighted in yellow.

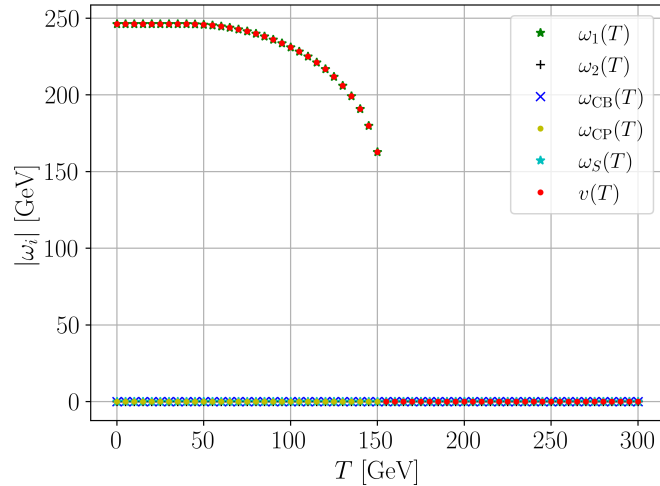
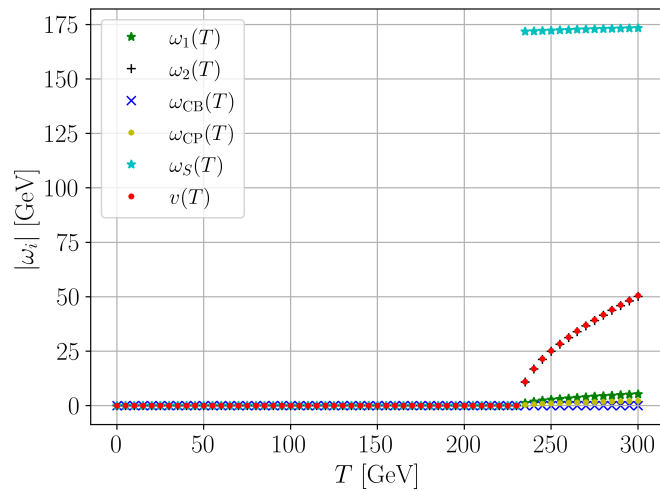
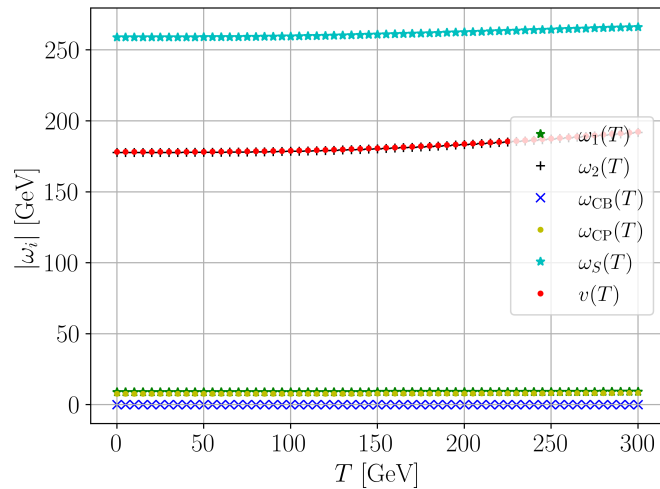
(a) $t_{37} = 0$ (b) $t_{37} = 13$ (c) $t_{37} = 20$

Figure 4.3.: Evolution of the VEV $v(T)$ at the one-loop global minimum (red), as defined in Eq. (5.4), and the individual VEV contributions ω_1 (green stars), ω_2 (black plus signs), ω_{CB} (dark blue crosses), ω_{CP} (yellow dots) and ω_S (light blue stars) as a function of the temperature T for the point F13R406 and for $t_{37} = 0$ (Fig. 4.3a), $t_{37} = 13$ (Fig. 4.3b) and $t_{37} = 20$ (Fig. 4.3c). The parameter point F13R406 is given in App. B.

a large non-zero t_{37} influences the shape of the one-loop corrected effective potential. New t_i -dependent local minima emerge and become unphysical global minima. They spoil the one-loop behavior of the effective potential at finite temperature and limit the allowed t_i range for a valid renormalization scheme in case no proper scheme conversion is performed.

Figures 4.4 and 4.5 show the one-loop corrected effective potential at zero temperature as a function of the scalar fields in direction of Φ_1 (blue), Φ_2 (yellow) and Φ_S (green) for different choices of t_i for the benchmark point F16R292 that is given in App. B. Boundedness from below is found to be always guaranteed for the whole one-loop corrected effective potential along each field direction. V_{CW} will compensate a V_{CT} that is not bounded from below. However, depending on the choice of t_i there are regions where $V^{(1)}$ develops t_i -dependent minima in direction of the dark fields if no proper scheme conversion is performed. Figure 4.4c shows such a new unphysical global minimum for $t_{268} = -20$ in direction of the second doublet fields. Choosing $t_{2,6} < 0$ leads to V_{CT} not being bounded from below. This choice of t_i violates the conditions stated in [16] for a general viable N2HDM. By comparing Fig 4.5a where $t_2 = -20$ and Fig 4.5b where $t_6 = -10^4$ while all other parameters are kept fixed, we observe $V^{(1)}$ to develop t_i dependent minima in direction of the dark doublet for $t_2 = -20$ and the dark singlet field for $t_6 = -10^4$. Note that $V^{(1)}$ will be bounded from below if large enough ϕ_i are considered, see Fig. 4.4.

Figure 4.6 illustrates the shape of the tree-level and the one-loop corrected effective potential at zero temperature near the origin in direction of ζ_1 (blue), ζ_2 (yellow) and ζ_S (green) for $t_i \in \{0, 10\}$ and $t_{268} = -1$ for the benchmark point F16R292, given in App. B. The Mexican-hat shaped potential with broken minimum at $\phi_i = 264.22$ GeV is observed in the ζ_1 -direction of the SM-like first doublet Φ_1 independent of the choice of t_i . However, choosing $|t_i| > 0$ leads to deviations from the EW minimum obtained from the one-loop effective potential at $T = 0$ GeV in direction of the dark doublet. *Any* deviation from the EW minimum at $T = 0$ GeV corresponds to *unphysical* global minima. For $t_i = 0$ (Fig. 4.6, middle row) the EW minimum is still the global minimum because the dark directions (i.e. the direction ζ_2 from the second doublet) are exactly in their symmetric configuration. For $t_i = 10$ (Fig. 4.6, upper row) the dark doublet directions, represented by $\phi_i = \zeta_2$, are observed to also develop a Mexican-hat shaped potential that leads to $v(T = 0 \text{ GeV}, t_i = 20) \neq v_{\text{EW}}(T = 0 \text{ GeV}, t_i = 0)$ and for $t_{268} = -1$ (Fig. 4.6, lower row) unphysical minima at even larger dark ϕ_i in direction of the dark doublet evolve. Note that the whole one-loop potential will still be bounded from below in every field directions, as illustrated in Fig. 4.4.

In conclusion, Figs. 4.4, 4.5 and 4.6 all show significant and t_i -dependent defects for large t_i . Then the found global minimum no longer coincides with the electroweak minimum at zero temperature as also indicated by the analysis of $|\Delta V_{\text{eff}}|$. This case, see Eq. (5.8), is caught by BSMP and the point will then fail the scan, nevertheless it clearly shows the limitations of choosing t_i when no proper scheme conversion is performed.

On the other hand, as already stated above, t_3 and t_7 influence the one-loop trilinear couplings. In particular, the trilinear couplings between the SM-like Higgs h and two dark scalars $h_1 h_1$, $h_2 h_2$, $h_3 h_3$, $H^\pm H^\pm$ are sensitive to a change in t_{37} . Raising t_{37} shifts the couplings to larger negative values for the same mass range. The maximal absolute coupling value is obtained for the largest dark scalar masses. Figure 4.7 shows the one-loop trilinear couplings $\lambda_{hh_1 h_1}^{(1)}$ obtained from the one-loop corrected effective potential at $T = 0$ GeV in the plane spanned by m_{H^\pm} and m_{h_1} for $t_i \in \{0, 2\pi, 4\pi\}$ and all found SFOEWPT

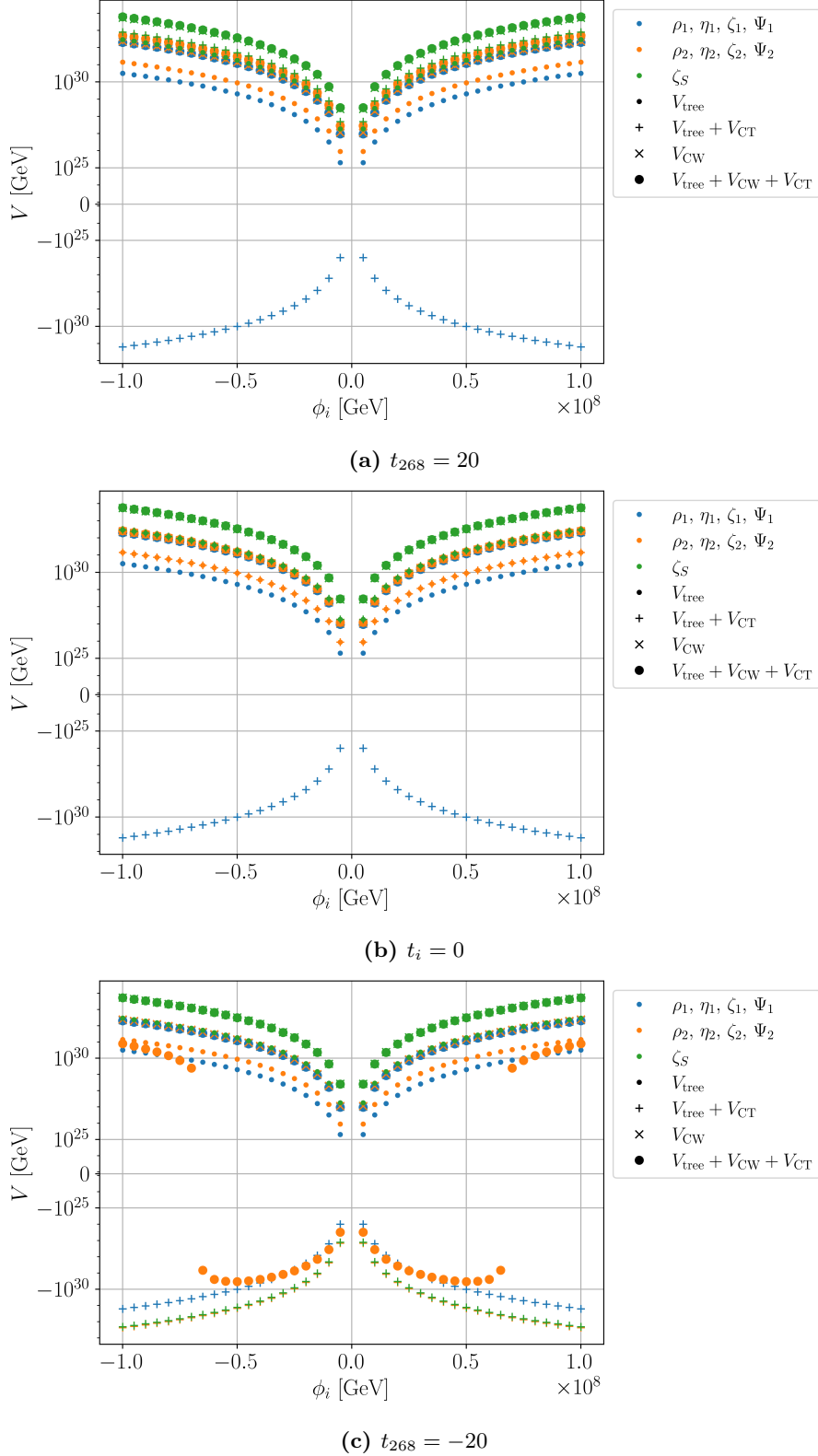
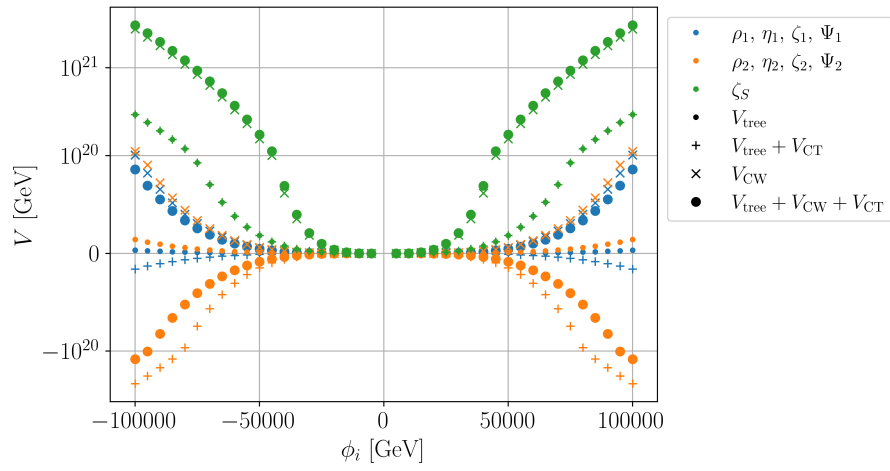
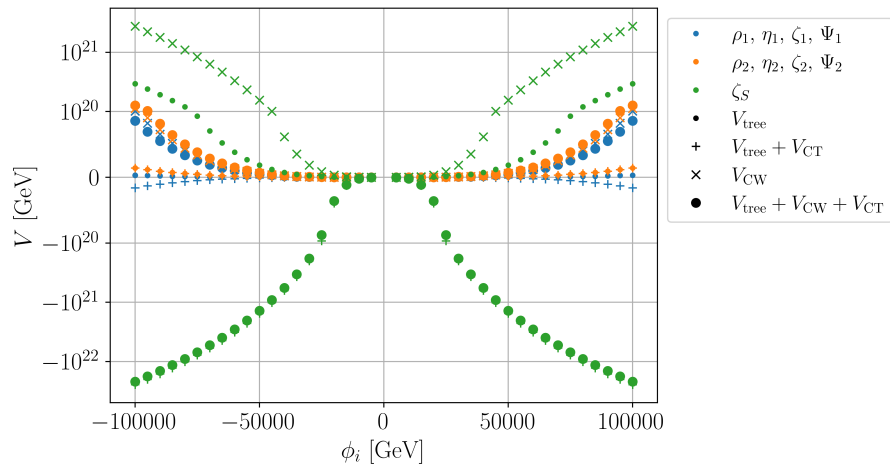


Figure 4.4.: Development of the tree-level potential V_{tree} (small dots), the sum of the tree-level and the CT potential $V_{\text{tree}} + V_{\text{CT}}$ (plus sign), the Coleman-Weinberg potential V_{CW} (cross) and the sum of tree-level, Coleman-Weinberg and CT potential (large dots) for different field directions, namely the Φ_1 -direction (blue), the Φ_2 -direction (orange) and the $\zeta_S = \Psi_S$ -direction (green) as a function of the field value ϕ_i for the point F16R292 that is given in App. B and $t_{268} = 20$ (Fig. 4.4a), $t_i = 0$ (Fig. 4.4b) and $t_{268} = -20$ (Fig. 4.4c). For the doublet directions Φ_i , with $i \in \{1, 2\}$, the field value ϕ_i is set to one of the four corresponding fields in the gauge basis $\{\rho_i, \eta_i, \zeta_i, \Psi_i\}$, while the other field directions are then set to zero, respectively, as the shape of V is independent of this choice.

(a) $t_2 = -20$ (b) $t_6 = -10^3$ **Figure 4.5.:** Same as Fig. 4.4, but for $t_2 = -20$ (Fig. 4.5a) and $t_6 = -10^3$ (Fig. 4.5b).

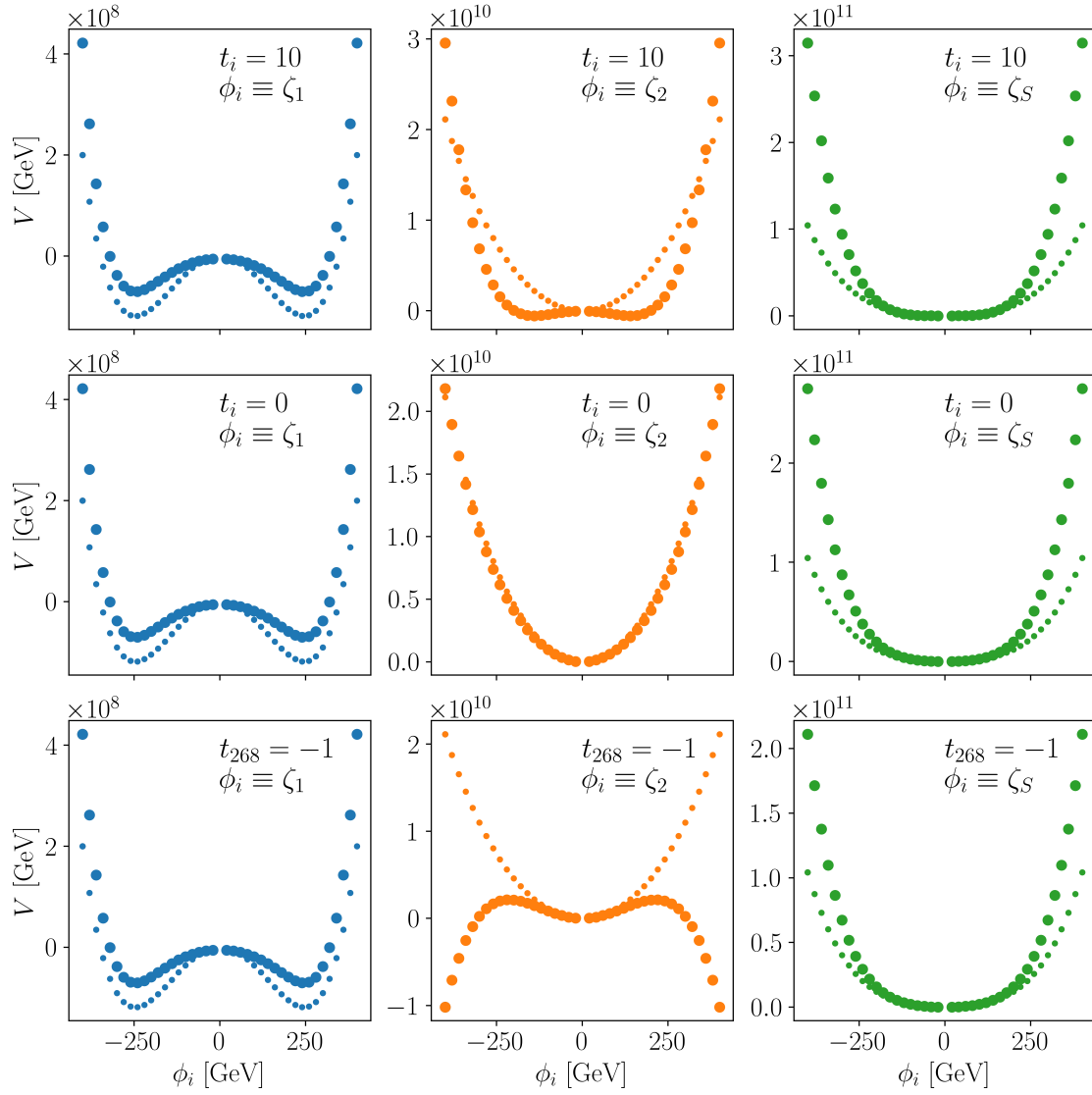


Figure 4.6.: Development of the tree-level potential (small dots) and complete one-loop potential (large dots) at $T = 0$ GeV for small field variations $|\phi_i| < 400$ GeV for the ζ_1 -direction (blue dots, left column), the ζ_2 -direction (orange dots, middle column) and the ζ_S -direction (green dots, right column) as a function of the field value ϕ_i for $t_i = 10$ (upper row), $t_i = 0$ (middle row) and $t_{268} = -1$ (lower row) for the point F16R292, given in App. B.

points that were obtained without applying DM constraints. In Fig. 4.8 we illustrate the SFOEWPT points in the same mass plane, but indicate the strength of the EWPT ξ_c , defined in Eq. (2.22), by the color code. We also show the sample that passes the theoretical and experimental constraints checked by **ScannerS** [75, 76] (gray), see Sec. 5.1.1 and the sample that additionally passes all checks by **BSMPT** [65, 66] (orange), see Sec. 5.1.2.⁶

Figures 4.7 and 4.8 show a change in phenomenology for higher t_i values. Higher dark scalar masses are needed in order to enable an SFOEWPT, while the trilinear couplings are shifted to lower values for the same mass range.

In order to still ensure NLO stability and perturbativity one could derive constraints on t_i from the size of the unconstrained trilinear couplings. However, as we do not use a complete OS-scheme and do not have an analytic formula for the one-loop effective corrected potential, the relation between one-loop trilinear coupling and input parameters in the t_i -scheme is unknown. In principle, knowing these relations would enable to translate the one-loop trilinear couplings in the $t_i = 0$ scheme to a scheme with arbitrary t_i . A proper translation would ensure that any difference between the renormalization schemes is only due to unknown higher-order corrections, but not connected to a change in t_i .

What we observe in Figs. 4.7 and 4.8 can again be understood as a relic of our lack of properly converting the parameters between the different schemes. In principle, if one could do a complete parameter conversion between the schemes, the mass parameter space is expected to be identical between different t_i choices modulo higher order corrections. Like in Eq. (4.41), we have for the trilinear couplings

$$\lambda_{3H}^{t_i=0} + \delta\lambda_{3H}^{t_i=0} = \lambda_{3H}^{t_i=2\pi} + \delta\lambda_{3H}^{t_i=2\pi} = \lambda_{3H}^{t_i=4\pi} + \delta\lambda_{3H}^{t_i=4\pi}, \quad (4.48)$$

which would in principle allow us to perform the parameter conversion. But the one-loop corrected effective potential at finite temperature in its notation of Sec. 4.1 is not an analytical function in terms of the trilinear couplings. If it was, one could insert the converted parameters and then extract the input parameters in the different scheme. Because we still show the same unconverted scan range for the input parameters $p^{t_i=0}$, but plot results for the changed renormalization scheme with $t_i \neq 0$, the result range is changed.

Let us repeat the argument. The observed change in phenomenology is not physical, but a remnant from not properly converting the renormalization scheme. Coming back to the analysis of $|\Delta V_{\text{eff}}|$ in Fig. 4.2, the shape of the potential is influenced through a change in t_i because even though we set $t_i \neq 0$ we still plot $V_{t_i=0}^{(1)}$ without a proper conversion to $V_{t_i \neq 0}^{(1)}$. The result is that for too large t_i our perturbative approach breaks down indicated by the evolution of new unphysical global minima, as also seen in Fig. 4.3. A proper conversion to the general t_i -scheme would, however, imply to minimize $V_{t_i}^{(1)}$, not $V_{t_i=0}^{(1)}$ when $t_i \neq 0$.

In the following discussion we set $t_i = 0$ and show results for this specific renormalization scheme. With choosing $t_i = 0$, no additional finite pieces that are irrelevant for the initial aim of fixing NLO masses and angles at their tree-level values are picked up. Then the CT potential is given by Eqs. (4.17), (4.25) and (4.27). All parameters and parameter-dependent quantities have to be understood as defined in the $t_i = 0$ scheme.

⁶The workflow of the parameter scan is described in detail in Sec. 5.1.

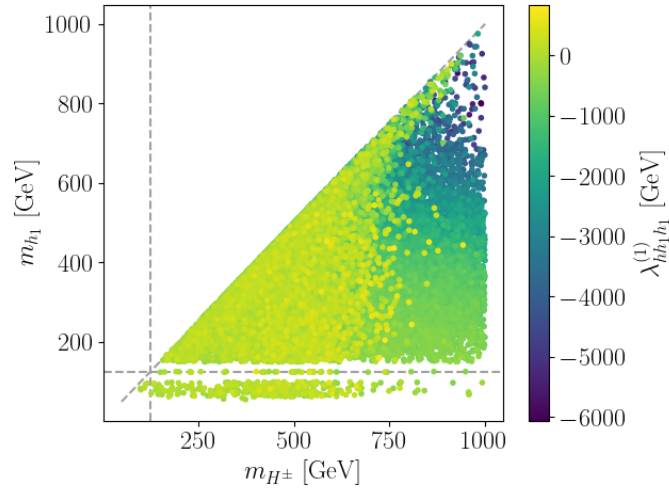
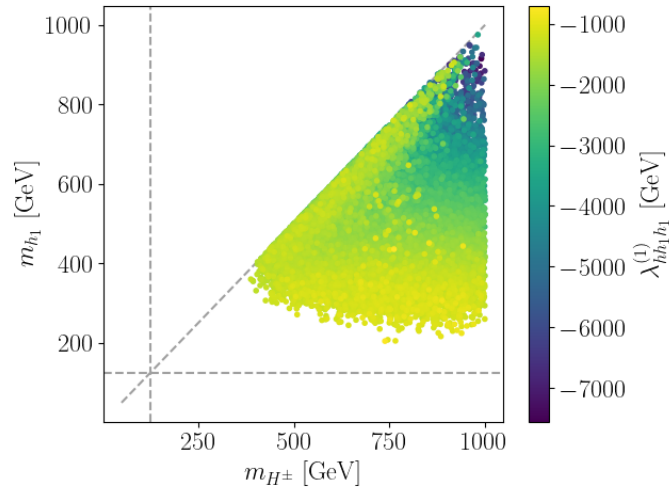
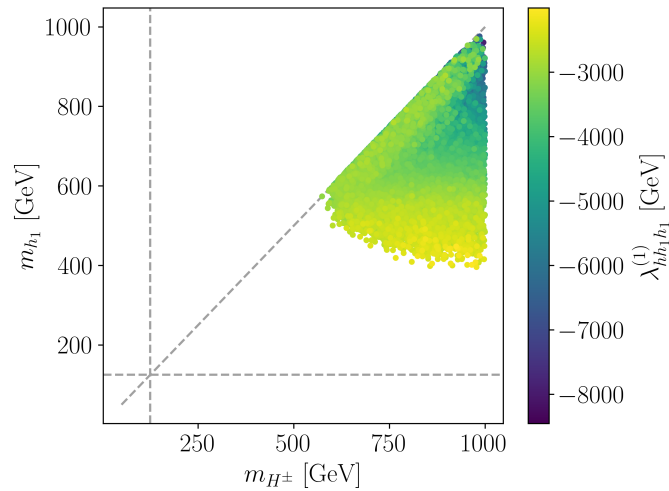
(a) $t_i = 0$ (b) $t_i = 2\pi$ (c) $t_i = 4\pi$

Figure 4.7.: The one-loop trilinear coupling hh_1h_1 in the $m_{H^\pm} - m_{h_1}$ -plane for $t_i = 0$ (Fig. 4.7a), $t_i = 2\pi$ (Fig. 4.7b) and $t_i = 4\pi$ (Fig. 4.7c). The size of the one-loop trilinear coupling $\lambda_{hh_1h_1}^{(1)}$ is indicated by color for all found viable SFOEWPT points. No DM constraints are imposed for this scan.

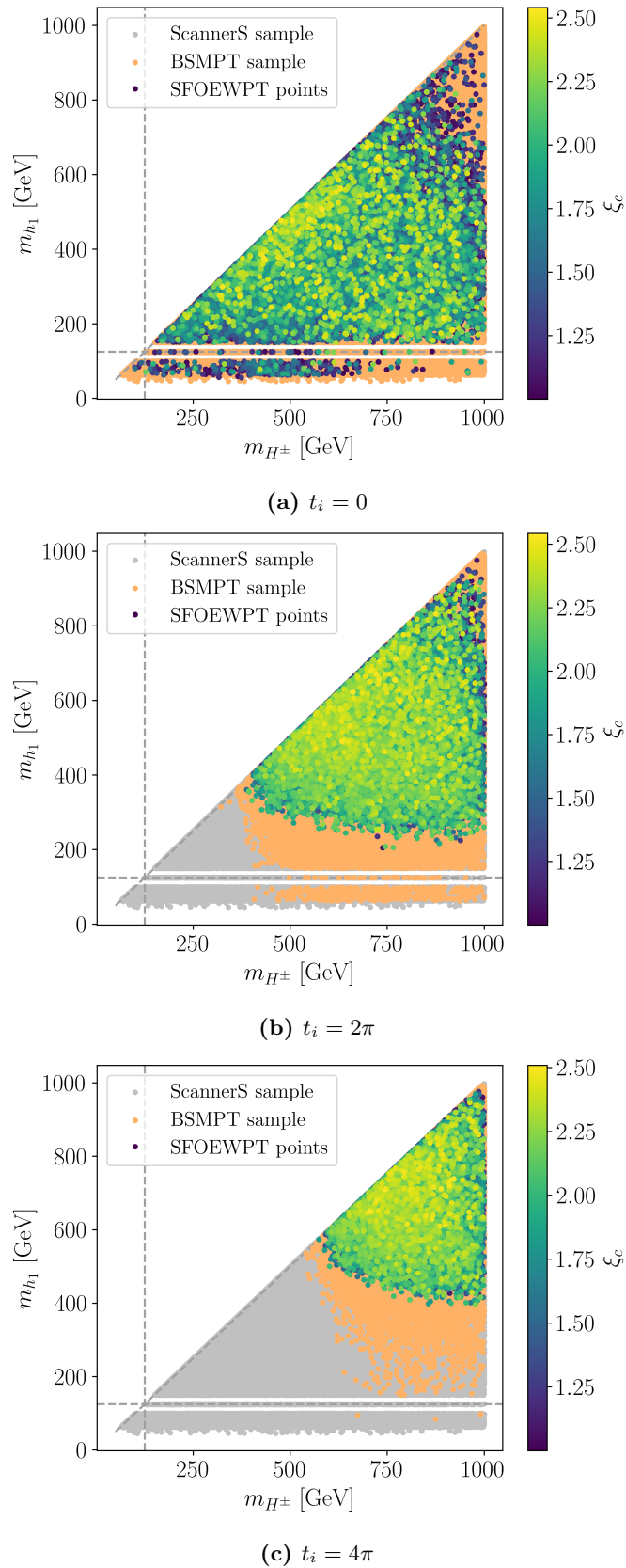


Figure 4.8.: Scatter plot in the $m_{H^\pm} - m_{h_1}$ -plane for all points passing the tests by ScannerS [75, 76] (gray), see Sec. 5.1.1, and points additionally passing the BSMPT [65, 66] checks (orange), see Sec. 5.1.2, for $t_i = 0$ (Fig. 4.8a), $t_i = 2\pi$ (Fig. 4.8b) and $t_i = 4\pi$ (Fig. 4.8c). Colored points are those for which BSMPT finds $\xi_c > 1$ with the size indicated by the color code. No DM constraints are imposed for this scan, $T_c > T_{EW}$ is additionally required, as discussed in Sec. 5.1.2.

5. Results

This Chapter presents the results that were obtained in the context of this thesis. The workflow of the numerical analysis is introduced in Sec. 5.1. We give an overview of the parameter point sample that we obtained for CP in the Dark in Sec. 5.2. Section 5.3 summarizes the VEV configurations that were found to show an SFOEWPT. The distribution of SFOEWPT points in the dark mass plane is illustrated in Sec. 5.4, pointing out the importance of applying DM constraints. Section 5.5 shows the singlet and doublet admixture of the SFOEWPT points. The sizes of the trilinear Higgs self-couplings of the SFOEWPT points are discussed in Sec. 5.6 and the predictions on DM observables in Sec. 5.7, respectively. Section 5.8 shows results for the branching ratios of the SM-like Higgs h into photons and dark particles.

5.1. Workflow

In order to investigate the possibility of an SFOEWPT in CP in the Dark and determine its available parameter space, we use the programs `BSMPT` [65, 66] and `ScannerS-2` [75, 76]. `ScannerS-2` scans a given parameter space and returns points which fulfill certain theoretical and experimental bounds. The procedure is further introduced in Sec. 5.1.1.

`BSMPT` is used to perform the global minimization of the one-loop corrected effective potential at finite temperature. It determines the strength of the phase transitions ξ_c using Eq. (2.22). Section 5.1.2 gives details on how `BSMPT` is used in the context of this thesis.

5.1.1. ScannerS

The code `ScannerS-2` [75, 76] performs parameter scans for SM extensions checking for experimental and theoretical constraints. `ScannerS-2` already provides an implementation of CP in the Dark following the conventions of [14]. The model is referred to as the minimal CP-violating DM model, shorthand CPVDM.

Every parameter point is checked for tree-level perturbative unitarity. Perturbative unitarity is crucial in order for the perturbative approximation to hold. `ScannerS` demands the tree-level $2 \rightarrow 2$ scattering matrix to fulfill

$$\left| \mathcal{M}_{2 \rightarrow 2}^i \right| \leq 8\pi. \quad (5.1)$$

A stable tree-level vacuum is further ensured by testing the tree-level potential for *boundedness from below*, namely requiring that the potential tends to positive infinity for large field values and does not grow towards large negative potential values. Both theoretical constraints can be taken over from the N2HDM [16].

	min.	max.
m_h	125.09	125.09
m_{h_1}	1	1000
m_{h_2}	1	1000
m_{H^\pm}	65	1000
α_1	$-\pi/2$	$\pi/2$
α_2	$-\pi/2$	$\pi/2$
α_3	$-\pi/2$	$\pi/2$
λ_2	0	9
λ_6	0	17
λ_8	-26	26
m_{22}^2	0	10^6
m_S^2	0	10^6

Table 5.1.: Input parameter ranges used for `ScannerS`, for details see Sec. 5.1.1. Masses are given in GeV.

The Peskin-Takeuchi electroweak precision constraints S , T and U [77] are tested via the fit of [78]. In its *default* working mode, `ScannerS` provides an automated link to the codes `HiggsBounds` [79–83] and `HiggsSignals` [84, 85]. This enables a check of experimental constraints from Tevatron, LEP and LHC for models with extended scalar sectors.

Most stringent constraints on extended scalar sectors with CPV originate additionally from the EDM of the electron [86],

$$|d_e| < 8.7 \times 10^{-29} \text{ ecm} . \quad (5.2)$$

However, in CP in the Dark, h is the only scalar that couples to fermions. Even though this model features explicit CPV, the EDM constraints are therefore automatically fulfilled [14].

The code `MicrOMEGAs` 5.2.7a [87–89] is included to impose DM constraints on the parameter space. The predicted relic density Ω^{model} is required to not exceed

$$\Omega^{\text{model}} h^2 \leq \Omega^{\text{obs}} h^2 + 2\delta , \quad (5.3)$$

with the uncertainty δ on the measurement and the experimentally observed relic density $\Omega^{\text{obs}} h^2 = 0.1200 \pm 0.0012$ [4]. Additionally, `ScannerS` is able to include constraints on the DM nucleon scattering cross section using `MicrOMEGAs` and results from the XENON1T direct detection DM searches [90].

The input parameter ranges used for the scan are displayed in Tab. 5.1. The charged dark scalar H^\pm does not couple to fermions, its mass is therefore not constrained by B -physics bounds and chosen to vary between 65 GeV and 1000 GeV. This choice eliminates the possibility of $h \rightarrow H^+ H^-$ decays. The scalar mixing angles α_1 , α_2 and α_3 are varied between $-\pi/2$ and $\pi/2$. The requirement of boundedness from below restricts λ_2 and λ_6 to positive values, while λ_8 can also become negative [16].

5.1.2. BSMPT

The C++ code `BSMPT` [65, 66] is used for the parameter points that passed all theoretical and experimental constraints described in Sec. 5.1.1. In the context of this thesis, CP in the

	GSL			CMAES		NLOpt	
	default	modified		default	modified	default	modified
tolerance	10^{-6}	10^{-9}		10^{-5}	10^{-20}	10^{-4}	10^{-9}
MaxTries	600	2000	sigma	5	10	-	-
MaxSol	50	1000		-	-	-	-

Table 5.2.: Modified minimization parameters used for BSMPT scans. As described in Sec. 5.1.2, we increase the precision of all three minimizers, that are included in BSMPT. The table summarizes the minimizer parameters with its default and modified values.

Dark is added as a new model class to BSMPT. Its couplings to scalars, fermions and gauge bosons are encoded in the corresponding tensors of Eq. (4.1) that are defined in Sec. 4.1.

We use all three minimizers that are implemented in BSMPT for the minimization of the one-loop corrected effective potential. In order to increase the minimizer precision, accepting longer runtimes, we also changed some minimizer parameters with respect to their default values as displayed in Tab. 5.2. BSMPT offers the use of two local and one global minimization algorithms, given by:

- `gsl_multimin` from the GNU Scientific Library [91] is a multidimensional derivative-free local minimizer that features the *Nelder-Mead Simplex algorithm*. By increasing `MaxTries` and `MaxSol`, we reduce the probability of finding only a local, but not the global minimum.
- The global minimization algorithm CMAES is implemented in the C++ library `libcmaes` [92]. The initially estimated parameter error `sigma` is raised to 10.
- The compilation of non-linear optimization routines NLOpt [93] features the local minimization algorithm `GN_ORIG_DIRECT_L` which is also included in BSMPT. Its precision is enhanced by setting the relative tolerance to 10^{-9} .

The found minima are collected and numerically compared. The minimum with the lowest potential value is then taken by BSMPT as the global minimum of the potential for the given temperature T .

Like for the N2HDM [71], the temperature-dependent electroweak VEV $v(T)$ is calculated taking into account only the doublet VEVs. The singlet field is allowed to develop a VEV ω_S which is taken into account for the minimization procedure, but ω_S is dropped in the calculation of the electroweak VEV $v(T)$. Since the electroweak sphaleron transitions are due to an $SU(2)$ -vacuum transition, only the scalar $SU(2)$ degrees of freedom are taken into account for the determination of the strength of the electroweak phase transition, hence

$$v(T) = \sqrt{\omega_1^2(T) + \omega_2^2(T) + \omega_{\text{CP}}^2(T) + \omega_{\text{CB}}^2(T)}. \quad (5.4)$$

The critical temperature T_c indicates the point of the phase transition where the evolved broken minimum has developed the same potential value as the symmetric vacuum,

$$V(\omega = 0, T_c) = V(\omega \neq 0, T_c). \quad (5.5)$$

A *bisection method* is used to find T_c as explained hereafter.

The temperature range $T \in \{0 \text{ GeV}, 300 \text{ GeV}\}$ is scanned and the temperature-dependent VEV in Eq. (5.4) is determined for each temperature step. At the beginning of each step, the potential is minimized for

$$T_{\text{mid}} \equiv \frac{1}{2} (T_{\text{start}} + T_{\text{end}}) . \quad (5.6)$$

If $\omega_{\text{mid}} < 10^{-2}$, we are in the symmetric vacuum and therefore $T_c < T_{\text{mid}}$. For the next step T_{end} is set to T_{mid} . Respectively, for $\omega_{\text{mid}} \geq 10^{-2}$ we are in the broken phase and $T_c > T_{\text{mid}}$. Then T_{start} is set to T_{mid} for the next step. As soon as $T_{\text{start}} - T_{\text{end}} \leq 10^{-2}$ is reached, the phase transition is determined at $T_c \equiv T_{\text{start}}$ with $v_c \equiv v(T_c)$.

The global minimum of the one-loop corrected effective potential at $T = T_c$ is labeled using $\omega_i|_{T=T_c} \equiv \bar{\omega}_i$ with

$$\{\bar{\omega}_1, \bar{\omega}_2, \bar{\omega}_{\text{CB}}, \bar{\omega}_{\text{CP}}, \bar{\omega}_S\} . \quad (5.7)$$

During the steps of the bisection method, BSMPT discards parameter points if they fail one of the following additional checks. A discarded point is characterized by ξ_c set to some negative number:

- If $v(T = 300 \text{ GeV}) > 10^{-4}$ the symmetric VEV is not found at $T = 300 \text{ GeV}$. The temperature-dependent electroweak VEV is bounded from above by the LO electroweak VEV, $v(T) \leq 246.22 \text{ GeV}$. For temperature $T > v(T)$, the EWPT cannot be of strong first-order, $\xi_c = \frac{v_c}{T_c} < 1$. Therefore, for $T > 300 \text{ GeV}$, an SFOEWPT is not possible, ξ_c is then set to $\xi_c = -1$. The upper limit of 300 GeV is chosen to allow for numerical errors [94].
- The NLO stability of the zero temperature VEV is checked by requiring

$$\max |\omega_i(T = 0 \text{ GeV}) - v_{i,\text{EW}}| < 1 \text{ GeV} \quad (5.8)$$

with the LO electroweak VEV vector of CP in the Dark given by

$$v_{\text{EW}} \equiv (v_{1,\text{EW}}, v_{2,\text{EW}}, v_{\text{CB},\text{EW}}, v_{\text{CP},\text{EW}}, v_{S,\text{EW}}) = (246.22 \text{ GeV}, 0, 0, 0, 0) . \quad (5.9)$$

In case a point fails Eq. (5.8), the NLO VEV differs from the LO electroweak VEV at $T = 0 \text{ GeV}$ and it is discarded due to its lack of NLO vacuum stability, ξ_c is then set to $\xi_c = -2$.

- Points with an NLO VEV $v(T) \geq 255 \text{ GeV}$ at some point during the bisection method are also discarded due to unphysical and numerically unstable behavior. Then ξ_c is set to $\xi_c = -3$. This upper bound is again chosen to allow for some numerical error.
- In the fourth step, it is checked whether $v_c/T_c < \mathbf{C_PT}$, while by default $\mathbf{C_PT}$ is set to zero. If points with $v_c/T_c < \mathbf{C_PT}$ are found, ξ_c is set to $\xi_c = -4$ and the point is discarded. In the default implementation with $\mathbf{C_PT} = 0$, all points that pass all additional checks are taken into further account. In order to obtain only points that provide an SFOEWPT, $\mathbf{C_PT}$ can be set to $\mathbf{C_PT} = 1$.
- Additionally, if at $T = 0 \text{ GeV}$ the NLO VEV is below 10^{-4} GeV , or above 255 GeV , the parameter point will fail the consistency checks of BSMPT. Then ξ_c is set to $\xi_c = -5$.

In the analysis of Sec. 5.4 we found parameter points with the prospect of a really strong first-order EWPT with $\xi_c > 10$ which pass all constraints applied by **ScannerS** and BSMPT. However, they are all characterized by $T_c < T_{\text{EW}} = 100 \text{ GeV}$ and even $T_c < m_W$ for points

with $\xi_c > 10$. Therefore, they violate the assumptions made in the high-temperature expansion [57]. We moreover expect to have $T_c \sim T_{EW}$ in order to obtain an SFOEWPT. A cut on T_c discards all found SFOEWPT points with $\xi_c > 3$ when $T_c > m_W$ is required ($\xi_c > 2.5$ for the requirement $T_c > T_{EW}$).

5.2. Parameter Point Sample

Table 5.3 illustrates the parameter point sample that was generated using `ScannerS` with (without) additional DM constraints and `BSMPT`. We start with 10^6 points passing all theoretical and experimental constraints that are per default implemented in `ScannerS` and given in Tab. 5.1. Only 16% points of the original `ScannerS` sample additionally fulfill the DM constraints applied by `MicrOMEGAs`. The `BSMPT` constraints are described in Sec. 5.1.2. The additional cut on T_c is motivated in Sec. 5.1.2. After applying all constraints including the DM constraints and requiring an SFOEWPT only 2599 points (0.3%) of the initial sample are left.

5.3. VEV Configuration Analysis

Tables 5.4-5.7 provide a detailed analysis of the VEV configurations at $T = T_c$ that were found to show an SFOEWPT. We define $\omega_i|_{T=T_c} \equiv \bar{\omega}_i$. All found SFOEWPT points have $|\bar{\omega}_1| > 10^{-3}$ and $|\bar{\omega}_{CB}| < 10^{-3}$ independent of whether DM constraints are imposed. Although the charge-breaking VEV direction ω_{CB} is included in the minimization in order to be as general as possible, finding only viable SFOEWPT points with vanishing $\bar{\omega}_{CB}$ is of course reassuring. Points with $|\bar{\omega}_{CB}| > 10^{-3}$ would have to be excluded due to unphysical behavior.

Without DM constraints being imposed, we find that 1.2% of the SFOEWPT points yield at least one additional dark VEV $|\bar{\omega}_i| > 10^{-3}$ with $i \in \{2, S, CP\}$. The minimal and maximal values of non-zero VEVs are displayed in Tab. 5.4. Detailed VEV configurations can be found in Tab. 5.5. A percentage of 98.8% of all SFOEWPT points only have $|\bar{\omega}_1| > 10^{-3}$. For 1.2%, we find VEV configurations where all except $\bar{\omega}_{CB}$ participate in the phase transition, as only $|\bar{\omega}_{CB}| < 10^{-3}$. Two VEV configurations show only $|\bar{\omega}_S| > 10^{-3}$ or $|\bar{\omega}_S|, |\bar{\omega}_2| > 10^{-3}$ in addition to $|\bar{\omega}_1| > 10^{-3}$.

Only 7.3% of the SFOEWPT points of the sample additionally pass the DM constraints that were discussed in Sec. 5.1.1. Table 5.6 displays the minimal and maximal values

<code>ScannerS</code>	<code>BSMPT</code>	SFOEWPT	$T_c > T_{EW}$
$10^6(100\%)$	502 065(50%)	38 737(4%)	35 540(4%)
<code>ScannerS</code> and <code>MicrOMEGAs</code>	<code>BSMPT</code>	SFOEWPT	$T_c > T_{EW}$
164 351(16%)	98 123(10%)	2806(0.3%)	2599(0.3%)

Table 5.3.: Benchmark point sample size after generating the sample with `ScannerS` and optionally including DM constraints with `MicrOMEGAs`. Further constraints are imposed by `BSMPT`, see Sec. 5.1.2. An SFOEWPT requires $\xi_c \gtrsim 1$, with ξ_c being the strength of the EWPT, defined in Eq. (2.22). Furthermore, we restrict $T_c > T_{EW}$ as argued in Sec. 5.1.2. The numbers in the brackets give the percentage of the original sample generated with `ScannerS`.

	number	min	max
# SFOEWPT	35 540		
$ \bar{\omega}_1 > 10^{-3}$	35 540	111.693	254.999
$ \bar{\omega}_2 > 10^{-3}$	418	0.001	75.037
$ \bar{\omega}_{\text{CB}} > 10^{-3}$	0	0	0
$ \bar{\omega}_{\text{CP}} > 10^{-3}$	417	0.009	90.597
$ \bar{\omega}_S > 10^{-3}$	419	0.005	77.571

Table 5.4.: VEV configurations found by BSMPT (without DM constraints) that have $|\bar{\omega}_i| > 10^{-3}$ with $i \in \{1, 2, \text{CB}, \text{CP}, S\}$. The minimal and maximal VEV values are also displayed. Units are in GeV. We require $T_c > T_{\text{EW}}$, as discussed in Sec. 5.1.2.

VEVs $> 10^{-3}$	$ \bar{\omega}_1 $	$ \bar{\omega}_1 , \bar{\omega}_2 ,$ $ \bar{\omega}_{\text{CP}} , \bar{\omega}_S $	$ \bar{\omega}_1 , \bar{\omega}_S $	$ \bar{\omega}_1 , \bar{\omega}_2 ,$ $ \bar{\omega}_S $
found by				
GSL	20 689	87	1	0
CMAES	10 498	288	0	1
NLopt	3934	42	0	0
# total	35 121	417	1	1

Table 5.5.: Detailed VEV configurations found by BSMPT for the sample without DM constraints. We require $T_c > T_{\text{EW}}$, as discussed in Sec. 5.1.2. The table additionally includes information on the minimizers. GSL is observed to find the majority of VEV configurations with only $|\bar{\omega}_1| > 10^{-3}$. VEV configurations with non-zero dark VEVs at $T = T_c$ are preferably found by CMAES. See Sec. 5.1.2 for a description of the minimizers that are implemented in BSMPT.

	number	min	max
# SFOEWPT	2599		
$ \bar{\omega}_1 > 10^{-3}$	2599	125.374	254.880
$ \bar{\omega}_2 > 10^{-3}$	38	0.258	71.089
$ \bar{\omega}_{\text{CB}} > 10^{-3}$	0	0	0
$ \bar{\omega}_{\text{CP}} > 10^{-3}$	38	0.115	43.279
$ \bar{\omega}_S > 10^{-3}$	38	9.283	62.209

Table 5.6.: VEV configurations found by BSMPT with $|\bar{\omega}_i| > 10^{-3}$ for $i \in \{1, 2, \text{CB}, \text{CP}, S\}$ and minimal and maximal VEV values are displayed for DM constraints imposed. Units are in GeV. We require $T_c > T_{\text{EW}}$, as discussed in Sec. 5.1.2.

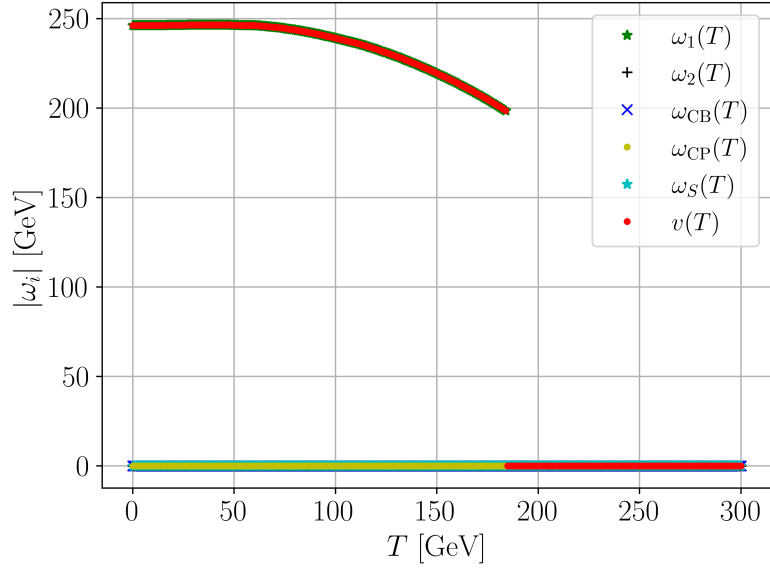
VEVs $> 10^{-3}$	$ \bar{\omega}_1 $	$ \bar{\omega}_1 , \bar{\omega}_2 ,$ $ \bar{\omega}_{\text{CP}} , \bar{\omega}_S $
found by		
GSL	1235	4
CMAES	1041	28
NLopt	285	6
# total	2561	38

Table 5.7.: The number of SFOEWPT points and their respective VEV configurations are shown for the sample with imposed DM constraints. We require $T_c > T_{\text{EW}}$, as discussed in Sec. 5.1.2. The table additionally includes information on the minimizers. Similarly compared to the analysis without implying DM constraints, see Tab. 5.5, **GSL** finds the most SFOEWPT points that only show $|\bar{\omega}_1| > 10^{-3}$. **CMAES** in addition is observed to find most SFOEWPT points that only show $|\bar{\omega}_{\text{CB}}| < 10^{-3}$.

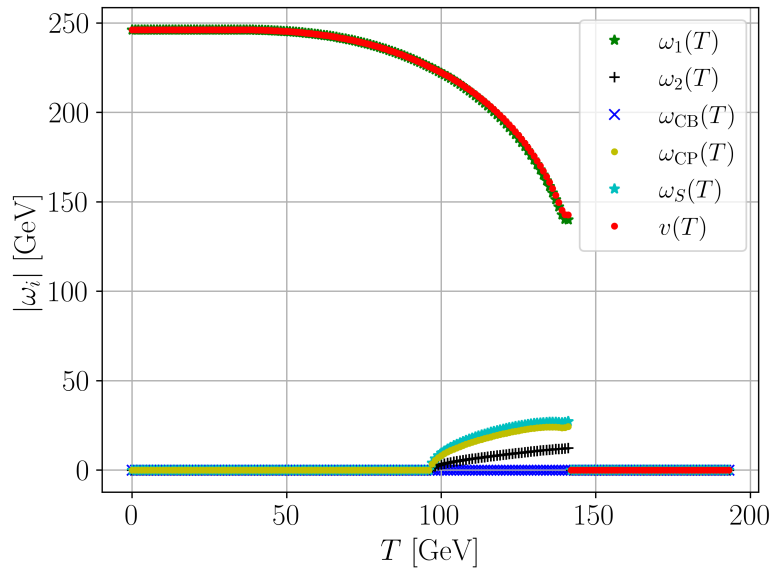
of the five VEV directions. Table 5.7 illustrates the detailed VEV configurations that were found by BSMPT. 98.5% of the SFOEWPT points that pass the DM constraints only have $|\bar{\omega}_1| > 10^{-3}$. All other found SFOEWPT points, 1.5% of the sample, only show $|\bar{\omega}_{\text{CB}}| < 10^{-3}$, with all other dark VEVs $> 10^{-3}$ at $T = T_c$.

In Fig. 5.1 we show the evolution of all VEV directions with the temperature T for the two categories of points that are found when imposing DM constraints, see Tab. 5.7. Figure 5.1a shows the benchmark point F1R57. Its VEV evolution is exemplary for 98.5% of the SFOEWPT points that pass the DM constraints and all only have $|\bar{\omega}_1| > 10^{-3}$ and all other dark VEVs $|\bar{\omega}_i| < 10^{-3}$ with $i \in \{2, \text{CB}, \text{CP}, S\}$. Figure 5.1b shows the benchmark point F610R819 that is one of the 38 or 1.5% of the SFOEWPT points that pass the DM constraints and only show $|\bar{\omega}_{\text{CB}}| < 10^{-3}$ with all other dark VEVs $> 10^{-3}$ at $T = T_c$. Both benchmark points are specified in App. B. As described in Sec. 2.3, an SFOEWPT is characterized by a strong discontinuity in the order parameter, the temperature-dependent VEV $v(T)$ (red) of Eq. (5.4). Both parameter points in Fig. 5.1 show such an SFOEWPT. For 5.1a, only $|\bar{\omega}_1|$ (green) is larger than 10^{-3} and therefore participates in the phase transition. For 5.1b also all dark VEVs contribute around the phase transition, except for the charge-breaking VEV (dark blue) which is always found to be $|\bar{\omega}_{\text{CB}}| < 10^{-5}$.

In case $|\bar{\omega}_{\text{CP}}| > 10^{-3}$, we have *spontaneous* CPV at finite temperature. In Fig. 5.2 we show $|\bar{\omega}_{\text{CP}}|$ as a function of $|\text{Im}(A)|$ normalized to $|\text{Re}(A)|$ for all SFOEWPT points that pass the



(a) With all dark VEVs zero



(b) With non-zero dark VEVs

Figure 5.1.: The evolution of the finite-temperature VEVs $|\omega_i|$ with $i \in \{1, 2, \text{CB}, \text{CP}, S\}$ as a function of the temperature T . Figure 5.1a shows the point F1R57, Fig. 5.1b shows the VEV evolution for the point F610R819. The benchmark points F1R57 and F610R819 are given in App. B.

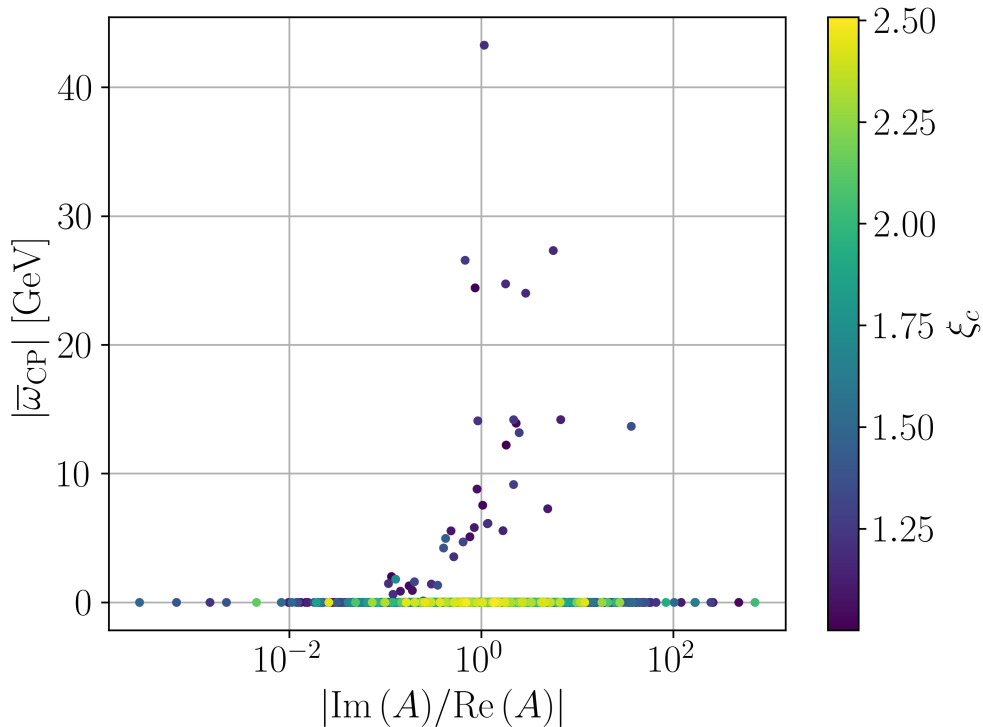


Figure 5.2.: The absolute value of the CP -violating finite-temperature VEV $\bar{\omega}_{CP}$ that minimizes the one-loop corrected effective potential at $T = T_c$ versus the absolute value of the imaginary part of the trilinear coupling $\text{Im}(A)$, normalized to its real part, $\text{Re}(A)$, for all viable SFOEWPT points that are found when implying DM constraints. The strength of the phase transition ξ_c is indicated by the color code.

DM constraints. The color indicates the strength of the phase transition, ξ_c , for $\xi_c \gtrsim 1$. CP is explicitly violated by $\text{Im}(A) \neq 0$, as discussed in Chapter 3. Today, at $T = 0 \text{ GeV}$, CP can only be generated explicitly, as $\omega_{CP}|_{T=0 \text{ GeV}} \equiv v_{CP} = 0$. If, however, $|\bar{\omega}_{CP}| > 0$, CP is violated spontaneously at $T = T_c$. In total, we find 38 SFOEWPT points that pass the DM constraints *and* yield spontaneous CPV at $T = T_c$. Figure 5.2 shows that high $\xi_c > 2.2$ are only found for points with no spontaneous, but explicit CPV with $|\text{Im}(A)| \sim 1$. The highest ξ_c -value of $\xi_c = 2.507$ is found for $|\bar{\omega}_{CP}| = 2.5 \times 10^{-6} \text{ GeV}$ and $|\text{Im}(A)| = 1.372 \text{ GeV}$. Furthermore, we find SFOEWPT points with $10^{-6} \text{ GeV} < |\bar{\omega}_{CP}| < 43.28 \text{ GeV}$, compare also with Tab. 5.6.

The 38 found SFOEWPT points that show spontaneous CPV at finite temperature additionally have $|\bar{\omega}_2| > 10^{-3}$ and $|\bar{\omega}_S| > 10^{-3}$. This means that for these points at finite temperature, the \mathbb{Z}_2 -symmetry is broken and the dark charge is no longer a conserved quantum number. Therefore, previously dark particles will mix with the particles from the first doublet. Consequently, additional non-standard CPV that is a necessary ingredient for an EWBG in order to generate the measured BAU can in this case be transferred to the SM-like couplings to fermions at finite temperature.

In conclusion, CP in the Dark provides points that enable the interesting feature of spontaneous CPV at finite temperature. However, unfavorably in context of an EWBG scenario, the strength of spontaneous CPV seems not correlated with the strength of the EWPT, as the points with large $|\bar{\omega}_{CP}|$ do not in addition show a large ξ_c -value.

5.4. SFOEWPT in CP in the Dark

Figures 5.3-5.5 show the distribution of points that provide an SFOEWPT in the dark mass plane, in particular Fig. 5.3 displays them in the plane of the mass of the lightest neutral dark scalar particle, m_{h_1} , and the mass of the charged dark scalar, m_{H^\pm} . Figure 5.4 shows them in the $m_{H^\pm} - m_{h_2}$ -plane, with m_{h_2} , the mass of the second-lightest dark neutral scalar. In Fig. 5.5 we display the point sample in the plane of the heaviest neutral dark scalar mass m_{h_3} and the charged dark scalar mass m_{H^\pm} . The left plots in each of these figures are without imposing the DM constraints, the plots on the right side of these figures are with imposed DM constraints, that were discussed in Sec. 5.1.1. The gray points are benchmark scenarios generated by **ScannerS**, hence fulfilling experimental and theoretical constraints, as described in Sec. 5.1.1, while the orange points additionally pass all tests by **BSMPT**, see Sec. 5.1.2 and provide an NLO stable EW vacuum. The color code shows the strength of the EWPT $\xi_c \gtrsim 1$ and thus indicates the parameter points with an SFOEWPT.

Figures 5.6-5.8 are the corresponding figures to 5.3-5.5, but with additionally applying a cut on the critical temperature, $T_c > T_{EW}$. As already discussed in Sec. 5.2, the DM constraints impose essential bounds on our parameter sample. The amount of points and their distribution in the dark mass plane gets significantly restricted. With additionally imposed $T_c > T_{EW}$ the highest found ξ_c -value is below $\xi_c = 2.5$. As seen in these plots, the theoretical and experimental constraints allow for a large range for the Higgs boson masses. The additional requirement of an SFOEWPT, however, reduces significantly the available parameter points, but the overall range of Higgs masses is still possible. We emphasize that a single point in a region is sufficient to underline this statement, since a dedicated scan in this respective region would yield more similar points. To summarize, we do not observe a favored mass region for an SFOEWPT. The DM constraints might give a stronger constraint on the different mass planes.

Let us discuss in more detail the results when we impose all possible constraints, namely also DM constraints and the requirement of $T_c > T_{EW}$, i.e. Figs. 5.6-5.8 (right). Figure 5.6 shows the $m_{h_1} - m_{H^\pm}$ -plane. As can be inferred from the plot, we find viable SFOEWPT points for the whole scanned range of m_{H^\pm} and also for a broad mass range of m_{h_1} . In Fig. 5.7 we show the found SFOEWPT points in the plane of the second-lightest neutral dark scalar mass m_{h_2} and the charged dark scalar mass m_{H^\pm} . The mass m_{h_2} is found to be preferably in the range of m_{H^\pm} for points with an SFOEWPT, still the absolute deviation in the two masses can be of up to 335.81 GeV for some SFOEWPT points, cf. Fig. 5.9b. Figure 5.8 displays the viable SFOEWPT points with DM constraints and the cut $T_c > T_{EW}$ in the $m_{h_3} - m_{H^\pm}$ -plane. We find viable SFOEWPT points for $m_{h_3} < m_{H^\pm}$, $m_{h_3} \sim m_{H^\pm}$ and $m_{h_3} > m_{H^\pm}$. The plots show that when imposing all constraints, we do not find a point in our sample with $m_{h_3} < m_h = 125.1$ GeV and simultaneously an SFOEWPT, while m_{h_2} can still be below m_h for a viable SFOEWPT point.

In order to further illustrate the relations between the neutral and charged dark masses, we show the SFOEWPT points in the plane spanned by their mass differences $m_{H^\pm} - m_{h_i}$ with $i \in \{1, 2, 3\}$ in Fig. 5.9. As we do not find a favored mass region for an SFOEWPT, the ranges of the mass differences for the SFOEWPT point distribution are dictated by the mass hierarchy

$$m_{h_1} < m_{h_2} < m_{h_3}, \quad (5.10)$$

the scan range $m_{H^\pm} \in \{65, 1000\}$ GeV, as well as the point distribution and density from **ScannerS**. Note, that the latter is not physical and as soon as we are able to obtain one

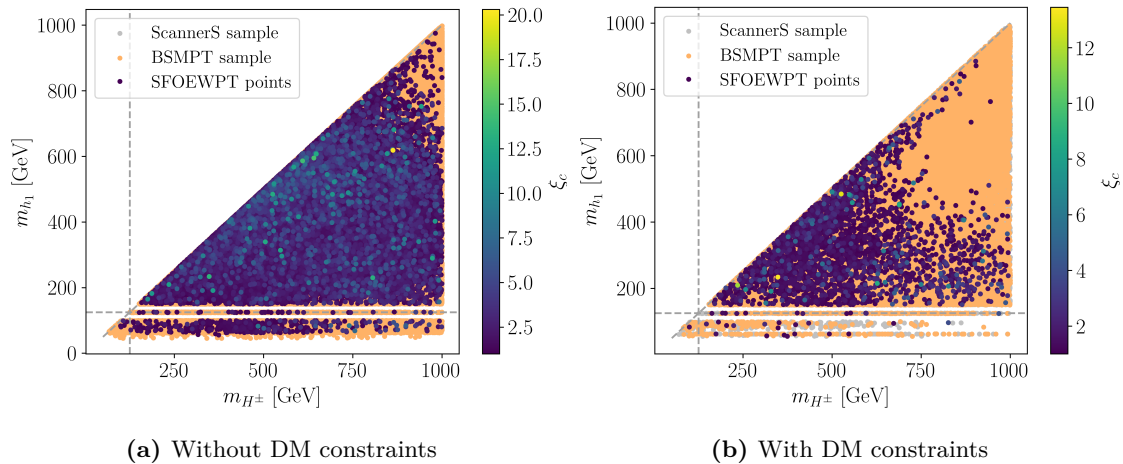


Figure 5.3.: Benchmark point sample (see Tab. 5.3) in the mass plane of the lightest neutral dark scalar mass, m_{h_1} , versus the charged dark scalar mass, m_{H^\pm} . Gray points are those of the full **ScannerS** sample, orange points pass the BSMPT constraints, and the colored points have $\xi_c \gtrsim 1$, with the color code indicating the size of ξ_c . The left figure does not include DM constraints, in the right figure they are included.

point in a certain mass region that passes the theoretical and experimental constraints of **ScannerS**, a dedicated scan will find more points in this region. We observe viable SFOEWPT points for nearly the whole scanned range of m_{H^\pm} , cf. Figs. 5.6-5.8. In Fig. 5.9a we do not only observe viable SFOEWPT points in a broad $m_{H^\pm} - m_{h_1}$ range, but also in a broad, but smaller $m_{H^\pm} - m_{h_3}$ range. Figure 5.9b shows a much smaller range of $m_{H^\pm} - m_{h_2}$ for viable SFOEWPT points. In Fig. 5.9c the viable SFOEWPT points are displayed in the plane of $m_{H^\pm} - m_{h_2}$ versus $m_{H^\pm} - m_{h_3}$ and $m_{H^\pm} - m_{h_1}$ is indicated by the color code. Large $m_{H^\pm} - m_{h_1}$ are only obtained for small $m_{H^\pm} - m_{h_3}$, due to the mass hierarchy, see Eq. (5.10).

We define the mass asymmetry $\Delta_{m_1 m_2}$ for two masses m_1 and m_2 as

$$\Delta_{m_1 m_2} = \frac{m_1 - m_2}{m_1 + m_2}. \quad (5.11)$$

Figure 5.10 displays in color all SFOEWPT points that pass the DM constraints in the plane that is spanned by $\Delta_{m_{h_1} m_{H^\pm}}$ and $\Delta_{m_{h_2} m_{H^\pm}}$. The size of $\Delta_{m_{h_3} m_{H^\pm}}$ for the SFOEWPT points is indicated by the color code. In agreement with the previous plots, we find that a broad range of $\Delta_{m_{h_1} m_{H^\pm}}$ yields SFOEWPT points. The mass asymmetry $\Delta_{m_{h_2} m_{H^\pm}}$ is preferably low, since $m_{h_2} \sim m_{H^\pm}$ was found as the favored mass hierarchy for an SFOEWPT. Only in cases where $\Delta_{m_{h_1} m_{H^\pm}}$ or $\Delta_{m_{h_2} m_{H^\pm}}$ are small, $\Delta_{m_{h_3} m_{H^\pm}}$ can reach values above $> 60\%$. This is due to the chosen mass hierarchy, see Eq. (5.10).

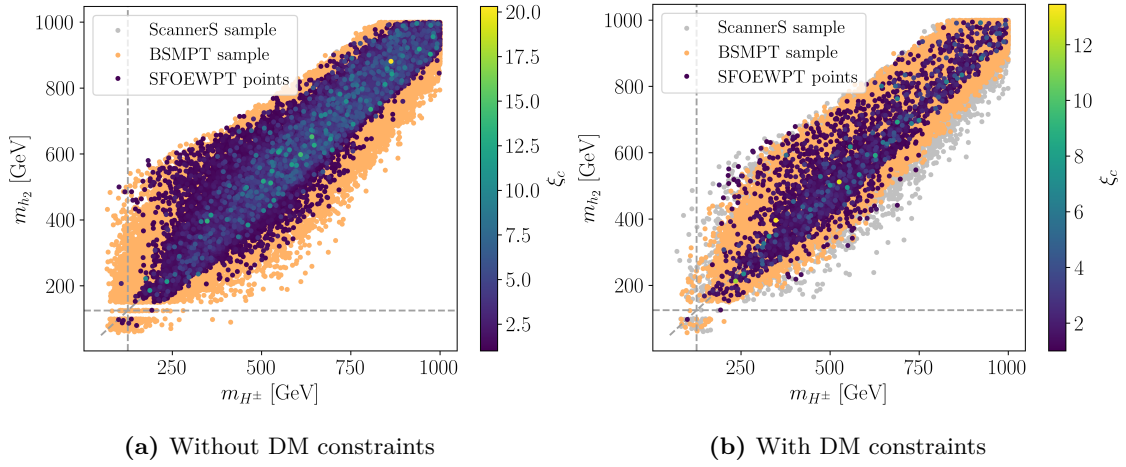


Figure 5.4.: Same as Fig. 5.3, but for the next-to-lightest neutral dark scalar mass m_{h_2} versus m_{H^\pm} .

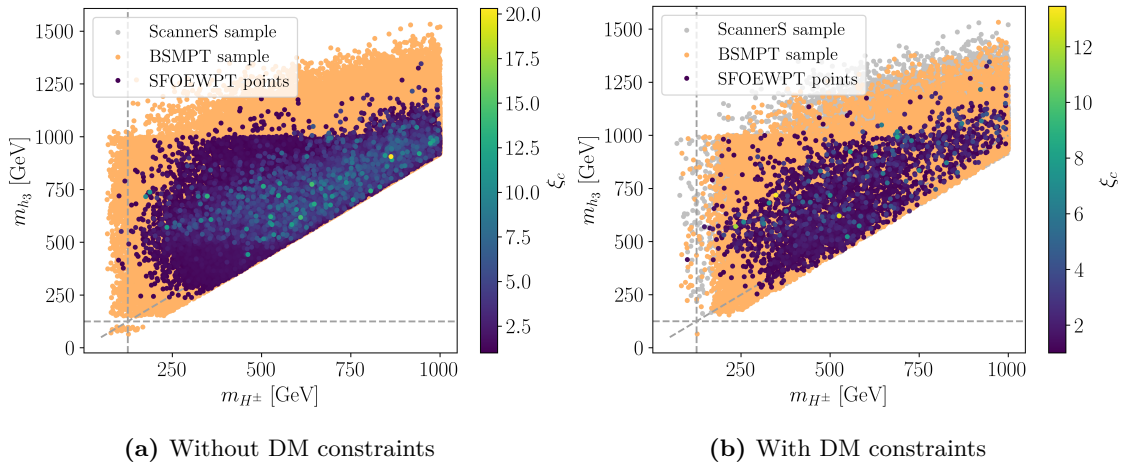


Figure 5.5.: Same as Fig. 5.3, but for the heaviest neutral dark scalar mass m_{h_3} versus m_{H^\pm} .

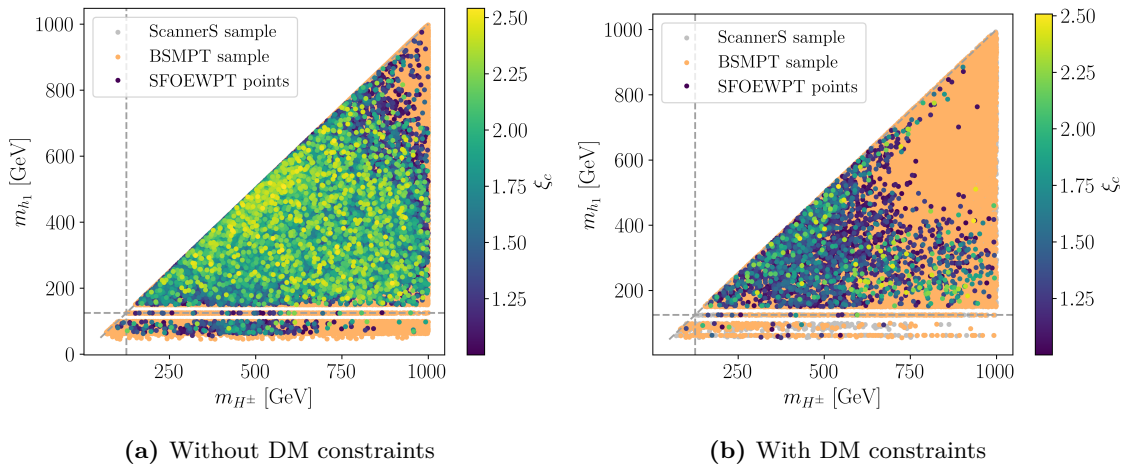


Figure 5.6.: Same as Fig. 5.3, but with additionally imposing $T_c > T_{EW}$ on the SFOEWPT points.

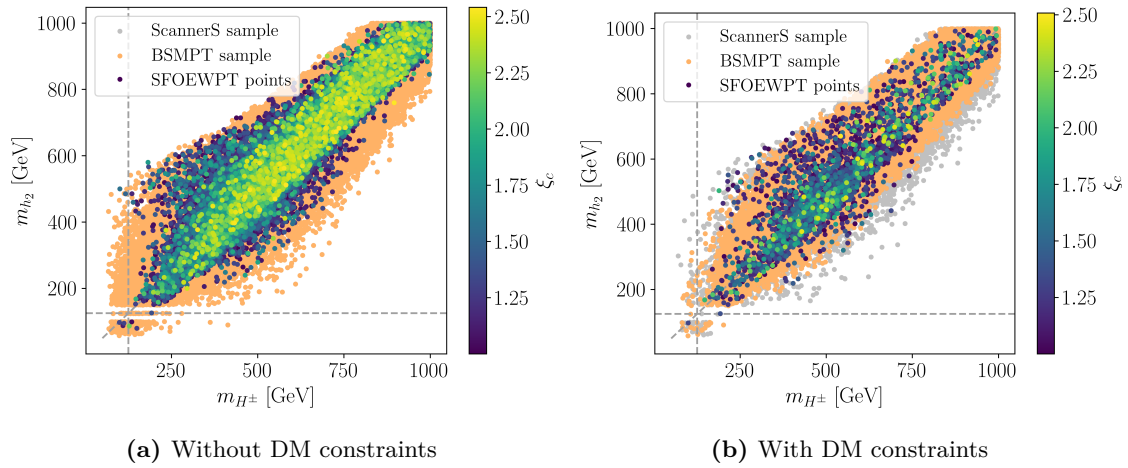


Figure 5.7.: Same as Fig. 5.4, but with additionally imposing $T_c > T_{EW}$ on the SFOEWPT points.

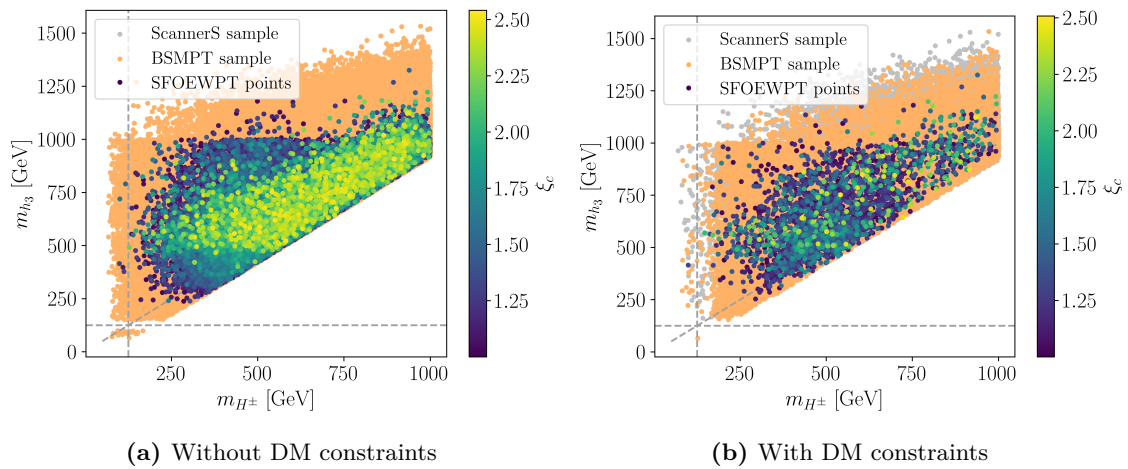


Figure 5.8.: Same as Fig. 5.5, but with additionally imposing $T_c > T_{EW}$ on the SFOEWPT points.

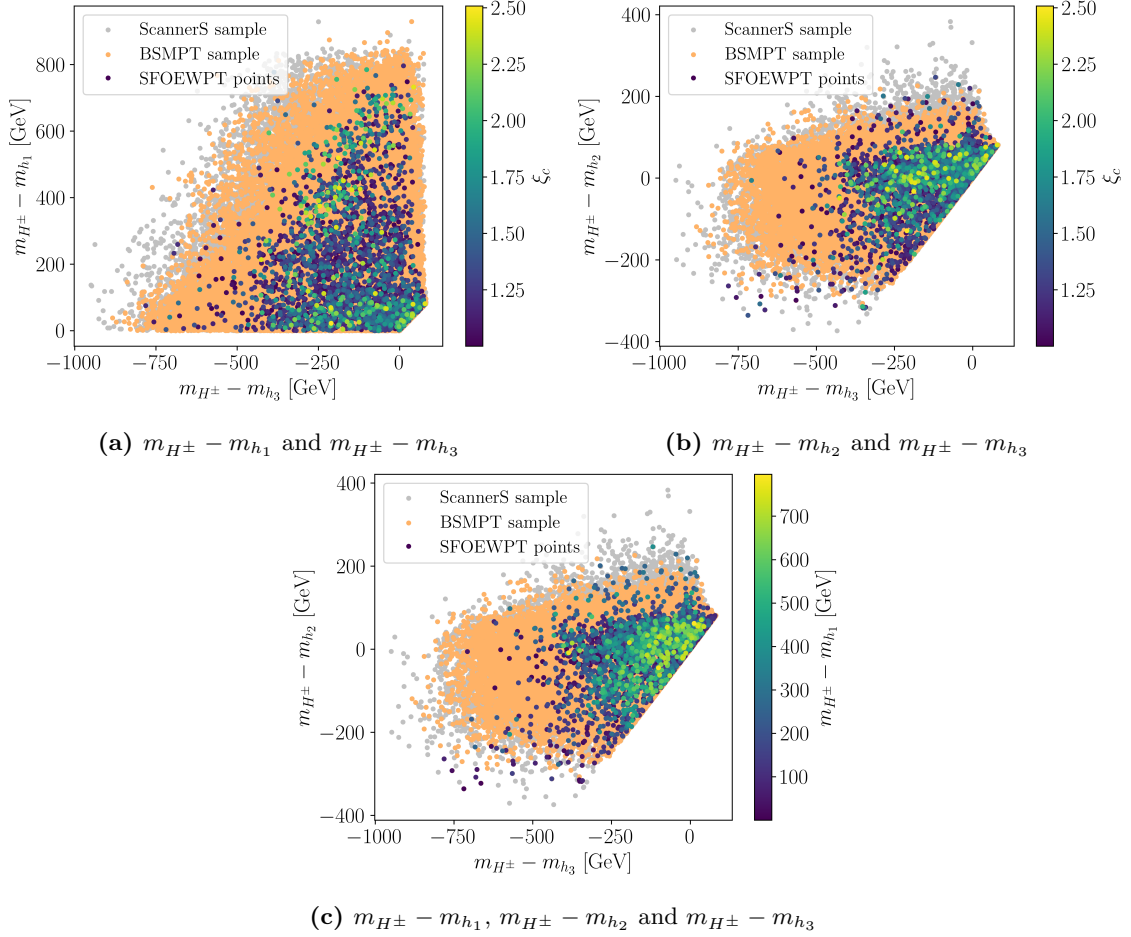


Figure 5.9.: Benchmark point sample (see Tab. 5.3) with imposed DM constraints and additional cut for the found SFOEWPT points on the critical temperature $T_c > T_{EW}$ in the plane spanned by the mass differences $m_{H^\pm} - m_{h_i}$ with $i \in \{1, 2, 3\}$. Gray points pass all **ScannerS**-tests, orange points additionally pass all checks of **BSMPT**. Figure 5.9a and 5.9b include the information on the strength of the EWPT ξ_c as indicated by the color code. Figure 5.9c combines information on all mass differences.

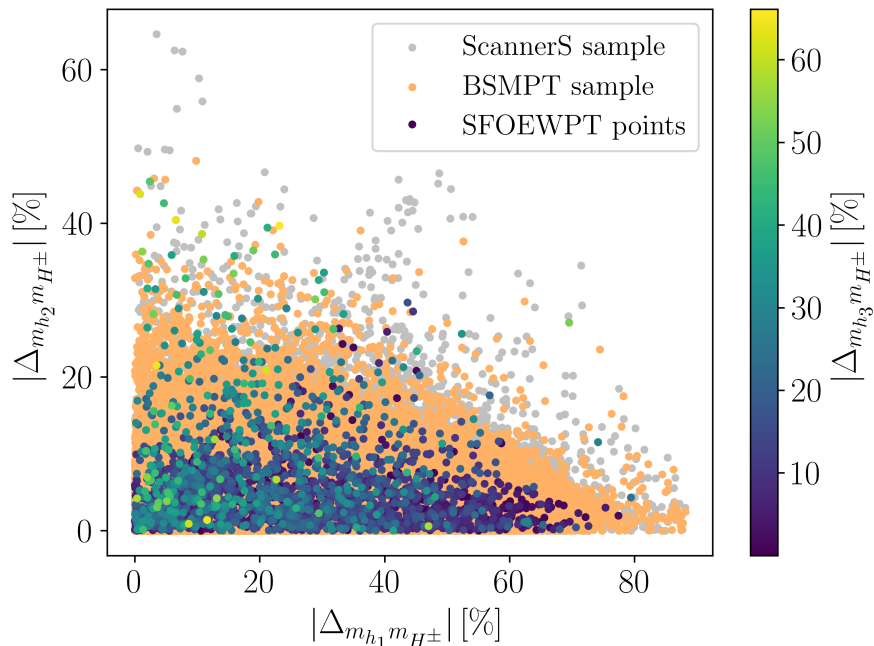


Figure 5.10.: Scatter plot in the plane of the mass asymmetries $|\Delta_{m_{h_1} m_{H^\pm}}|$ and $|\Delta_{m_{h_2} m_{H^\pm}}|$ with $\Delta_{m_1 m_2}$ defined in Eq. (5.11) for the points obtained from the **ScannerS** scan with DM constraints (gray), after imposing the BSMPT constraints (orange) and additionally requiring an SFOEWPT (color). The color code indicates the size of $|\Delta_{m_{h_3} m_{H^\pm}}|$, where $T_c > T_{EW}$ is imposed.

5.5. Doublet and Singlet Admixture

As discussed in Chapter 3, CP in the Dark features three neutral dark scalars h_i with $i \in \{1, 2, 3\}$ that are admixtures of the neutral CP -even scalars ζ_2 , ζ_S and the neutral CP -odd scalar Ψ_2 ,

$$h_i = R_{i1}\zeta_2 + R_{i2}\Psi_2 + R_{i3}\zeta_S. \quad (5.12)$$

The rotation matrix elements R_{ij} with $i, j \in \{1, 2, 3\}$ are defined in Eq. (3.13). We define the admixture $\Sigma_{h_i}^{\phi_j}$ of the field ϕ_j in the gauge basis to the field h_i in the mass basis as

$$\Sigma_{h_i}^{\phi_j} \equiv (R_{ij})^2. \quad (5.13)$$

In Fig. 5.11 we illustrate the distribution of the found SFOEWPT points in the plane which is spanned by the doublet admixtures $\Sigma_{h_i}^{\zeta_2}$ and $\Sigma_{h_i}^{\Psi_2}$ and the singlet admixture $\Sigma_{h_i}^{\zeta_S}$ against the neutral dark scalar masses m_{h_i} , respectively.

We find SFOEWPT points over the whole range of doublet and singlet admixtures to the dark matter candidate h_1 . On the other hand viable SFOEWPT points show preferably a low singlet admixture to the second-lightest neutral dark particle h_2 , but the whole range of doublet admixtures. Note, that this point distribution is very likely a scan artifact of **ScannerS**. We find some viable SFOEWPT points where h_2 also shows a large singlet admixture. Therefore, this parameter space region is theoretically and experimentally allowed and a more dedicated scan is expected to yield more points with high singlet and low doublet admixtures for h_2 . The heaviest neutral dark scalar h_3 again provides viable SFOEWPT points for all combinations of doublet and singlet admixtures.

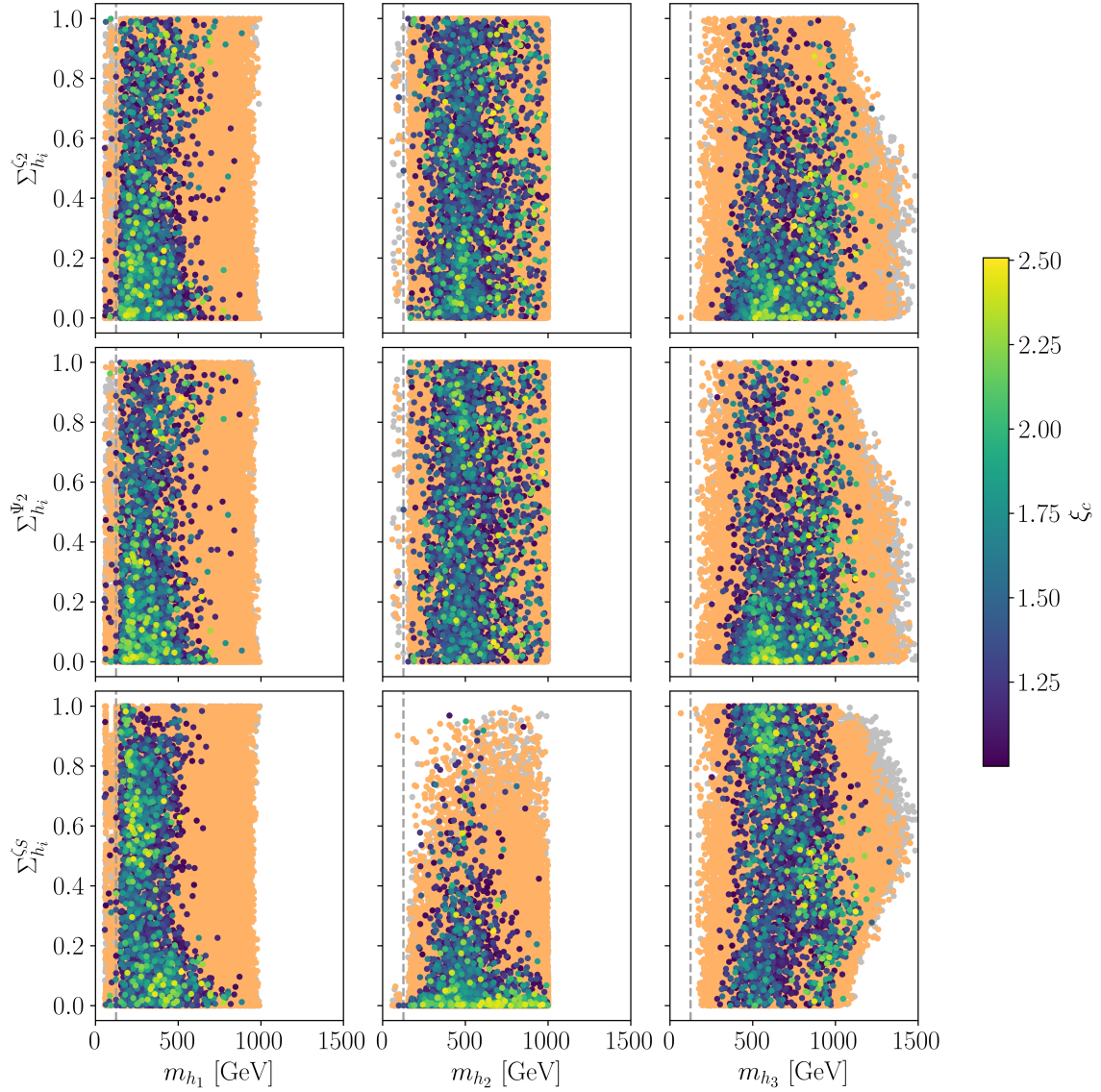


Figure 5.11.: CP -even, CP -odd doublet and singlet admixtures $\Sigma_{h_i}^{\zeta_2}$, $\Sigma_{h_i}^{\Psi_2}$ and $\Sigma_{h_i}^{\zeta_S}$, respectively, to the neutral dark scalars h_1 (left), h_2 (middle) and h_3 (right), as defined in Eqs. (5.12) and (5.13) as a function of the corresponding Higgs mass m_{h_i} . The color code is the same as in Fig. 5.8. DM constraints are included. Only points with $T_c > T_{\text{EW}}$ are considered as viable SFOEWPT points, as discussed in Sec. 5.1.2.

5.6. Trilinear Higgs Self-Couplings

In this section we discuss the behavior of the leading-order and of the next-to-leading order trilinear Higgs self-couplings of the SM-like Higgs boson h normalized to the corresponding SM values $\lambda_{hhh}^{(0),\text{SM}}$ and $\lambda_{hhh}^{(1),\text{SM}}$, respectively, in view of an SFOEWPT. The leading-order trilinear SM-Higgs self-coupling is derived as the third derivative with respect to h of Eq. (2.2) yielding

$$\lambda_{hhh}^{(0),\text{SM}} = \frac{3m_h^2}{v}. \quad (5.14)$$

The dominant top-quark contribution to the one-loop correction of the trilinear SM-Higgs self-coupling has been given in [95],

$$\lambda_{hhh}^{(1),\text{SM}} = \frac{3m_h^2}{v} \left[1 - \frac{N_c}{3\pi^2} \frac{m_t^4}{v^2 m_h^2} \left\{ 1 + \mathcal{O}\left(\frac{m_h^2}{m_t^2}, \frac{p_i^2}{m_t^2}\right) \right\} \right], \quad (5.15)$$

with the mass of the top quark m_t , the momenta p_i , $i \in \{1, 2, 3\}$, of the external Higgs bosons and the number of colors $N_c = 3$.

The LO and NLO trilinear Higgs self-couplings for CP in the Dark are obtained from BSMPT. We compare the ratios between the SM-Higgs trilinear self-couplings $\lambda_{hhh}^{(0),\text{SM}}$ and $\lambda_{hhh}^{(1),\text{SM}}$ and the trilinear self-couplings derived for CP in the Dark. In BSMPT, they are determined numerically by calculating the third derivatives of the effective potential with respect to the scalar fields [65, 66].

The SM-like Higgs boson of CP in the Dark is referred to as h , therefore the leading-order hhh -coupling ratio is exactly determined to be

$$\frac{\lambda_{hhh}^{(0)}}{\lambda_{hhh}^{(0),\text{SM}}} = 1. \quad (5.16)$$

For the next-to-leading order SM-like Higgs self-coupling ratio, we obtain for all viable parameter points that pass all experimental and theoretical constraints of **ScannerS** and BSMPT values in the range of

$$-7.878 < \frac{\lambda_{hhh}^{(1)}}{\lambda_{hhh}^{(1),\text{SM}}} < 1.743. \quad (5.17)$$

The viable SFOEWPT points yield ratios in the reduced range of

$$-0.420 < \frac{\lambda_{hhh}^{(1)}}{\lambda_{hhh}^{(1),\text{SM}}}\Big|_{\xi_c > 1} < 1.743. \quad (5.18)$$

The increase of the lower bound when requiring an SFOEWPT is also observed for the N2HDM in [71]. It is stated in [70] for the C2HDM and again observed in [71] for the N2HDM, that an SFOEWPT favors large trilinear Higgs self-couplings. For CP in the Dark, we find SFOEWPT points in the coupling range of Eq. (5.18), which is shifted towards more positive values compared to the range of all viable parameter points given in Eq. (5.17). Additionally, the strength of the EWPT does not seem to directly scale with the size of the trilinear couplings. In contrast to the N2HDM, we observe an SFOEWPT to be possible not only for SM-like or enhanced, but even for vanishing loop-corrected trilinear Higgs couplings.

Figure 5.12 shows the trilinear Higgs self-coupling ratios to the SM-Higgs trilinear self-coupling for the couplings between the SM-like Higgs h and two neutral dark scalars $h_i h_i$ with $i \in \{1, 2, 3\}$ for the parameter sample that passes the constraints by **ScannerS** (gray) and **BSMPT** (orange) and the found viable SFOEWPT points (color). Displayed are the NLO ratios versus the LO ratios. The strength ξ_c of the SFOEWPT is again indicated by the color code. The trilinear couplings between the SM-like Higgs h and two neutral dark scalars $h_i h_i$, $i \in \{1, 2, 3\}$, play a role in decays of h to dark particles. Such decays are important for collider searches for DM particles. We clearly observe large allowed coupling ranges over the parameter space that yield viable SFOEWPT points in Fig. 5.12.

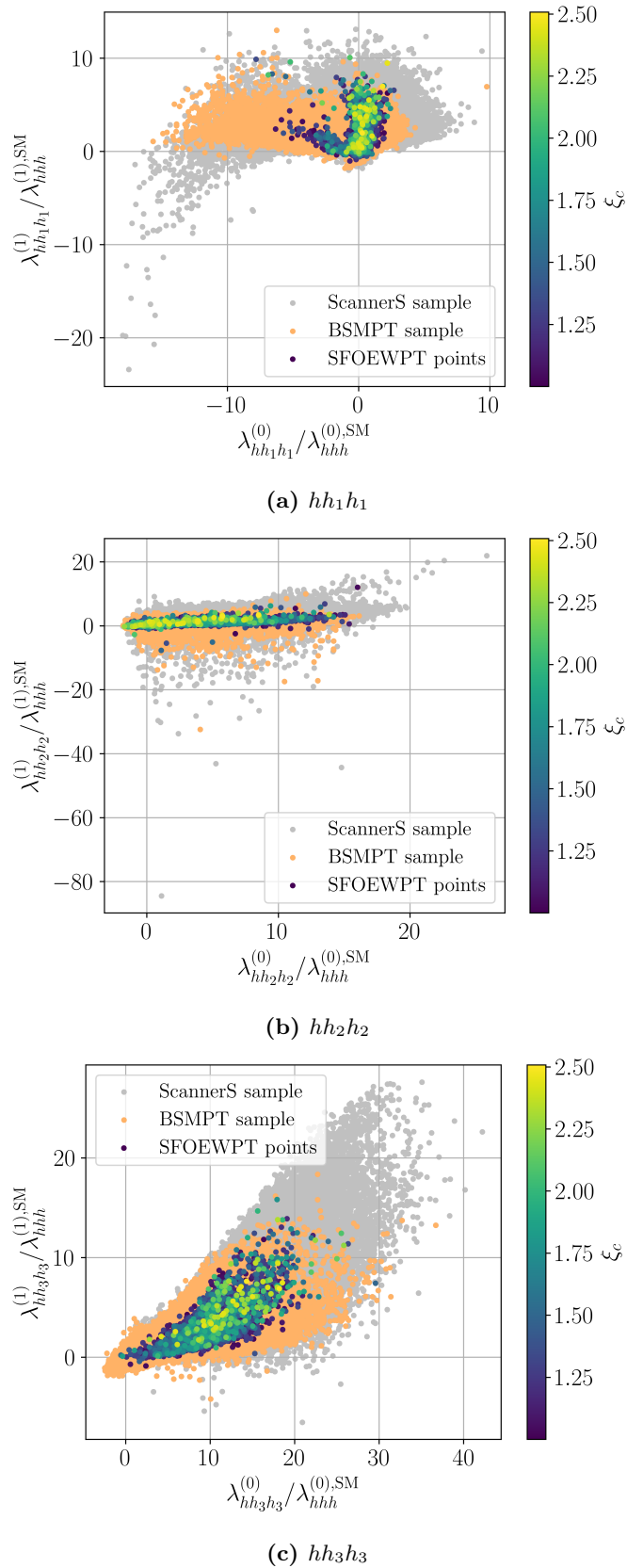


Figure 5.12.: The ratio of the trilinear coupling normalized to the SM-Higgs trilinear coupling at NLO as function of the corresponding LO quantity for the trilinear coupling of the SM-like Higgs boson h to a pair of two lightest dark neutral bosons h_1 (top), a pair of two second-lightest dark neutral bosons h_2 (middle) and a pair of two heaviest dark neutral bosons h_3 (bottom). Gray points pass all **ScannerS**-tests, including DM constraints, orange points additionally pass all checks of **BSMP**. The color code indicates the strength $\xi_c \gtrsim 1$ of the SFOEWPT. Only points with $T_c > T_{EW}$ are considered as viable SFOEWPT points.

5.7. DM observables

Figure 5.13 shows the relic density, which has been calculated assuming the freeze-out mechanism, with `MicrOMEGAs` [87–89] which is linked to `ScannerS` [75, 76], versus the DM mass m_{h_1} . Again points that pass all theoretical and experimental constraints of `ScannerS` are colored in gray while points that additionally pass the constraints of `BSMPT` are colored in orange. The size of ξ_c for viable SFOEWPT points is indicated by the color code. The majority of viable SFOEWPT points is found to be underabundant. We find three SFOEWPT points that are able to produce a relic density that exceeds $\Omega_{\text{prod}} h^2 > 0.11$. The maximally produced relic density by parameter points providing an SFOEWPT is

$$\Omega_{\text{prod}}^{\text{max}} h^2 = 0.114, \quad (5.19)$$

and therefore is not able to saturate the experimentally measured relic density within 1σ -limits, $\Omega_{\text{obs}} h^2 = 0.1200 \pm 0.0012$ [4]. Note, that Fig. 5.13 shows that it is possible to generate parameter points that pass the `ScannerS` bounds and lie within the 1σ limits for the measured relic density. We find 222 such points, that all have $m_{h_1} = 190.193$ GeV, in our parameter sample, see Sec. 5.2. They are additionally colored in red in Fig. 5.13.

Figure 5.14 illustrates the effective spin-independent (SI) direct detection DM-nucleon cross section $f_{\chi\chi} \cdot \sigma$ versus the DM mass m_{h_1} . The SI direct detection DM-nucleon cross section σ has to be rescaled with the renormalized relic density to account for the underabundance of the DM candidate, cf. also [96, 97],

$$\sigma \cdot f_{\chi\chi} \equiv \sigma \cdot \frac{\Omega_{\text{prod}} h^2}{\Omega_{\text{obs}} h^2}. \quad (5.20)$$

The required values are obtained with `MicrOMEGAs`. All parameter points are below the `XENON1T` exclusion limit [90], as this is already required in the checks of `ScannerS`. We find that the majority of SFOEWPT points are above the neutrino floor, which is displayed by the gray shaded region, and in reach of the projected sensitivity of the `XENONnT` experiment [98]. This means that a large amount of the SFOEWPT points of CP in the Dark will be able to be tested by future DM direct detection experiments.

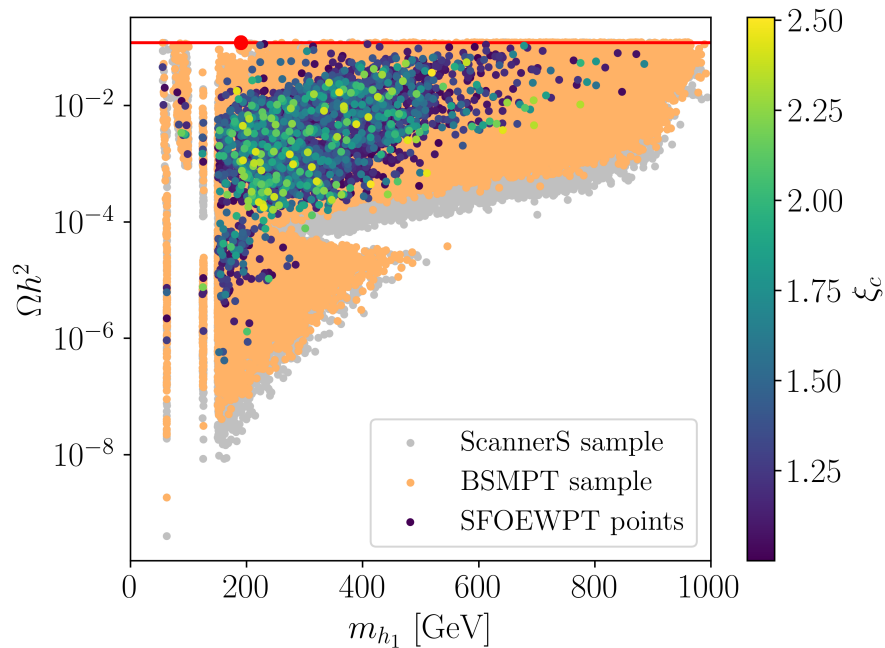


Figure 5.13.: The relic density versus the DM mass m_{h_1} for all points that pass the ScannerS constraints (gray). DM constraints are included. Orange points additionally pass the BSMPT constraints. The colored points indicate SFOEWPT points with strength $\xi_c \gtrsim 1$. Only points with $T_c > T_{EW}$ are considered as viable SFOEWPT points. The experimentally measured relic density $\Omega_{\text{obs}} h^2 = 0.1200 \pm 0.0012$ [4] is shown in red. Points within the 1σ bounds around the central value are additionally colored in red, they are all found to have $m_{h_1} = 190.193$ GeV.

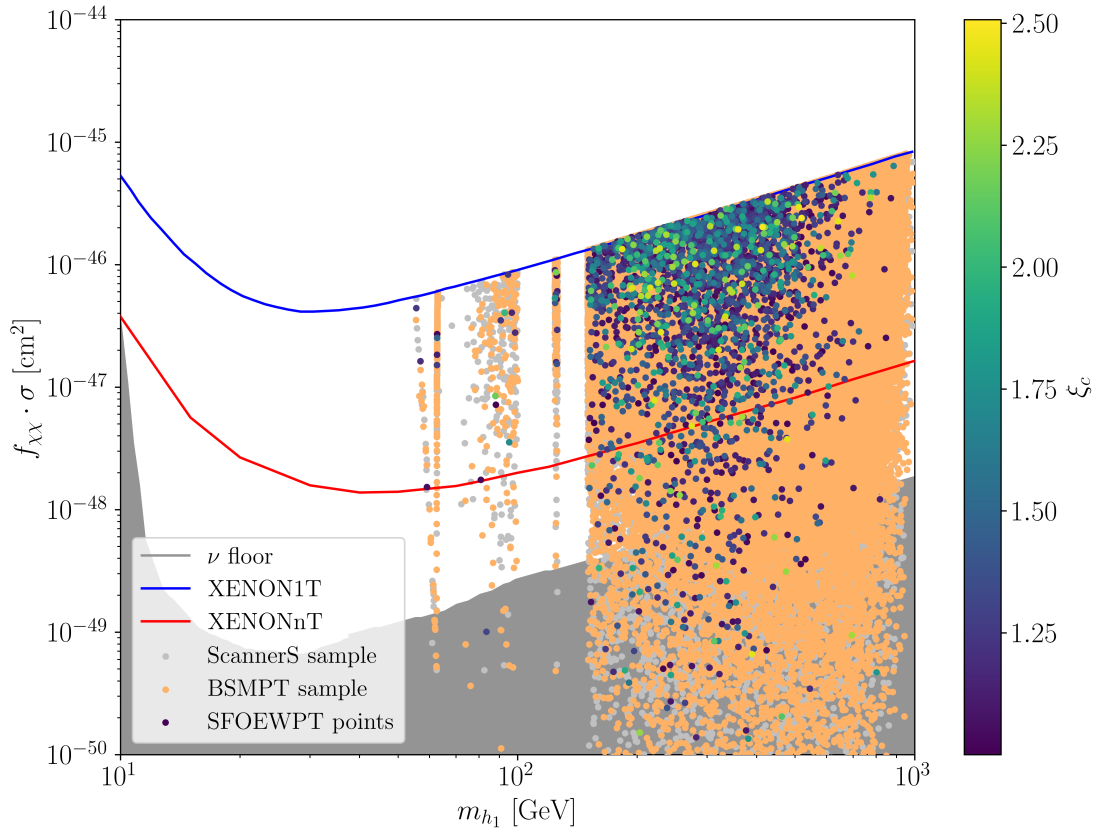


Figure 5.14.: The effective SI direct detection DM-nucleon cross section as a function of the DM mass m_{h_1} for all points of the sample of Tab. 5.3. The color code is the same as in Fig. 5.13. The experimental results have been taken from [99]. The XENON1T exclusion limit [90] is shown in blue. In red, we show the projected sensitivity of the XENONnT experiment [98]. The experimental limit for the neutrino background has been taken from [100].

5.8. Branching Ratios of the SM-like Higgs Boson

In this section we discuss the results for the branching ratios of the SM-like Higgs h into photons and into dark particle pairs. The benchmark point sample that is introduced in Sec. 5.2 and further discussed in Secs. 5.3-5.7 only includes 247 points with $m_{h_1} < 70$ GeV that pass all **ScannerS** and **MicrOMEGAs** constraints (see Sec. 5.1.1). This corresponds to a percentage of 0.15% of the **ScannerS** sample that also passes DM constraints. Only 121 or 49% of these **ScannerS** points that show $m_{h_1} < 70$ GeV pass the **BSMPT** constraints and in total 7 or 2.8% are also **SFOEWPT** points with $T_c > T_{EW}$. A non-zero invisible branching ratio of h is observed to be possible whenever $m_{h_1} < \frac{m_h}{2}$. As we aim to study decays of h into dark particles, we need a substantial amount of viable parameter points in the mass region $m_{h_1} < 70$ GeV. Therefore, we performed an additional dedicated scan with **ScannerS** and **MicrOMEGAs** in this specific mass region. The thus generated benchmark point sample is summarized in Tab. 5.8. Note that the percentages of points that pass the subsequent checks are similar to those of the benchmark point sample of Tab. 5.3, where we scanned in the much broader range of $1 \text{ GeV} < m_{h_1} < 1000 \text{ GeV}$.

In Fig. 5.15 we show the branching ratio of the SM-like Higgs h into two photons normalized to the SM value $\text{BR}^{\text{SM}}(h \rightarrow \gamma\gamma) = 0.00227$ [61] versus the mass of the dark charged scalar m_{H^\pm} . Figure 5.15a illustrates the sample of Sec. 5.2 with $1 \text{ GeV} < m_{h_1} < 1000 \text{ GeV}$. In Fig. 5.15b we *additionally* include the points from the dedicated scan in the region $m_{h_1} < 70$ GeV. Points from the new sample cover the whole scanned m_{H^\pm} -range and even extend the range of the ratio $\frac{\text{BR}(h \rightarrow \gamma\gamma)}{\text{BR}^{\text{SM}}(h \rightarrow \gamma\gamma)}$ that is found for viable **SFOEWPT** points. Figure 5.15a shows for the **SFOEWPT** points of the sample with $1 \text{ GeV} < m_{h_1} < 1000 \text{ GeV}$ that the ratio takes values in the range

$$0.917 < \left. \frac{\text{BR}(h \rightarrow \gamma\gamma)}{\text{BR}^{\text{SM}}(h \rightarrow \gamma\gamma)} \right|_{\xi_c > 1, T_c > T_{EW}} < 1.115. \quad (5.21)$$

When we additionally include the points of the dedicated scan with $m_{h_1} < 70$ GeV, this region is extended to

$$0.843 < \left. \frac{\text{BR}(h \rightarrow \gamma\gamma)}{\text{BR}^{\text{SM}}(h \rightarrow \gamma\gamma)} \right|_{m_{h_1} < 70 \text{ GeV}, \xi_c > 1, T_c > T_{EW}} < 1.179, \quad (5.22)$$

as for $m_{h_1} < \frac{m_h}{2}$ the decay channel $h \rightarrow h_1 h_1$ is open and depending on m_{h_1} also the channels into the other neutral dark bosons h_2 and h_3 are open. This changes the total SM-like Higgs decay width and increases the range of the ratio in Eq. (5.22). This change stays compatible with current Higgs data, as ensured by **ScannerS**.

Figure 5.16 displays the invisible branching ratio of the SM-like Higgs h into dark neutral particles $\text{BR}(h \rightarrow h_i h_j)$, $i, j \in \{1, 2, 3\}$, versus the DM mass m_{h_1} in the range $40 \text{ GeV} < m_{h_1} < 70 \text{ GeV}$ for all points from the samples of Tabs. 5.3 and 5.8. We manually impose an additional cut on $\text{BR}(h \rightarrow \text{inv.}) < 0.11$, following the latest results of [101]. We find viable parameter points and also viable **SFOEWPT** points for all $\text{BR}(h \rightarrow \text{inv.}) < 0.11$. This means that the model CP in the Dark with an **SFOEWPT** can be tested by future improved measurements of $h \rightarrow \text{inv.}$ at LHC. Note that the overdensity of points for $m_{h_1} > 55$ GeV and the underdensity for $m_{h_1} < 55$ GeV is not physical, but merely a scan artifact most likely issuing from this mass region being under-represented in terms of initial parameter points in **ScannerS**.

In Fig. 5.17 we show the invisible branching ratio of h versus the gauge boson signal

ScannerS and MicrOMEGAs	BSMPT	SFOEWPT	$T_c > T_{EW}$
433 437(100%)	225 285(52.0%)	7367(1.7%)	6397(1.5%)

Table 5.8.: Benchmark point sample for a dedicated scan in the DM mass region $m_{h_1} < 70$ GeV with **ScannerS** and **MicrOMEGAs**. For details on the implemented constraints, see Sec. 5.1.1.

strength, derived directly from the **ScannerS** output and defined as, cf. also [96],

$$\mu_{VV} \equiv \frac{\sigma(pp \rightarrow h \rightarrow ZZ)}{\sigma^{\text{SM}}(pp \rightarrow h \rightarrow ZZ)} = \frac{\sigma(pp \rightarrow h \rightarrow W^+W^-)}{\sigma^{\text{SM}}(pp \rightarrow h \rightarrow W^+W^-)}. \quad (5.23)$$

A cut on $\text{BR}(h \rightarrow \text{inv.}) < 0.11$, following the latest results of [101] is again imposed. Our results look similar to those found in [96] for the fully dark phase (FDP) of the N2HDM. The invisible branching ratio $\text{BR}(h \rightarrow \text{inv.})$ decreases for increasing μ_{VV} until $\text{BR}(h \rightarrow \text{inv.}) = 0$ when $\mu_{VV} = 1$. This is expected as for $\mu_{VV} \rightarrow 1$, the SM-like Higgs converges to its SM behavior with no decays into invisible particles being allowed. Furthermore, we find viable SFOEWPT points over the whole range of μ_{VV} and $\text{BR}(h \rightarrow \text{inv.})$.

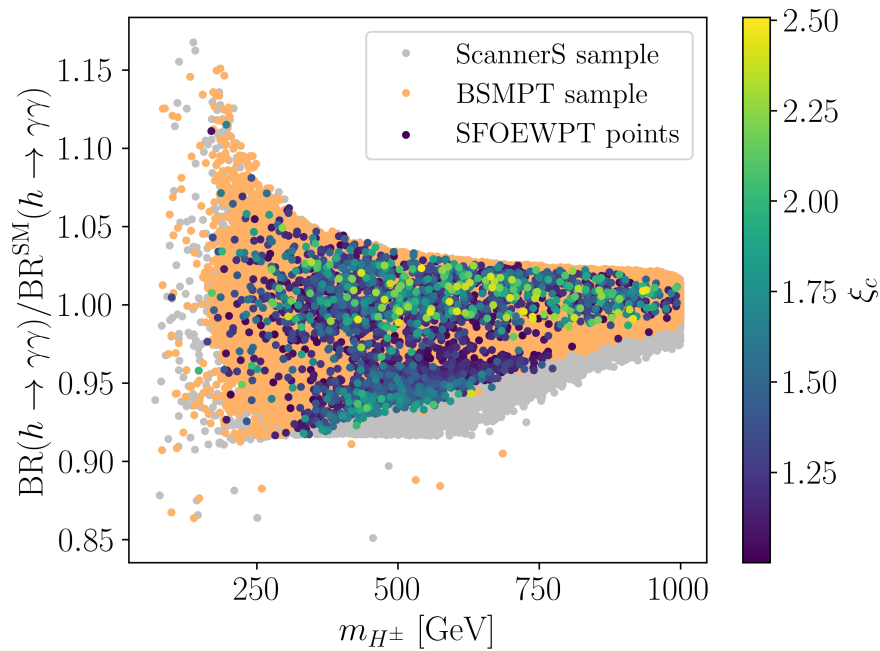
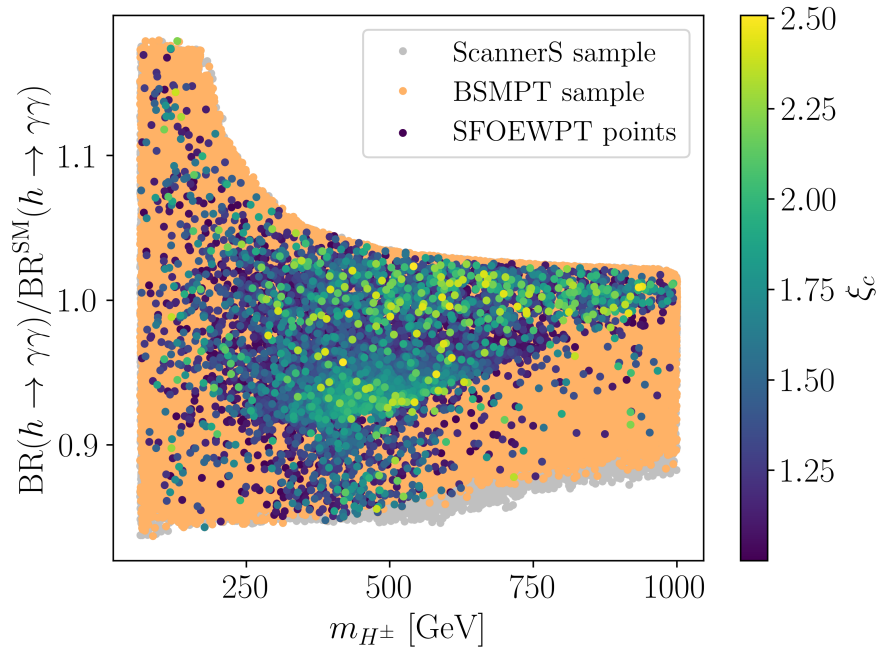
(a) Sample of Sec. 5.2 with $1 \text{ GeV} < m_{h_1} < 1000 \text{ GeV}$ (b) Sample of Fig. 5.15a with additional $m_{h_1} < 70 \text{ GeV}$ sample

Figure 5.15.: Branching ratio of the SM-like Higgs h into photons, $\text{BR}(h \rightarrow \gamma\gamma)$, normalized to the SM value $\text{BR}^{\text{SM}}(h \rightarrow \gamma\gamma) = 0.00227$ [61] versus the charged dark scalar mass m_{H^\pm} . The top figure illustrates the parameter sample that was discussed in Sec. 5.2, in the bottom figure we additionally combine the sample of Sec. 5.2 with a new sample that is generated through a dedicated scan in the mass region $m_{h_1} < 70 \text{ GeV}$. Details on this new sample can be found in Tab. 5.8. Gray points pass all `ScannerS`-tests, including DM constraints, orange points additionally pass all checks of `BSMPT`. A cut on $T_c > T_{\text{EW}}$ for the SFOEWPT points is enforced. The color code indicates the strength of the SFOEWPT $\xi_c \gtrsim 1$.

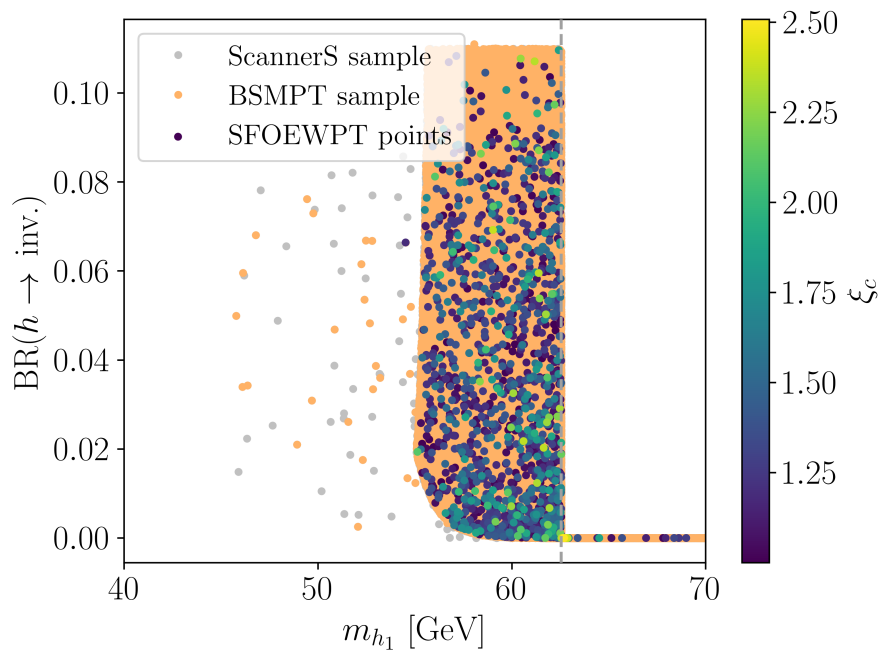


Figure 5.16.: The invisible branching ratio of the SM-like Higgs h into two neutral dark scalars $h_i h_j$, $i, j \in \{1, 2, 3\}$, versus the DM mass m_{h_1} for all points of the sample from Sec. 5.2 combined with the new sample with $m_{h_1} < 70$ GeV, for details see Tab. 5.8. We additionally impose a cut on $\text{BR}(h \rightarrow \text{inv.}) < 0.11$, following the latest results of [101]. Gray points pass all **ScannerS**-tests, including DM constraints, orange points additionally pass all checks of **BSMPT**. A cut on $T_c > T_{\text{EW}}$ for the SFOEWPT points, is enforced. The color code indicates the strength of the SFOEWPT $\xi_c \gtrsim 1$. The vertical line is at $m_{h_1} = \frac{m_h}{2}$.

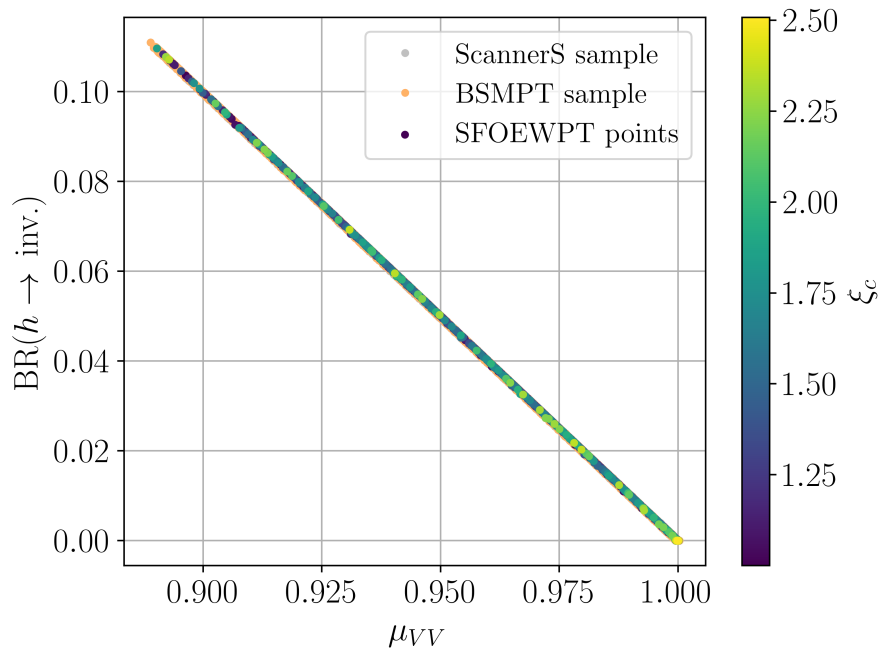


Figure 5.17.: The invisible branching ratio of the SM-like Higgs h , $\text{BR}(h \rightarrow \text{inv.})$, $\text{inv.} \equiv h_i h_j$ with $i, j \in \{1, 2, 3\}$, versus the gauge boson signal strength μ_{VV} , as defined in Eq. (5.23), for the combined sample from Tabs. 5.3 and 5.8. We additionally impose a cut on $\text{BR}(h \rightarrow \text{inv.}) < 0.11$, following the latest results of [101]. Gray points pass all **ScannerS**-tests, including DM constraints, orange points additionally pass all checks of **BSMPT**. A cut on $T_c > T_{\text{EW}}$ for the **SFOEWPT** points is enforced. The color code indicates the strength of the SFOEWPT $\xi_c \gtrsim 1$.

6. Conclusions

In this thesis we studied the possibility of an SFOEWPT within the model CP in the Dark. CP in the Dark features an N2HDM-like extended scalar sector with an SM-like first doublet and a stabilized dark sector consisting of a dark doublet and a dark real singlet. The dark neutral scalars mix and create three mass eigenstates h_i with $i \in \{1, 2, 3\}$ and the mass hierarchy $m_{h_1} < m_{h_2} < m_{h_3}$. The lightest, h_1 , acts as a stable particle dark matter candidate. Explicit CPV in the dark sector is introduced through $\text{Im}(A) \neq 0$.

In Chapter 4 we proposed a renormalization scheme based on the conventional approach of [65, 66, 69–71] that redefines the finite pieces such that the tree-level masses and mixing angles can be used as scan input variables. Our scheme adds an additional term to the counterterm Lagrangian that is able to absorb all non-vanishing contributions of loop-induced CPV interactions. We stated that the conventional approach that is based on a tree-level like structure of the counterterm Lagrangian is insufficient for any model that features non-standard CPV. The reason are loop-induced CPV interactions that can still alter the masses and angles that are extracted from the one-loop corrected effective potential at finite temperature. We also studied in detail the effects of varying the non-constrained finite piece parameters of our renormalization scheme and their physical implications. At the end of the discussion, we concluded to choose a specific scheme for the numerical analysis.

In Chapter 5 we presented our results. As one outcome of this work, we provided the implementation of the model CP in the Dark as a new model class into the C++ code BSMPT [65, 66]. BSMPT determines an SFOEWPT through the global minimization of the one-loop corrected effective potential including daisy resummation of the bosonic masses at finite temperature. For CP in the Dark, we find viable SFOEWPT points over a broad range of dark charged masses m_{H^\pm} and dark neutral masses m_{h_i} with $i \in \{1, 2, 3\}$. We do not find a favored mass region for an SFOEWPT. Imposing DM constraints on our sample significantly reduces the amount of viable SFOEWPT points, but does not impose limits on the distribution in the dark mass parameter space. We furthermore observe viable SFOEWPT points for any CP-even, CP-odd doublet or singlet admixture. A study of the trilinear SM-like Higgs couplings shows large ranges for SM-like Higgs boson couplings to two dark neutral scalars, that provide viable SFOEWPT points. These couplings enter the SM-like Higgs decays into a dark particle pair and are hence important for LHC searches for DM. Besides that, we predict viable SFOEWPT points in a range that allows for vanishing, SM-like and enhanced values of the one-loop trilinear self-coupling of the SM-like Higgs boson.

The detailed analysis of the minimizing VEV configurations at the EWPT in Sec. 5.3 reveals a most promising feature of the model. We observe that 1.5% of the found viable SFOEWPT points have non-zero dark VEVs minimizing the one-loop effective potential at

$T = T_c$. In particular, we find a non-zero dark CP -violating VEV $\bar{\omega}_{CP} \neq 0$ for these 38 points. In addition to explicit CPV in case $\text{Im}(A) \neq 0$, these points show that CP in the Dark enables the generation of spontaneous CPV at finite temperature.

A study of DM observables in Sec. 5.7 shows theoretically and experimentally viable points that lie within the 1σ bounds of the measured relic density. All found SFOEWPT points are underabundant, but cover a broad range of DM masses and are observed to cover five orders of magnitude in the relic density value. The calculation of the effective SI direct detection DM-nucleon cross section shows that the majority of found SFOEWPT points lies above the neutrino floor and moreover within the experimental reach of the future XENONnT experiment.

Also, the low DM-mass region $m_{h_1} < 70$ GeV is found to provide viable SFOEWPT points over the whole range of the theoretically and experimentally allowed parameter space and with $\text{BR}(h \rightarrow \text{inv.}) < 0.11$ as imposed, below the current experimental bound on the invisible branching ratio of the SM-like Higgs. Future improved measurements of $h \rightarrow \text{inv.}$ at the LHC will be able to test this parameter space region of CP in the Dark.

In summary, we stress that CP in the Dark proved itself to be a very promising extended scalar sector model in the context of a possible explanation of the BAU through EWBG. A large part of the parameter space compatible with theoretical and experimental constraints is covered by viable SFOEWPT points, that are even within reach of future experiments. In addition, not only explicit CPV, but also spontaneous CPV at finite temperature is possible in the framework of the model. Providing an SFOEWPT and additional non-standard spontaneous CPV at finite temperature, CP in the Dark seems promising in an EWBG scenario. The next step to be taken now is to find a detailed answer to the question whether CP in the Dark is actually able to generate the BAU in an EWBG context.

Bibliography

- [1] ATLAS, Georges Aad et al. “Observation of a new particle in the search for the Standard Model Higgs boson with the ATLAS detector at the LHC”. In: *Phys. Lett. B* 716 (2012), pp. 1–29. DOI: 10.1016/j.physletb.2012.08.020. arXiv: 1207.7214 [hep-ex].
- [2] CMS, Serguei Chatrchyan et al. “Observation of a New Boson at a Mass of 125 GeV with the CMS Experiment at the LHC”. In: *Phys. Lett. B* 716 (2012), pp. 30–61. DOI: 10.1016/j.physletb.2012.08.021. arXiv: 1207.7235 [hep-ex].
- [3] Muon $g - 2$ Collaboration, B. Abi et al. “Measurement of the Positive Muon Anomalous Magnetic Moment to 0.46 ppm”. In: *Phys. Rev. Lett.* 126 (14 Apr. 2021), p. 141801. DOI: 10.1103/PhysRevLett.126.141801. URL: <https://link.aps.org/doi/10.1103/PhysRevLett.126.141801>.
- [4] Planck, N. Aghanim et al. “Planck 2018 results. VI. Cosmological parameters”. In: *Astron. Astrophys.* 641 (2020), A6. DOI: 10.1051/0004-6361/201833910. arXiv: 1807.06209 [astro-ph.CO].
- [5] F. Zwicky. “On the Masses of Nebulae and of Clusters of Nebulae”. In: *Astrophys. J.* 86 (1937), pp. 217–246. DOI: 10.1086/143864.
- [6] Vera C. Rubin and W. Kent Ford Jr. “Rotation of the Andromeda Nebula from a Spectroscopic Survey of Emission Regions”. In: *Astrophys. J.* 159 (1970), pp. 379–403. DOI: 10.1086/150317.
- [7] Marc Davis, George Efstathiou, Carlos S. Frenk, and Simon D. M. White. “The Evolution of Large Scale Structure in a Universe Dominated by Cold Dark Matter”. In: *Astrophys. J.* 292 (1985). Ed. by M. A. Srednicki, pp. 371–394. DOI: 10.1086/163168.
- [8] A. D. Sakharov. “Violation of CP Invariance, C asymmetry, and baryon asymmetry of the universe”. In: *Pisma Zh. Eksp. Teor. Fiz.* 5 (1967), pp. 32–35. DOI: 10.1070/PU1991v034n05ABEH002497.
- [9] Particle Data Group, P.A. Zyla et al. “Review of Particle Physics”. In: *PTEP* 2020.8 (2020), p. 083C01. DOI: 10.1093/ptep/ptaa104.
- [10] K. Kajantie, M. Laine, K. Rummukainen, and Mikhail E. Shaposhnikov. “Is there a hot electroweak phase transition at $m(H)$ larger or equal to $m(W)$?” In: *Phys. Rev. Lett.* 77 (1996), pp. 2887–2890. DOI: 10.1103/PhysRevLett.77.2887. arXiv: hep-ph/9605288.
- [11] F. Csikor, Z. Fodor, and J. Heitger. “Endpoint of the hot electroweak phase transition”. In: *Phys. Rev. Lett.* 82 (1999), pp. 21–24. DOI: 10.1103/PhysRevLett.82.21. arXiv: hep-ph/9809291.
- [12] James M. Cline. “Baryogenesis”. In: *Les Houches Summer School - Session 86: Particle Physics and Cosmology: The Fabric of Spacetime*. Sept. 2006. arXiv: hep-ph/0609145.

-
- [13] David E. Morrissey and Michael J. Ramsey-Musolf. “Electroweak baryogenesis”. In: *New J. Phys.* 14 (2012), p. 125003. DOI: 10.1088/1367-2630/14/12/125003. arXiv: 1206.2942 [hep-ph].
- [14] Duarte Azevedo, Pedro M. Ferreira, M. Margarete Muhlleitner, Shruti Patel, Rui Santos, and Jonas Wittbrodt. “CP in the dark”. In: *JHEP* 11 (2018), p. 091. DOI: 10.1007/JHEP11(2018)091. arXiv: 1807.10322 [hep-ph].
- [15] Chien-Yi Chen, Michael Freid, and Marc Sher. “Next-to-minimal two Higgs doublet model”. In: *Phys. Rev. D* 89.7 (2014), p. 075009. DOI: 10.1103/PhysRevD.89.075009. arXiv: 1312.3949 [hep-ph].
- [16] Margarete Muhlleitner, Marco O. P. Sampaio, Rui Santos, and Jonas Wittbrodt. “The N2HDM under Theoretical and Experimental Scrutiny”. In: *JHEP* 03 (2017), p. 094. DOI: 10.1007/JHEP03(2017)094. arXiv: 1612.01309 [hep-ph].
- [17] P. M. Ferreira, Margarete Mühlleitner, Rui Santos, Georg Weiglein, and Jonas Wittbrodt. “Vacuum Instabilities in the N2HDM”. In: *JHEP* 09 (2019), p. 006. DOI: 10.1007/JHEP09(2019)006. arXiv: 1905.10234 [hep-ph].
- [18] Michael E. Peskin and Daniel V. Schroeder. *An Introduction to quantum field theory*. Reading, USA: Addison-Wesley, 1995. ISBN: 978-0-201-50397-5.
- [19] KATRIN Collaboration, M. Aker et al. “Improved Upper Limit on the Neutrino Mass from a Direct Kinematic Method by KATRIN”. In: *Phys. Rev. Lett.* 123 (22 Nov. 2019), p. 221802. DOI: 10.1103/PhysRevLett.123.221802. URL: <https://link.aps.org/doi/10.1103/PhysRevLett.123.221802>.
- [20] F. Englert and R. Brout. “Broken Symmetry and the Mass of Gauge Vector Mesons”. In: *Phys. Rev. Lett.* 13 (1964). Ed. by J. C. Taylor, pp. 321–323. DOI: 10.1103/PhysRevLett.13.321.
- [21] Peter W. Higgs. “Broken symmetries, massless particles and gauge fields”. In: *Phys. Lett.* 12 (1964), pp. 132–133. DOI: 10.1016/0031-9163(64)91136-9.
- [22] Peter W. Higgs. “Broken Symmetries and the Masses of Gauge Bosons”. In: *Phys. Rev. Lett.* 13 (1964). Ed. by J. C. Taylor, pp. 508–509. DOI: 10.1103/PhysRevLett.13.508.
- [23] G. S. Guralnik, C. R. Hagen, and T. W. B. Kibble. “Global Conservation Laws and Massless Particles”. In: *Phys. Rev. Lett.* 13 (1964). Ed. by J. C. Taylor, pp. 585–587. DOI: 10.1103/PhysRevLett.13.585.
- [24] F. Zwicky. “Die Rotverschiebung von extragalaktischen Nebeln”. In: *Helv. Phys. Acta* 6 (1933), pp. 110–127. DOI: 10.1007/s10714-008-0707-4.
- [25] *SDSS Sloan Digital Sky Survey*. <https://www.sdss.org/>. Accessed: 2021-07-31.
- [26] Werner Bernreuther. “CP violation and baryogenesis”. In: *Lect. Notes Phys.* 591 (2002), pp. 237–293. arXiv: hep-ph/0205279.
- [27] Makoto Kobayashi and Toshihide Maskawa. “CP Violation in the Renormalizable Theory of Weak Interaction”. In: *Prog. Theor. Phys.* 49 (1973), pp. 652–657. DOI: 10.1143/PTP.49.652.
- [28] G. ’t Hooft. “Symmetry Breaking through Bell-Jackiw Anomalies”. In: *Phys. Rev. Lett.* 37 (1 July 1976), pp. 8–11. DOI: 10.1103/PhysRevLett.37.8. URL: <https://link.aps.org/doi/10.1103/PhysRevLett.37.8>.
- [29] G. ’t Hooft. “Computation of the quantum effects due to a four-dimensional pseudoparticle”. In: *Phys. Rev. D* 14 (12 Dec. 1976), pp. 3432–3450. DOI: 10.1103/PhysRevD.14.3432. URL: <https://link.aps.org/doi/10.1103/PhysRevD.14.3432>.

- [30] N. S. Manton. “Topology in the Weinberg-Salam Theory”. In: *Phys. Rev. D* 28 (1983), p. 2019. DOI: 10.1103/PhysRevD.28.2019.
- [31] Frans R. Klinkhamer and N. S. Manton. “A Saddle Point Solution in the Weinberg-Salam Theory”. In: *Phys. Rev. D* 30 (1984), p. 2212. DOI: 10.1103/PhysRevD.30.2212.
- [32] V.A. Rubakov and D.S. Gorbunov. *Introduction To The Theory Of The Early Universe: Hot Big Bang Theory*. World Scientific Publishing Company, 2011. ISBN: 9789814390620. URL: <https://books.google.de/books?id=kJrFCgAAQBAJ>.
- [33] D. A. Kirzhnits. “Weinberg model in the hot universe”. In: *JETP Lett.* 15 (1972), pp. 529–531.
- [34] D. A. Kirzhnits and Andrei D. Linde. “Macroscopic Consequences of the Weinberg Model”. In: *Phys. Lett. B* 42 (1972), pp. 471–474. DOI: 10.1016/0370-2693(72)90109-8.
- [35] D. A. Kirzhnits and Andrei D. Linde. “A Relativistic phase transition”. In: *Zh. Eksp. Teor. Fiz.* 67 (1974), pp. 1263–1275.
- [36] L. Dolan and R. Jackiw. “Symmetry behavior at finite temperature”. In: *Phys. Rev. D* 9 (12 June 1974), pp. 3320–3341. DOI: 10.1103/PhysRevD.9.3320. URL: <https://link.aps.org/doi/10.1103/PhysRevD.9.3320>.
- [37] Steven Weinberg. “Gauge and Global Symmetries at High Temperature”. In: *Phys. Rev. D* 9 (1974), pp. 3357–3378. DOI: 10.1103/PhysRevD.9.3357.
- [38] Robert D. Pisarski and Frank Wilczek. “Remarks on the chiral phase transition in chromodynamics”. In: *Phys. Rev. D* 29 (2 Jan. 1984), pp. 338–341. DOI: 10.1103/PhysRevD.29.338. URL: <https://link.aps.org/doi/10.1103/PhysRevD.29.338>.
- [39] Hiren H. Patel and Michael J. Ramsey-Musolf. “Baryon Washout, Electroweak Phase Transition, and Perturbation Theory”. In: *JHEP* 07 (2011), p. 029. DOI: 10.1007/JHEP07(2011)029. arXiv: 1101.4665 [hep-ph].
- [40] M. B. Gavela, P. Hernandez, J. Orloff, and O. Pene. “Standard model CP violation and baryon asymmetry”. In: *Mod. Phys. Lett. A* 9 (1994), pp. 795–810. DOI: 10.1142/S0217732394000629. arXiv: hep-ph/9312215.
- [41] Sidney Coleman and Erick Weinberg. “Radiative Corrections as the Origin of Spontaneous Symmetry Breaking”. In: *Phys. Rev. D* 7 (6 Mar. 1973), pp. 1888–1910. DOI: 10.1103/PhysRevD.7.1888. URL: <https://link.aps.org/doi/10.1103/PhysRevD.7.1888>.
- [42] Giuseppe Degrandi, Stefano Di Vita, Joan Elias-Miro, Jose R. Espinosa, Gian F. Giudice, Gino Isidori, and Alessandro Strumia. “Higgs mass and vacuum stability in the Standard Model at NNLO”. In: *JHEP* 08 (2012), p. 098. DOI: 10.1007/JHEP08(2012)098. arXiv: 1205.6497 [hep-ph].
- [43] A. V. Bednyakov, B. A. Kniehl, A. F. Pikelner, and O. L. Veretin. “Stability of the Electroweak Vacuum: Gauge Independence and Advanced Precision”. In: *Phys. Rev. Lett.* 115.20 (2015), p. 201802. DOI: 10.1103/PhysRevLett.115.201802. arXiv: 1507.08833 [hep-ph].
- [44] P. M. Ferreira, R. Santos, and A. Barroso. “Stability of the tree-level vacuum in two Higgs doublet models against charge or CP spontaneous violation”. In: *Phys. Lett. B* 603 (2004). [Erratum: *Phys.Lett.B* 629, 114–114 (2005)], pp. 219–229. DOI: 10.1016/j.physletb.2004.10.022. arXiv: hep-ph/0406231.

- [45] A. Barroso, P. M. Ferreira, and R. Santos. “Charge and CP symmetry breaking in two Higgs doublet models”. In: *Phys. Lett. B* 632 (2006), pp. 684–687. DOI: 10.1016/j.physletb.2005.11.031. arXiv: hep-ph/0507224.
- [46] I. P. Ivanov. “Minkowski space structure of the Higgs potential in 2HDM”. In: *Phys. Rev. D* 75 (2007). [Erratum: Phys.Rev.D 76, 039902 (2007)], p. 035001. DOI: 10.1103/PhysRevD.75.035001. arXiv: hep-ph/0609018.
- [47] Igor P. Ivanov. “Minkowski space structure of the Higgs potential in 2HDM. II. Minima, symmetries, and topology”. In: *Phys. Rev. D* 77 (2008), p. 015017. DOI: 10.1103/PhysRevD.77.015017. arXiv: 0710.3490 [hep-ph].
- [48] Erick J. Weinberg. “Radiative corrections as the origin of spontaneous symmetry breaking”. PhD thesis. Harvard U., 1973. arXiv: hep-th/0507214.
- [49] Takeo Matsubara. “A New Approach to Quantum-Statistical Mechanics”. In: *Progress of Theoretical Physics* 14.4 (Oct. 1955), pp. 351–378. ISSN: 0033-068X. DOI: 10.1143/PTP.14.351. eprint: <https://academic.oup.com/ptp/article-pdf/14/4/351/5286981/14-4-351.pdf>. URL: <https://doi.org/10.1143/PTP.14.351>.
- [50] Ashok Das. *Finite Temperature Field Theory*. WORLD SCIENTIFIC, 1997. DOI: 10.1142/3277. eprint: <https://www.worldscientific.com/doi/pdf/10.1142/3277>. URL: <https://www.worldscientific.com/doi/abs/10.1142/3277>.
- [51] Marc Sher. “Electroweak Higgs Potentials and Vacuum Stability”. In: *Phys. Rept.* 179 (1989), pp. 273–418. DOI: 10.1016/0370-1573(89)90061-6.
- [52] M. Quiros. “Field theory at finite temperature and phase transitions”. In: *Helv. Phys. Acta* 67 (1994), pp. 451–583.
- [53] Mariano Quiros. “Finite temperature field theory and phase transitions”. In: *ICTP Summer School in High-Energy Physics and Cosmology*. Jan. 1999. arXiv: hep-ph/9901312.
- [54] José Eliel Camargo-Molina, António P. Morais, Roman Pasechnik, Marco O. P. Sampaio, and Jonas Wessén. “All one-loop scalar vertices in the effective potential approach”. In: *JHEP* 08 (2016), p. 073. DOI: 10.1007/JHEP08(2016)073. arXiv: 1606.07069 [hep-ph].
- [55] M. E. Carrington. “Effective potential at finite temperature in the standard model”. In: *Phys. Rev. D* 45 (8 Apr. 1992), pp. 2933–2944. DOI: 10.1103/PhysRevD.45.2933. URL: <https://link.aps.org/doi/10.1103/PhysRevD.45.2933>.
- [56] Peter Brockway Arnold. “Phase transition temperatures at next-to-leading order”. In: *Phys. Rev. D* 46 (1992), pp. 2628–2635. DOI: 10.1103/PhysRevD.46.2628. arXiv: hep-ph/9204228.
- [57] J.I. Kapusta. *Finite-Temperature Field Theory*. Cambridge Monographs on Mathematical Physics. Cambridge University Press, 1993. ISBN: 9780521449458.
- [58] Peter Brockway Arnold and Olivier Espinosa. “The Effective potential and first order phase transitions: Beyond leading-order”. In: *Phys. Rev. D* 47 (1993). [Erratum: Phys.Rev.D 50, 6662 (1994)], p. 3546. DOI: 10.1103/PhysRevD.47.3546. arXiv: hep-ph/9212235.
- [59] Rajesh R. Parwani. “Resummation in a hot scalar field theory”. In: *Phys. Rev. D* 45 (1992). [Erratum: Phys.Rev.D 48, 5965 (1993)], p. 4695. DOI: 10.1103/PhysRevD.45.4695. arXiv: hep-ph/9204216.
- [60] John F. Gunion, Howard E. Haber, Gordon L. Kane, and Sally Dawson. *The Higgs Hunter’s Guide*. Vol. 80. 2000.

- [61] Particle Data Group, M. Tanabashi et al. “Review of Particle Physics”. In: *Phys. Rev. D* 98.3 (2018), p. 030001. DOI: 10.1103/PhysRevD.98.030001.
- [62] A. Cordero-Cid, J. Hernández-Sánchez, V. Keus, S. F. King, S. Moretti, D. Rojas, and D. Sokolowska. “CP violating scalar Dark Matter”. In: *JHEP* 12 (2016), p. 014. DOI: 10.1007/JHEP12(2016)014. arXiv: 1608.01673 [hep-ph].
- [63] Dorota Sokolowska. “Dark Matter and CP-violation in the Three-Higgs Doublet Model”. In: *J. Phys. Conf. Ser.* 873.1 (2017), p. 012030. DOI: 10.1088/1742-6596/873/1/012030.
- [64] Marcel Krause, David Lopez-Val, Margarete Muhlleitner, and Rui Santos. “Gauge-independent Renormalization of the N2HDM”. In: *JHEP* 12 (2017), p. 077. DOI: 10.1007/JHEP12(2017)077. arXiv: 1708.01578 [hep-ph].
- [65] Philipp Basler and Margarete Mühlleitner. “BSMPT (Beyond the Standard Model Phase Transitions): A tool for the electroweak phase transition in extended Higgs sectors”. In: *Comput. Phys. Commun.* 237 (2019), pp. 62–85. DOI: 10.1016/j.cpc.2018.11.006. arXiv: 1803.02846 [hep-ph].
- [66] P. Basler, M. Muhlleitner, and J. Müller. “BSMPT v2 A Tool for the Electroweak Phase Transition and the Baryon Asymmetry of the Universe in Extended Higgs Sectors”. In: (July 2020). arXiv: 2007.01725 [hep-ph].
- [67] Carroll Wainwright, Stefano Profumo, and Michael J. Ramsey-Musolf. “Gravity waves from a cosmological phase transition: Gauge artifacts and daisy resummations”. In: *Phys. Rev. D* 84 (2 July 2011), p. 023521. DOI: 10.1103/PhysRevD.84.023521. URL: <https://link.aps.org/doi/10.1103/PhysRevD.84.023521>.
- [68] Mathias Garny and Thomas Konstandin. “On the gauge dependence of vacuum transitions at finite temperature”. In: *JHEP* 07 (2012), p. 189. DOI: 10.1007/JHEP07(2012)189. arXiv: 1205.3392 [hep-ph].
- [69] P. Basler, M. Krause, M. Muhlleitner, J. Wittbrodt, and A. Wlotzka. “Strong First Order Electroweak Phase Transition in the CP-Conserving 2HDM Revisited”. In: *JHEP* 02 (2017), p. 121. DOI: 10.1007/JHEP02(2017)121. arXiv: 1612.04086 [hep-ph].
- [70] Philipp Basler, Margarete Mühlleitner, and Jonas Wittbrodt. “The CP-Violating 2HDM in Light of a Strong First Order Electroweak Phase Transition and Implications for Higgs Pair Production”. In: *JHEP* 03 (2018), p. 061. DOI: 10.1007/JHEP03(2018)061. arXiv: 1711.04097 [hep-ph].
- [71] Philipp Basler, Margarete Mühlleitner, and Jonas Müller. “Electroweak Phase Transition in Non-Minimal Higgs Sectors”. In: *JHEP* 05 (2020), p. 016. DOI: 10.1007/JHEP05(2020)016. arXiv: 1912.10477 [hep-ph].
- [72] Lukas Altenkamp, Stefan Dittmaier, and Heidi Rzehak. “Precision calculations for $h \rightarrow WW/ZZ \rightarrow 4$ fermions in the Two-Higgs-Doublet Model with Prophecy4f”. In: *JHEP* 03 (2018), p. 110. DOI: 10.1007/JHEP03(2018)110. arXiv: 1710.07598 [hep-ph].
- [73] Lukas Altenkamp, Michele Boggia, Stefan Dittmaier, and Heidi Rzehak. “Electroweak corrections in the Two-Higgs-Doublet Model and Singlet Extension of the Standard Model”. In: *PoS LL2018* (2018), p. 011. DOI: 10.22323/1.303.0011. arXiv: 1807.05876 [hep-ph].
- [74] Marcel Krause, Margarete Mühlleitner, and Michael Spira. “2HDECAY — A program for the calculation of electroweak one-loop corrections to Higgs decays in the Two-Higgs-Doublet Model including state-of-the-art QCD corrections”. In: *Comput. Phys. Commun.* 246 (2020), p. 106852. DOI: 10.1016/j.cpc.2019.08.003. arXiv: 1810.00768 [hep-ph].

-
- [75] Rita Coimbra, Marco O. P. Sampaio, and Rui Santos. “ScannerS: Constraining the phase diagram of a complex scalar singlet at the LHC”. In: *Eur. Phys. J. C* 73 (2013), p. 2428. DOI: 10.1140/epjc/s10052-013-2428-4. arXiv: 1301.2599 [hep-ph].
- [76] Margarete Mühlleitner, Marco O. P. Sampaio, Rui Santos, and Jonas Wittbrodt. “ScannerS: Parameter Scans in Extended Scalar Sectors”. In: (July 2020). arXiv: 2007.02985 [hep-ph].
- [77] Michael E. Peskin and Tatsu Takeuchi. “Estimation of oblique electroweak corrections”. In: *Phys. Rev. D* 46 (1992), pp. 381–409. DOI: 10.1103/PhysRevD.46.381.
- [78] Johannes Haller, Andreas Hoecker, Roman Kogler, Klaus Mönig, Thomas Peiffer, and Jörg Stelzer. “Update of the global electroweak fit and constraints on two-Higgs-doublet models”. In: *Eur. Phys. J. C* 78.8 (2018), p. 675. DOI: 10.1140/epjc/s10052-018-6131-3. arXiv: 1803.01853 [hep-ph].
- [79] Philip Bechtle, Oliver Brein, Sven Heinemeyer, Georg Weiglein, and Karina E. Williams. “HiggsBounds: Confronting Arbitrary Higgs Sectors with Exclusion Bounds from LEP and the Tevatron”. In: *Comput. Phys. Commun.* 181 (2010), pp. 138–167. DOI: 10.1016/j.cpc.2009.09.003. arXiv: 0811.4169 [hep-ph].
- [80] Philip Bechtle, Oliver Brein, Sven Heinemeyer, Georg Weiglein, and Karina E. Williams. “HiggsBounds 2.0.0: Confronting Neutral and Charged Higgs Sector Predictions with Exclusion Bounds from LEP and the Tevatron”. In: *Comput. Phys. Commun.* 182 (2011), pp. 2605–2631. DOI: 10.1016/j.cpc.2011.07.015. arXiv: 1102.1898 [hep-ph].
- [81] Philip Bechtle, Oliver Brein, Sven Heinemeyer, Oscar Stal, Tim Stefaniak, Georg Weiglein, and Karina Williams. “Recent Developments in HiggsBounds and a Preview of HiggsSignals”. In: *PoS CHARGED2012* (2012). Ed. by Rikard Enberg and Arnaud Ferrari, p. 024. DOI: 10.22323/1.156.0024. arXiv: 1301.2345 [hep-ph].
- [82] Philip Bechtle, Oliver Brein, Sven Heinemeyer, Oscar Stål, Tim Stefaniak, Georg Weiglein, and Karina E. Williams. “HiggsBounds – 4: Improved Tests of Extended Higgs Sectors against Exclusion Bounds from LEP, the Tevatron and the LHC”. In: *Eur. Phys. J. C* 74.3 (2014), p. 2693. DOI: 10.1140/epjc/s10052-013-2693-2. arXiv: 1311.0055 [hep-ph].
- [83] Philip Bechtle, Sven Heinemeyer, Oscar Stal, Tim Stefaniak, and Georg Weiglein. “Applying Exclusion Likelihoods from LHC Searches to Extended Higgs Sectors”. In: *Eur. Phys. J. C* 75.9 (2015), p. 421. DOI: 10.1140/epjc/s10052-015-3650-z. arXiv: 1507.06706 [hep-ph].
- [84] Philip Bechtle, Sven Heinemeyer, Oscar Stål, Tim Stefaniak, and Georg Weiglein. “HiggsSignals: Confronting arbitrary Higgs sectors with measurements at the Tevatron and the LHC”. In: *Eur. Phys. J. C* 74.2 (2014), p. 2711. DOI: 10.1140/epjc/s10052-013-2711-4. arXiv: 1305.1933 [hep-ph].
- [85] Philip Bechtle, Sven Heinemeyer, Oscar Stål, Tim Stefaniak, and Georg Weiglein. “Probing the Standard Model with Higgs signal rates from the Tevatron, the LHC and a future ILC”. In: *JHEP* 11 (2014), p. 039. DOI: 10.1007/JHEP11(2014)039. arXiv: 1403.1582 [hep-ph].
- [86] ACME, Jacob Baron et al. “Order of Magnitude Smaller Limit on the Electric Dipole Moment of the Electron”. In: *Science* 343 (2014), pp. 269–272. DOI: 10.1126/science.1248213. arXiv: 1310.7534 [physics.atom-ph].
- [87] G. Belanger, F. Boudjema, A. Pukhov, and A. Semenov. “micrOMEGAs: A Tool for dark matter studies”. In: *Nuovo Cim. C* 033N2 (2010), pp. 111–116. DOI: 10.1393/ncc/i2010-10591-3. arXiv: 1005.4133 [hep-ph].

- [88] Geneviève Bélanger, Fawzi Boudjema, Andreas Goudelis, Alexander Pukhov, and Bryan Zaldivar. “micrOMEGAs5.0 : Freeze-in”. In: *Comput. Phys. Commun.* 231 (2018), pp. 173–186. DOI: 10.1016/j.cpc.2018.04.027. arXiv: 1801.03509 [hep-ph].
- [89] *MicrOMEGAs*. <https://lapth.cnrs.fr/micromegas/>. Accessed: 2021-07-31.
- [90] XENON, E. Aprile et al. “Dark Matter Search Results from a One Ton-Year Exposure of XENON1T”. In: *Phys. Rev. Lett.* 121.11 (2018), p. 111302. DOI: 10.1103/PhysRevLett.121.111302. arXiv: 1805.12562 [astro-ph.CO].
- [91] Mark C. Galassi, Jim Davies, James Theiler, Brian Gough, Gerard Jungman, Patrick Alken, Michael Booth, Fabrice Rossi, and Rhys Ulerich. *GNU Scientific Library*. Network Theory, Ltd., Aug. 2019. URL: <https://www.gnu.org/software/gsl/>.
- [92] *libcmaes*. Accessed: 2021-07-31. URL: <https://github.com/CMA-ES/libcmaes>.
- [93] Steven G. Johnson. *The NLOpt nonlinear-optimization package*. Accessed: 2021-07-31. URL: <http://github.com/stevengj/nlopt>.
- [94] Philipp Basler. “Vacuum Structure of Models beyond the Standard Model”. PhD thesis. KIT, Karlsruhe, 2019. DOI: 10.5445/IR/1000104124.
- [95] Shinya Kanemura, Shingo Kiyoura, Yasuhiro Okada, Eibun Senaha, and C. P. Yuan. “New physics effect on the Higgs selfcoupling”. In: *Phys. Lett. B* 558 (2003), pp. 157–164. DOI: 10.1016/S0370-2693(03)00268-5. arXiv: hep-ph/0211308.
- [96] Isabell Engeln, Pedro Ferreira, M. Margarete Mühlleitner, Rui Santos, and Jonas Wittbrodt. “The Dark Phases of the N2HDM”. In: *JHEP* 08 (2020), p. 085. DOI: 10.1007/JHEP08(2020)085. arXiv: 2004.05382 [hep-ph].
- [97] Seraina Glaus, Margarete Mühlleitner, Jonas Müller, Shruti Patel, Tizian Römer, and Rui Santos. “Electroweak Corrections in a Pseudo-Nambu Goldstone Dark Matter Model Revisited”. In: *JHEP* 12 (2020), p. 034. DOI: 10.1007/JHEP12(2020)034. arXiv: 2008.12985 [hep-ph].
- [98] XENON, E. Aprile et al. “Projected WIMP sensitivity of the XENONnT dark matter experiment”. In: *JCAP* 11 (2020), p. 031. DOI: 10.1088/1475-7516/2020/11/031. arXiv: 2007.08796 [physics.ins-det].
- [99] A. Desai and A. Moskowitz. *DMTTOOLS, Dark Matter Limit Plot Generator*. Accessed: 2021-07-31. URL: <http://dmttools.brown.edu/>.
- [100] J. Billard, L. Strigari, and E. Figueroa-Feliciano. “Implication of neutrino backgrounds on the reach of next generation dark matter direct detection experiments”. In: *Phys. Rev. D* 89.2 (2014), p. 023524. DOI: 10.1103/PhysRevD.89.023524. arXiv: 1307.5458 [hep-ph].
- [101] “Combination of searches for invisible Higgs boson decays with the ATLAS experiment”. In: (Oct. 2020).
- [102] Stephen P. Martin. “Taming the Goldstone contributions to the effective potential”. In: *Phys. Rev. D* 90 (1 July 2014), p. 016013. DOI: 10.1103/PhysRevD.90.016013. URL: <https://link.aps.org/doi/10.1103/PhysRevD.90.016013>.
- [103] J. Elias-Miro, J. R. Espinosa, and T. Konstandin. “Taming Infrared Divergences in the Effective Potential”. In: *JHEP* 08 (2014), p. 034. DOI: 10.1007/JHEP08(2014)034. arXiv: 1406.2652 [hep-ph].
- [104] Marcel Krause, Robin Lorenz, Margarete Muhlleitner, Rui Santos, and Hanna Ziesche. “Gauge-independent Renormalization of the 2-Higgs-Doublet Model”. In: *Journal of High Energy Physics* 2016 (May 2016). DOI: 10.1007/JHEP09(2016)143.

- [105] Marcel Krause, Margarete Muhlleitner, Rui Santos, and Hanna Ziesche. “Higgs-to-Higgs boson decays in a 2HDM at next-to-leading order”. In: *Phys. Rev. D* 95.7 (2017), p. 075019. DOI: 10.1103/PhysRevD.95.075019. arXiv: 1609.04185 [hep-ph].

Acknowledgements

I would like to express my most sincere gratitude to Prof. Dr. Milada Margarete Mühlleitner for providing me the opportunity to work on such a fascinating and inspiring topic. Through her supervision I was honored to be introduced into the vast and exciting field of theoretical particle physics. Innumerable fruitful discussions and feedback at any stages of this work was especially valuable and made this year not only a positively challenging, but also rewarding experience. Thanks as well for enabling my participation in several conferences and workshops, which all were particularly interesting and encouraging.

Thanks a lot to PD Dr. Stefan Gieseke for agreeing on the position of second reviewer.

I would also like to thank Dr. Jonas Müller for guiding me through an exciting year and introducing me to the field of finite temperature field theories and to BSMPT. Thanks for constantly providing ideas and further impulses that eminently promoted this project. Thanks a lot for giving always competent answers to numerous questions, for cross-checking my results and providing detailed feedback on the written form of this thesis.

Thanks to M.Sc. Thanh Tien Dat Nguyen for joining not only my thesis project, but also the discussions and raising suggestions, as well as cross-checking my results.

Many thanks also to Dr. Philipp Basler for giving always competent answers to BSMPT-related questions.

Thanks also to Dr. Jonas Wittbrodt for providing in-depth insight into `ScannerS` and clarifying issues.

On behalf of all system administrators, many thanks to M.Sc. Martin Gabelmann, for providing and maintaining the computing cluster and for giving me access to it.

Last but not least, thanks to all members of the Institute for Theoretical Physics. You made me feel welcome, although most probably have never seen me in person throughout this year during a very strange time.

In the end, my biggest thanks goes to Heike and Bernd. You raised me to always be curious and supported me in every possible way. Thank you for everything!

Appendix

A. Fourth derivative of the Coleman-Weinberg potential

In [54] the authors present a general analytic expression for derivatives of the Coleman-Weinberg potential. An essential part of the fourth derivative of the Coleman-Weinberg potential is the following function

$$f_{(T)abcd}^{(1)} = \frac{m_a^2 \log \frac{m_a^2}{\mu^2}}{(m_a^2 - m_b^2)(m_a^2 - m_c^2)(m_a^2 - m_d^2)} + \frac{m_b^2 \log \frac{m_b^2}{\mu^2}}{(m_b^2 - m_a^2)(m_b^2 - m_c^2)(m_b^2 - m_d^2)} \quad (\text{A.1})$$

$$+ \frac{m_c^2 \log \frac{m_c^2}{\mu^2}}{(m_c^2 - m_a^2)(m_c^2 - m_b^2)(m_c^2 - m_d^2)} + \frac{m_d^2 \log \frac{m_d^2}{\mu^2}}{(m_d^2 - m_a^2)(m_d^2 - m_b^2)(m_d^2 - m_c^2)}.$$

In the limit of vanishing masses, $f_{(T)abcd}^{(1)}$ is divergent. These divergences are known in the literature as relics of the vanishing momenta approximation which is used for calculating the Coleman-Weinberg potential [102, 103]. However, the divergences cancel if the calculation is performed over the whole momentum range. For the 2HDM, the diagrammatic approach was shown to yield finite results for vanishing momenta for the second and third derivatives [104, 105].

We calculate the degenerate mass limits of $f_{(T)abcd}^{(1)}$ and recreate the results for vanishing masses by dropping the IR divergences.

There are in total 52 limit cases that have to be considered separately. Equation (A.1) only holds in case all masses squared are non-degenerate. The degenerate mass limits for $f_{(T)abcd}^{(1)}$ read

$$f_{(T)aacd}^{(1)} = \lim_{m_b^2 \rightarrow m_a^2} f_{(T)abcd}^{(1)} = \frac{1}{(m_a^2 - m_c^2)(m_a^2 - m_d^2)} + \frac{(-m_a^2 + m_c^2 m_d^2) \log \frac{m_a^2}{\mu^2}}{(m_a^2 - m_c^2)^2 (m_a^2 - m_d^2)^2} \quad (\text{A.2})$$

$$+ \frac{m_c^2 \log \frac{m_c^2}{\mu^2}}{(m_c^2 - m_a^2)^2 (m_c^2 - m_d^2)} + \frac{m_d^2 \log \frac{m_d^2}{\mu^2}}{(m_d^2 - m_a^2)^2 (m_d^2 - m_c^2)},$$

$$f_{(T)aacc}^{(1)} = \lim_{m_d^2 \rightarrow m_c^2} f_{(T)aacd}^{(1)} = \frac{2}{(m_a^2 - m_c^2)^2} - \frac{(m_a^2 + m_c^2) \log \frac{m_a^2}{\mu^2}}{(m_a^2 - m_c^2)^3} + \frac{(m_a^2 + m_c^2) \log \frac{m_c^2}{\mu^2}}{(m_a^2 - m_c^2)^3}, \quad (\text{A.3})$$

$$f_{(T)aaad}^{(1)} = \lim_{m_c^2 \rightarrow m_a^2} f_{(T)aacd}^{(1)} = \frac{-m_a^2 + m_d^2}{2m_a^2(m_a^2 - m_d^2)^3} + \frac{m_d^2(\log \frac{m_a^2}{\mu^2} - \log \frac{m_d^2}{\mu^2})}{(m_a^2 - m_d^2)^3}, \quad (\text{A.4})$$

$$f_{(T)aaaa}^{(1)} = \lim_{m_d^2 \rightarrow m_a^2} f_{(T)aaad}^{(1)} = -\frac{1}{6m_a^4}. \quad (\text{A.5})$$

The zero mass limits read

$$f_{(T)aac0}^{(1)} = \frac{1}{m_a^2(m_a^2 - m_c^2)} - \frac{\log \frac{m_a^2}{\mu^2}}{(m_a^2 - m_c^2)^2} + \frac{\log \frac{m_c^2}{\mu^2}}{(m_c^2 - m_a^2)^2}, \quad (\text{A.6})$$

$$f_{(T)00cd}^{(1)} = \frac{1}{m_c^2 m_d^2} + \frac{\log \frac{m_c^2}{\mu^2}}{m_c^2(m_c^2 - m_d^2)} + \frac{\log \frac{m_d^2}{\mu^2}}{m_d^2(m_d^2 - m_c^2)}, \quad (\text{A.7})$$

$$f_{(T)aa00}^{(1)} = \frac{2 - \log \frac{m_a^2}{\mu^2}}{m_a^4}, \quad (\text{A.8})$$

$$f_{(T)aaa0}^{(1)} = -\frac{1}{2m_a^4}, \quad (\text{A.9})$$

$$f_{(T)000d}^{(1)} = 0, \quad (\text{A.10})$$

$$f_{(T)0000}^{(1)} = 0. \quad (\text{A.11})$$

B. Benchmark points

Two parameters of the tree-level potential are fixed through Eqs. (3.8) and (3.10b),

$$\lambda_1 \simeq 0.258 \quad \text{and} \quad m_{11}^2 \simeq -7823.754. \quad (\text{B.1})$$

The benchmark points of Figs. 4.2-4.6 and Fig. 5.1 are listed in Tabs. B.1-B.4. The mass and trilinear parameters that define the scalar tree-level potential of Eq. (3.4) are given in Tab. B.1. Table B.2 shows all quartic parameters of the scalar tree-level potential. Table B.3 gives the dark mass spectrum and Tab. B.4 includes results from BSMPT.

point	m_{22}^2 [GeV ²]	m_S^2 [GeV ²]	Re(A) [GeV]	Im(A) [GeV]
F1R57	24.2572×10^4	10.9399×10^4	93.784	126.304
F11R239	20.6512×10^4	24.4128×10^4	-126.573	196.608
F12R229	41.0665×10^4	68.9511×10^4	-327.739	693.838
F13R406	42.8085×10^4	42.8085×10^4	305.087	13.242
F14R415	53.9115×10^4	48.5477×10^4	92.486	-60.547
F16R126	39.0001×10^4	29.9337×10^4	-935.289	269.068
F16R292	21.8590×10^4	36.4763×10^4	760.170	383.020
F610R819	1.2474×10^4	6.3588×10^4	213.475	183.850

Table B.1.: Mass and trilinear parameters for the benchmark points that are displayed in Figs. 4.2-4.6 and Fig. 5.1. For a definition of the tree-level scalar potential of CP in the Dark in terms of the mass, trilinear and the quartic parameters (see Tab. B.2), see Eq. (3.4) in Chapter 3.

point	λ_2	λ_3	λ_4	λ_5	λ_6	λ_7	λ_8
F1R57	4.691	-0.215	-0.425	-0.138	15.076	6.779	-1.865
F11R239	0.182	7.246	-1.575	-1.374	9.168	2.741	-0.273
F12R229	0.003	8.582	-4.247	4.121	13.441	-1.217	3.842
F13R406	8.203	-1.144	0.212	0.138	2.966	13.277	-0.962
F14R415	3.230	2.357	-2.850	0.023	0.528	14.036	-0.137
F16R126	0.202	10.855	-5.014	-4.562	12.445	-0.001	-0.498
F16R292	1.141	5.869	2.777	1.657	11.743	-1.211	-0.288
F610R819	1.244	0.957	2.327	1.852	13.441	0.132	-0.447

Table B.2.: Quartic parameters of the tree-level scalar Lagrangian in Eq. (3.4) for all benchmark points that are displayed in Figs. 4.2-4.6 and Fig. 5.1.

point	m_{H^\pm} [GeV]	m_{h_1} [GeV]	m_{h_2} [GeV]	m_{h_3} [GeV]
F1R57	485.849	457.136	472.254	573.769
F11R239	652.815	537.595	594.005	665.010
F12R229	819.030	568.480	792.037	886.724
F13R406	627.232	625.769	629.053	927.451
F14R415	781.375	722.691	723.973	955.426
F16R126	847.964	346.466	768.153	850.479
F16R292	629.670	434.530	668.582	808.410
F610R819	203.684	88.170	301.213	439.503

Table B.3.: Dark scalar masses for the benchmark points that are displayed in Figs. 4.2-4.6 and Fig. 5.1. Note, that in CP in the Dark the mass hierarchy of the neutral dark scalars is defined as $m_{h_1} < m_{h_2} < m_{h_3}$, see Chapter 3.

point	T_c [GeV]	v_c [GeV]	ξ_c
F1R57	184.717	198.073	1.072
F11R239	189.377	203.315	1.074
F12R229	160.941	165.709	1.030
F13R406	150.751	158.765	1.053
F14R415	174.454	180.154	1.033
F16R126	196.417	236.532	1.204
F16R292	198.596	213.333	1.074
F610R819	141.129	142.779	1.012

point	$\bar{\omega}_{\text{CB}}$ [GeV]	$\bar{\omega}_1$ [GeV]	$\bar{\omega}_2$ [GeV]	$\bar{\omega}_{\text{CP}}$ [GeV]	$\bar{\omega}_S$ [GeV]
F1R57	9.1×10^{-7}	198.073	2.2×10^{-8}	2.2×10^{-6}	4.0×10^{-6}
F11R239	1.2×10^{-6}	203.315	-1.1×10^{-6}	1.3×10^{-6}	-1.6×10^{-6}
F12R229	1.7×10^{-7}	165.709	1.0×10^{-6}	-2.3×10^{-6}	-8.1×10^{-7}
F13R406	1.1×10^{-7}	158.765	1.5×10^{-6}	-7.8×10^{-7}	1.1×10^{-6}
F14R415	-1.1×10^{-6}	-180.154	-2.1×10^{-6}	-9.6×10^{-7}	1.8×10^{-6}
F16R126	-3.2×10^{-7}	-236.532	-4.0×10^{-6}	-9.2×10^{-7}	-1.7×10^{-6}
F16R292	3.2×10^{-6}	213.333	1.5×10^{-6}	2.3×10^{-7}	-5.2×10^{-7}
F610R819	-4.4×10^{-6}	140.117	12.500	-24.430	-27.353

Table B.4.: BSMPT output for the benchmark points whose parameters are listed in Tabs. B.1-B.3. Details on the determination of T_c and v_c with BSMPT can be found in Chapter 5.1.2. The strength of the electroweak phase transition, ξ_c , is derived from the baryon wash-out condition in Eq. (2.22), $\xi_c = \frac{v_c}{T_c}$. The finite-temperature VEV configurations $\bar{\omega}_i$ with $i \in \{1, 2, \text{CB}, \text{CP}, S\}$ minimize the one-loop corrected effective potential at $T = T_c$.